A STUDY ON DUCTILE FRACTURE PREDICTION IN MICROFORMING PROCESS – CONSTITUTIVE MODELING, NUMERICAL SIMULATION AND EXPERIMENTAL VERIFICATION

RAN JIAQI

Ph.D

The Hong Kong Polytechnic University

2014

The Hong Kong Polytechnic University

Department of Mechanical Engineering

A STUDY ON DUCTILE FRACTURE PREDICTION IN MICROFORMING PROCESS – CONSTITUTIVE MODELING, NUMERICAL SIMULATION AND EXPERIMENTAL VERIFICATION

RAN JIAQI

A thesis submitted in partial fulfillment of

the requirements for the degree of

Doctor of Philosophy

May, 2014

CERTIFICATE OF ORIGINALITY

I hereby declare that this thesis is my own work and that, to the best of my knowledge and belief, it reproduces no material previously published or written, nor material that has been accepted for the award of any other degree or diploma, except where due acknowledgement has been made in the text.

RAN JIAQI

Abstract

In macro-scaled plastic deformation, or macroforming, the so-called ductile fracture has been studied from the perspectives of physics, deformation mechanism, affecting factor and prediction criterion. In micro-scaled plastic deformation, or microforming, all of these are relatively new and have not yet been extensively investigated. In tandem with this, an exploration on the applicability of the traditional fracture criteria in micro-scaled plastic deformation and the study of how size effect affects the deformation and fracture behaviors in the process is critical. Using micro flanged upsetting as a case study process, the fracture in microforming process is studied via experimental and finite element (FE) simulation. The FE simulation is conducted using established model based on the widely accepted surface layer model in microforming arena. Both physical experiments and simulations show that the size effect has a significant influence over fracture formation in micro-scaled plastic deformation. It is found that the ductile fracture affected by size effect is difficult to occur in microforming process under the same deformation conditions at which the fracture happens in macroforming scenario. The research thus provides an in-depth understanding of ductile fracture in micro-scaled plastic deformation.

In the first stage of this research, a general constitutive model is established and Freudenthal fracture criterion is used as it is a classical damage accumulation

criterion. The influence of grain itself to fracture initiation in the entire deformation process is studied. The primary fracture prediction is conducted with this model.

In the second stage, dislocation density is implemented into the hybrid constitutive model to distinguish the stress contribution of body-centered cubic (BCC) and face-centered cubic (FCC) structures in multiphase materials. Freudenthal fracture criterion is used as the fracture criterion for the compression-dominative deformation process. The stress-induced fracture map is first proposed to evaluate the effects of grain and feature sizes on the fracture behavior in microforming.

Then, six uncoupled fracture criteria are studied and discussed in order to determine their applicability in micro-scaled forming process. The fracture strain via simulation is compared with the actual experimental fracture strain and a generalized form of ductile fracture criteria is provided for a better explanation and understanding of the criteria.

In the last part of this research, the flow stress model for sheet metal deformation process is presented. Using micro-scaled deep drawing process for experiment verification, the validity of the surface layer model is discussed and the explanation for the difference of simulation and experimental results is presented.

Keywords: Micro-scaled plastic deformation, Microforming, Size effect, Ductile fracture, Stress-induced fracture map.

Publications arising from the Thesis

Ran J.Q., Fu M.W., Chan W.L., 2013. The influence of size effect on the ductile fracture in micro-scaled plastic deformation, International Journal of Plasticity 41, 65-81.

Ran J.Q., Fu M.W., 2013. A hybrid model for analysis of ductile fracture in micro-scaled plastic deformation of multiphase alloys, International Journal of Plasticity, online available.

Ran J.Q., Fu M.W. A Hybrid Fracture Prediction Model of Multiphase Metals in Micro scaled Forming Processes, the 8th International Conference on Micro Manufacturing, Victoria, British Columbia, Canada, on March 25 – 28, 2013.

Ran J.Q., Fu M.W., 2014. Applicability of the uncoupled ductile fracture criteria in micro-scaled plastic deformation, submitted to International Journal of Plasticity.

Acknowledgements

I would like to express my sincere gratitude to my supervisor Dr. Ming Wang FU for guiding me into the world of micro manufacturing, for his precious advice, cheerful encouragement and endless patience. This dissertation cannot be finished without his invaluable supervision.

Also I would like to thank my former and present team members Dr. WaiLun Chan and Mr. JiLai Wang for providing the necessary assistance. Special thanks to Dr. ZhengGang Liu for sharing his expertise on mathematics.

This dissertation is dedicated to my parents for their endless love, understanding and support, and to Dizi, the lady who holds my hand and brings me sunshine on my toughest days.

Table of Contents

Chapter 1 Introduction

1.1 Background

Metal forming, which transforms the bulk or sheet raw materials with simple geometry into target workpiece without changing the mass of the materials, is extremely important among all manufacturing processes as it saves manufacturing cost by eliminating material wastes and saving energy. With the development of modern forming technologies, workpieces with different shapes, dimensions and materials are able to be fabricated with metal forming processes. Meanwhile, the workpieces made by forming process possess excellent mechanical properties due to the good flowline and microstructure in deformed parts [1].

Compared with conventional metal forming processes in macro-scale, microforming is a significant and promising manufacturing process to fabricate small parts with at least two dimensions in sub-millimeter scale. Unlike other micro-manufacturing processes, such as micromachining and micro-electro-mechanical-systems (MEMS) based lithography processes, microforming has some unique advantages such as low production cost, high material utilization, good productivity, excellent material properties, and net-shape or near-net-shape geometries, similar to what macroforming has. Due to the huge demand on micro-scaled components in different industrial clusters, microforming has become increasingly important in biomedical, watch, micro electronic device and consumer electronics industries in different forms of micro-scaled parts including micro screw, micro pin, micro spring, micro gear, micro shaft, micro switch, etc.

According to previous researches, the material flow mechanisms of conventional macro- and micro-scaled plastic deformation processes are not completely the same due to the so-called size effect in microforming. The size effect, which characterizes and differentiates the deformation behaviors of microforming from macroforming, is considered as an important factor in ductile fracture prediction of microforming. As a result, the fracture formation in microforming could be different from the one in macroforming in terms of fracture behavior, mechanism, and the affecting factor [2].

In microforming researches, many prior arts basically focused on the material flow behaviors in the processes with the consideration of size effect. In macro-scaled plastic deformation processes, viz., macroforming, the so-called ductile fracture has been studied in terms of physics, mechanism, affecting factor and the prediction criterion. In micro-scaled plastic deformation processes, however, all of these are relatively new and have not yet been extensively investigated. There is a need to provide an in-depth and systematic study on these aspects to establish a more accurate fracture prediction methodology.

1.2 Research issues

In microforming research, one of the key focuses is to develop microforming process to efficiently produce qualified micro-scaled parts. From the previous researches in this area, it is found that the fracture in micro forming and how the size effect affects the fracture in the process have not yet been paid much attention and explored. The forming limit and defect formation in microforming requires a systematic study considering size effect. There is a need to verify whether the conventional fracture theory can be used in micro-scaled plastic deformation. Thus, in-depth research on fracture in microforming processes is critical.

The objectives of this research are to ensure and improve the quality of micro-scaled parts by digging out the root-causes of fracture, and figure out the methods to avoid them. There are two categories of fracture in micro-scaled deformation, which is the stress-induced fracture and flow-induced fracture. The stress-induced fracture is the fracture mainly caused by deformation stress and the flow-induced fracture is generated by irregular material flow. The stress-induced fracture will be focused in this research.

1.3 Research overview

The common representation of the uncoupled ductile fracture model can be designated as a general format:

$$\int_{0}^{\varepsilon_f} f\left(\sigma,\bar{\varepsilon}\right) d\bar{\varepsilon} - C = 0 \tag{1.1}$$

where $f\left(\sigma,\bar{\varepsilon}\right)$ the stress-related function, $\bar{\varepsilon}$ is the equivalent strain, ε_f is the fracture strain and C is the critical value.

In Eq. (1.1), C is different for different fracture criteria and materials. For multiphase metal with the same heat treatment condition, C is considered as the same. $\bar{\varepsilon}_f$ is the expected fracture strain calculated based on fracture model. There are two critical issues in the micro-scaled fracture prediction: one is the constitutive modeling for micro-scaled deformation process, the other one is to determine the applicable fracture criterion. By addressing these two issues, the most suitable fracture model for microforming is established. The general representation of the fracture model is demonstrated in Fig. 1.1.

In Fig. 1.2, the fracture prediction research is divided into four stages. The first stage is to investigate how the size effect affects the stress-strain relationship in plastic deformation by comparing the experimental results of the macro- and micro-scale. The second stage is to study the applicability of different fracture criteria in micro-scaled deformation. The third stage is to establish the constitutive model of micro-scaled deformation process by considering the influence of size effect. And the final stage is to combine the results of the above three stages together to conduct micro-scaled fracture prediction [3,4]. The details will be discussed in this thesis.

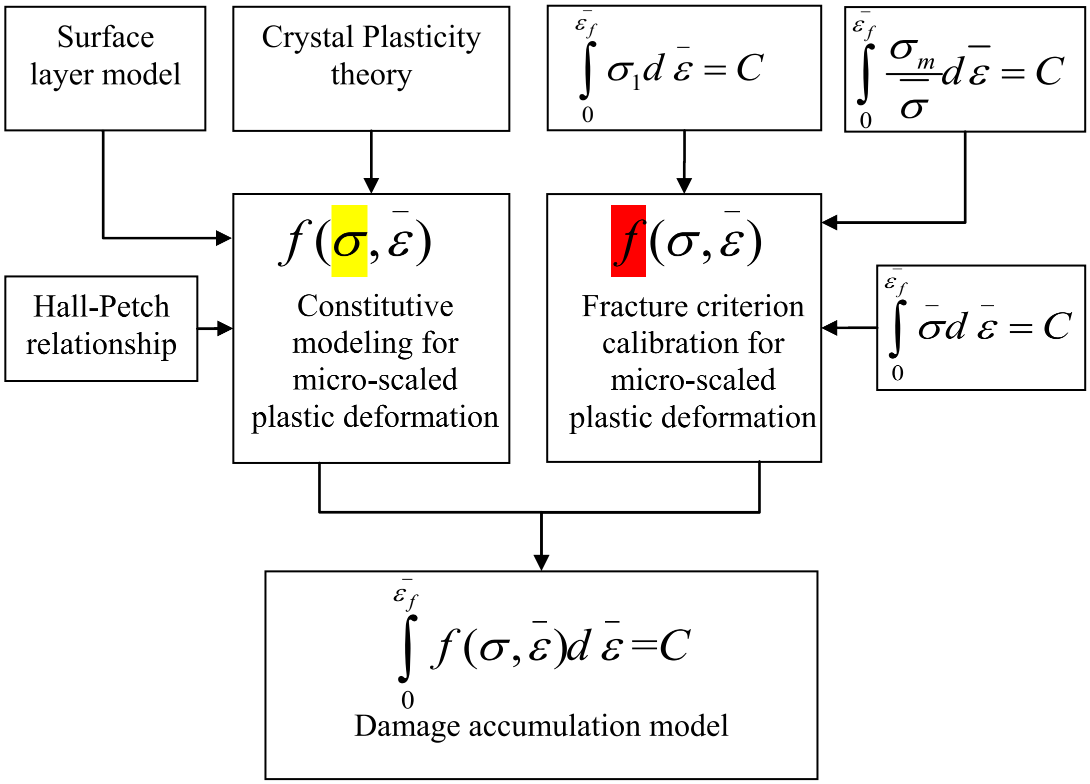

Fig. 1.1. General representation of fracture prediction model.

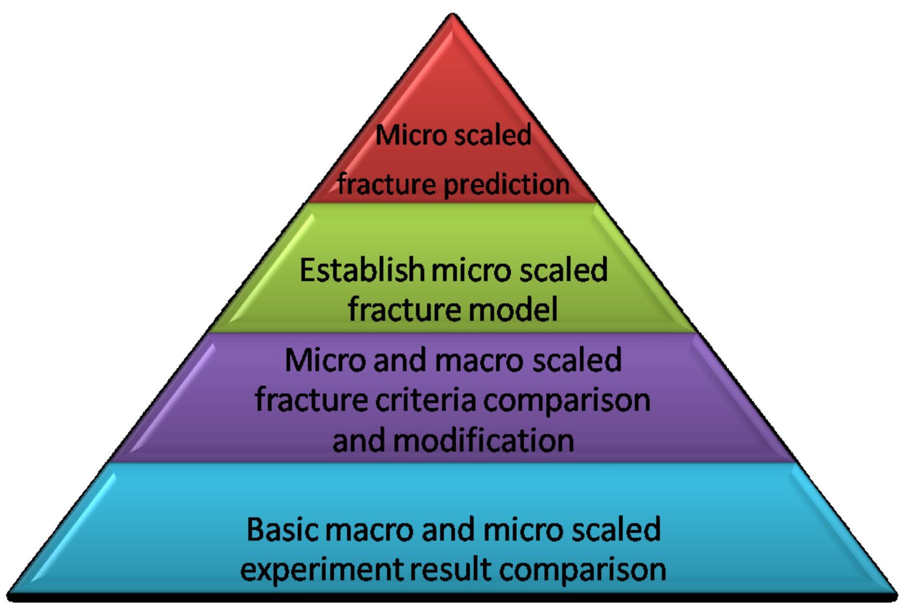

Fig. 1.2. Fracture prediction stages for microforming process.

In the stress model research, the constitutive-model-based fracture model (CFM) is first established for micro-scale. This model is the first attempt which considers the influence of size effect in micro-scaled fracture prediction, and the result is acceptable for testing material and deformation process. However, the physical meaning of some coefficients in CFM has not been explained clearly and the simulation results in some micro-scaled scenarios do not well agree with the experimental result. The hybrid constitutive-model-based fracture model (HCFM) is thus presented for multiphase micro-scaled fracture prediction. With the aim of crystal strengthening theory, the physical meaning of this model is well explained. The stress-induced fracture map (SFM) is proposed by using the calculation result of HCFM to predict the expected fracture strain of all the specimen dimensions with different microstructures prepared via heat treatment. The influence of different types of size effects including feature size effect and grain size effect is analyzed via SFM.

In the fracture criteria selection research, the applicability of various fracture criteria in both macro- and micro-scaled deformation processes is discussed. Six of the most commonly used uncoupled fracture criteria are studied and compared, and the most suitable one is identified for micro-scaled fracture prediction. The influence of size effect over the applicability of each fracture criterion is considered and demonstrated with HCFM. The most suitable fracture criterion for fracture prediction in microforming is thus revealed.

On the other hand, the above research methodology for bulk metal deformation is implemented in ductile fracture prediction in micro-scaled sheet metal deformation. The constitutive model for sheet metal deformation is carried out and the suitable fracture criterion is applied.

1.4 Thesis outline

This thesis consists of seven chapters and a reference list. It is organized into two parts: the fracture prediction for bulk metal forming, and the fracture prediction for sheet metal forming. The first part covers the size effect dependent constitutive modeling, SFM and fracture criteria applicability evaluation from Chapter 3 to Chapter 5. The second part is Chapter 6 which explores the fracture prediction in micro-scaled sheet metal forming. The details of each chapter are shown below:

Chapter 1 provides a brief introduction of the objectives of this research;

Chapter 2 presents a brief literature review of previous researches on microforming and fracture prediction;

Chapter 3 articulates the CFM and introduces the influence of size effect;

Chapter 4 proposes the HCFM for fracture prediction in multiphase alloy. It also demonstrates the establishment of SFM and how to use it to predict the expected fracture strain in different deformation scenarios with different specimen dimensions and heat treatment conditions;

Chapter 5 discusses the applicability and limitation of six commonly used uncoupled fracture criteria in micro-scaled plastic deformation.

Chapter 6 explores the fracture prediction for micro-scaled sheet metal forming.

Chapter 7 concludes this thesis and provides summarizes of the present researches. And the future work of this research is also introduced.

Chapter 2 A Brief Review on Microforming and Ductile Fracture

In metal forming arena, the forming principle of micro-scaled forming and micro-scaled ductile fracture are the key factor to improve the quality of micro-formed parts. To establish the fracture model in micro scale, the constitutive model and fracture criteria in macro-scaled forming are needed to be studied and the difference between the macro- and micro-scaled deformation is discussed. Therefore, a lot of researches have been conducted in microforming and ductile fracture areas. This chapter provides a brief review of the research in these two areas.

2.1 Prior study of microforming

In microforming researches, few efforts are provided to explore ductile fracture and its formation mechanism in this process. Regarding the flow and deformation behaviors, the pioneer researches include the exploration done by Pawelski, which concluded that the rules for macroforming are not fully applicable in manufacturing of the scaled-down parts using the same forming process [5]. Size effect is thus proposed to define the limitations induced in the scaled down forming processes. Michel and Picart conduct the evaluation of size effect on the flow stress of materials using the tensile test experiment of brass samples [6,7]. The material parameters are implemented in a constitutive model for sheet metal specimen based on the experimental results to evaluate the stress-strain model. Fu and Chan have done a systematic research on the influence of size effect over the deformation behavior and the friction variation in microforming processes [8,9]. In their researches, a series of flow stress curves are generated for the scaled down specimens and the applicability of these curves are validated via experiments and simulations. To present the panorama of the whole research status of microforming, Vollertsen have conducted a comprehensive review and succinctly figured out the issues to be addressed in development of micro forming processes and micro-scaled parts [10,11].

2.2 Hall-Petch equation and dislocation theory

In polycrystal grains, grain boundaries are opaque to dislocations passing through grain by grain. In order to generate deformation of the assembled grains, various sets of slip systems among all the grains are needed. The process in which the grain boundary acts as a barrier of the dislocation movement of polycrystal grain is discussed in this chapter. As this analysis is based on the slip system orientation without considering the deformation mechanism, the Taylor factor is thus considered to be independent of grain size. Based on the phenomenon that the decreasing grain size causes the increasing plastic resistance, this analysis states the plastic resistance of polycrystals depends on grain size, which indicates that grain boundaries is an important factor in strengthening. The Hall-Petch equation is supposed to be an explanation of the grain strengthening theory. The dislocation pileups achieve the required percolation in the neighboring grains for the initiation of new slip processes, which thus develop the stress concentrations and initiate the grain strengthening process [12].

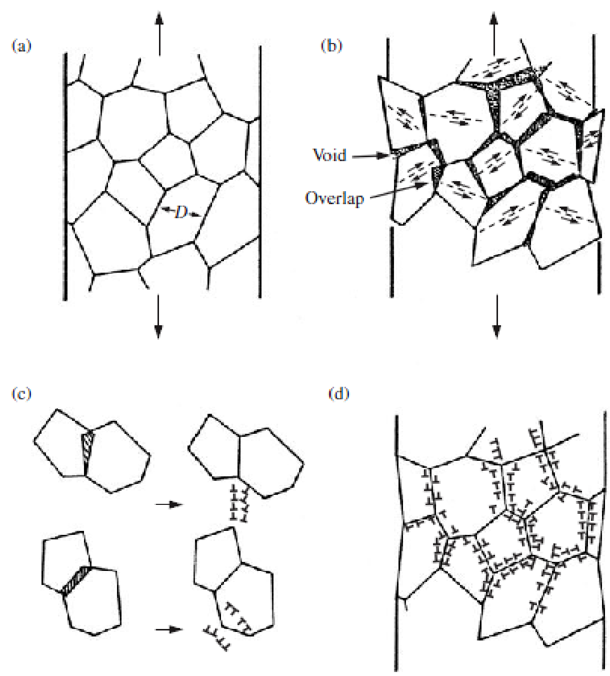

Fig. 2.1. Ashby's crystal strengthening theory [12].

Ashby proposed a satisfactory mechanistic interpretation of grain size dependence in terms of the presence of geometrically necessary dislocations resulted from the additional local deformation gradient which is needed to maintain compatibility among grains [13]. Fig. 2.1 (a) shows that a polycrystal is about to undergo plastic flow. Grain deformation will become incompatible if each grain is able to deform along its slip system, as depicted in Fig. 2.1 (b,c,d).

As it can be seen from Fig. 2.2, when considering the dislocation pile up in slip plane of a polycrystal grain, the applied tensile stress σ and the concentrated shear stress $\sigma_{xy}\left(x=\delta\right)$ at a distance δ from the grain boundary will have the following relationship:

$$\sigma_{xy}\left(x=\delta\right)=\left(\sigma-\sigma_0\right)m\sqrt{\frac{d}{4\delta}} \tag{2.1}$$

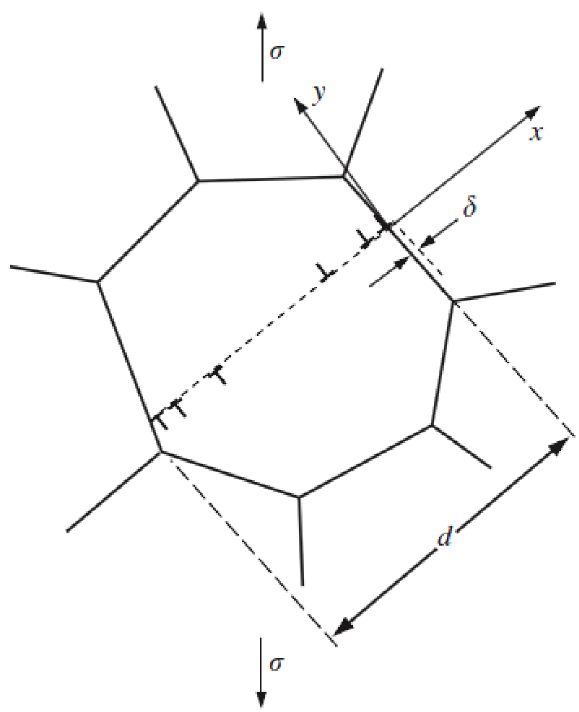

Fig. 2.2. Pile-up with flank friction [12].

In Eq. (2.1), σ_0 is the critical tensile stress required for initiation of the relative motion across the faces of slip plane (the shear crack) in the soft grain, m is the Schmid factor of the slip plane relative to the tensile axis. When the concentrated shear stress reaches the level of critical shear stress σ_{sc} which initiated the deformation of neighboring grain, the percolation of plastic behavior will be achieved. Thus, Eq. (2.1) is thus expressed as:

$$\sigma = \sigma_0 + kd^{-\frac{1}{2}} \tag{2.2}$$

which is known as the Hall-Petch relation and $k = (\sigma_{sc} / m)\sqrt{4\delta}$.

2.3 Size effect and surface layer model

In metal forming, flow stress is considered as the most important parameter in describing the material deformation behavior. In Fig. 2.3, the upsetting test is scaled down to study the material deformation behavior considering the size effect. It is discovered that the flow stress decreases with the dimensions of the billet. This effect has been proved by several experiments of different forming methods including sheet metal forming, bulging test and upsetting test [10].

In these experiments, the dimension of the specimen and molds are multiplied with a scaling factor. In Fig. 2.3, it is obvious that the flow stress decreases with the scaling factor. The reason of this phenomenon can be explained by the surface layer model theory, as shown in Fig. 2.4.

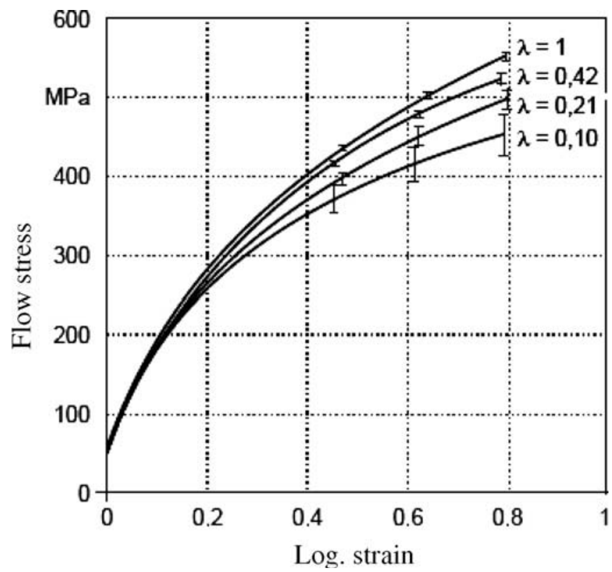

Fig. 2.3. The scaled down upsetting tests [10].

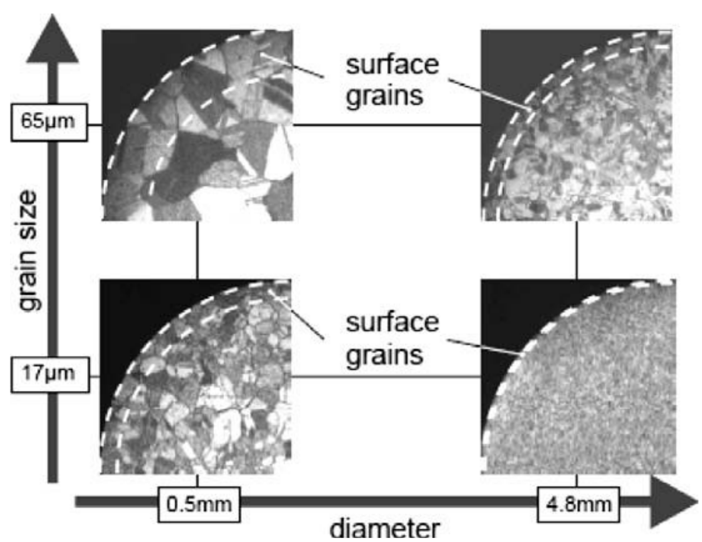

Fig. 2.4. Different portions of surface grains [14].

The mechanical property is mainly determined by the grain size, feature size and grain orientation in microforming processes. Size effect, which plays an important role in microforming, is initiated with the combination of specific grain size and feature size. Size effect can be classified in two different types: grain size effect and feature size effect. The feature size effect is to decrease the specimen size without changing the grain size. Meanwhile, the grain size effect is to enlarge the grain size while keep the feature size as constant. Grain size effect considers how grain size affects the deformation and deformation related phenomena in micro-scaled plastic deformation process. Feature size effect refers to the phenomenon by which the geometry dimensions of the workpiece affects the deformation. Both size effects take place when reducing the ratio between the feature size and grain size, as shown in Fig. 2.4 and 2.5.

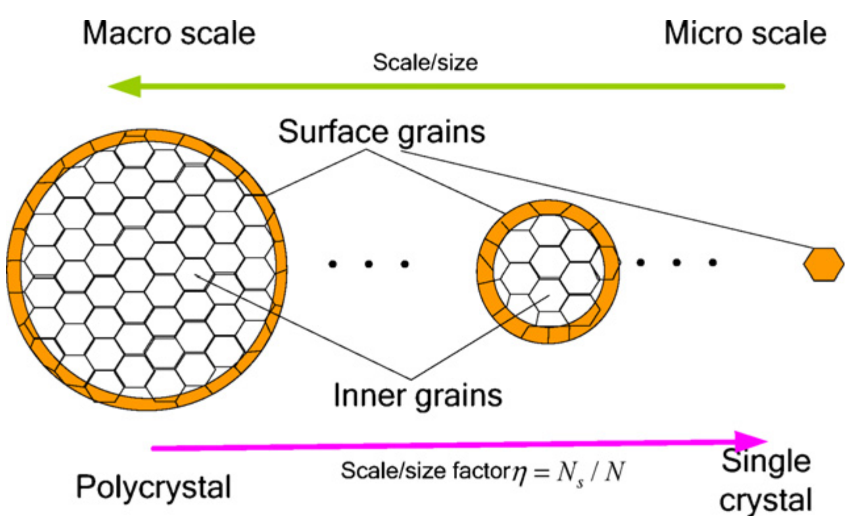

Fig. 2.5. Surface layer model [14].

To model the size effect in microforming, surface layer model is proposed. It suggests that the grain cells at the outer surface of the specimen are considered to have less constrain than other grain cells at the internal area of the specimen. In micro-scaled deformation, the dislocations which are moving through the grain will pile up at the grain boundary. But this phenomenon will not initiate at the free surface, which is the outer layer of the grain. In addition, lower deformation resistance and less hardening are generalized in the outer layer of the specimen.

2.4 Ductile fracture

Regarding the forming limit and the defect formation in microforming, Gouveia et al. have investigated the applicability of four ductile fracture criteria in metal forming processes [15]. The accuracy of the fracture prediction is examined and compared with the experimental results. In addition, Ogawa et al. have conducted the research on the forming limit of magnesium alloy [16]. It is found that the magnesium alloys have different workability after heat treatment due to oxidation. According to this phenomenon, a tensile stress related fracture criterion is proposed to predict the forming limit of the alloy. Sljapic et al. have investigated the fracture of cold upsetting process of brass [17]. The axi-symmetric brass forming experiments are modeled by finite element method (FEM). The maximum plastic strain coincident with the fracture initiation is identified via simulation. Murty et al. have examined the adequacy of some commonly used criteria which are used to predict ductile fracture in metal forming processes [18]. By considering the triaxiality, a stress-function-based ductile fracture model is proposed. Li et al. have provided a panoramic evaluation of numerous ductile fracture criteria in macro scaled plastic deformation [19]. By implementation of those criteria in simulation and conducting the physical experiment, the most applicable conditions and application limitation are identified for each criterion. However, the research did not address the applicability of the criteria in micro-scaled plastic deformation. Furthermore, Li et al. have proposed a methodology to predict ductile fracture initiation in tensile test [20]. The one dimensional quasi-static simple tension test is focused and the example of the Lambert W function in material analysis is provided. The feature size effect on ductile fracture initiation is considered in their model. Using the single crystal plasticity model, Kadkhodapour et al. have employed both the experimental and numerical methods to explain the failure mechanism in the tensile test of steels [21]. It is found that the deformation localization is most probably the root-cause of failure in the final stage of the test. The stress state dependence is found to be an important factor in the macroscopic fracture research. Wierzbicki et al. have revealed the relationship between the equivalent strain and stress triaxiality via experiment and FE simulation [22,23]. Fracture models for both the negative stress triaxiality and large triaxiality are proposed. As discussed by Brünig et al., this stress state dependence effect is caused by the stress state dependence of the damage mechanisms occurring at micro-scale [24-26].

2.5 Fracture initiation principle in ABAQUS

The damage evolution law describes the degradation rate of the material stiffness once the corresponding critical value is reached. For damage in ductile metals, FE simulation software ABAQUS assumes that the degradation of the stiffness associated with each active failure mechanism can be modeled using a scalar damage variable [27]. The stress tensor in the material is given by the scalar damage equation:

$$\sigma = (1 - D)\bar{\sigma} \tag{2.3}$$

where σ is the actual equivalent stress tensor, D is the overall damage variable and $\bar{\sigma}$ is the effective stress tensor computed in the current increment. The material loses its load-carrying capacity when D = 1. The removal of a solid element takes place when maximum degradation reaches at any one integration point. However, for the shell element, all through-the-thickness section points at any one integration location of an element must fail before the element is removed from the mesh [27].

Fig. 2.6 illustrates the characteristic stress-strain behavior of a material in which damage is induced. For elastic-plastic material with isotropic hardening, damage consists of two parts: softening of the yield stress and degradation of the elasticity. The solid curve in the figure represents the damaged stress-strain response, and the dashed curve is the undamaged response. The damaged response depends on the element dimensions such that mesh dependency of the results is minimized.

In Fig. 2.6, σ_{y0} and $\bar{\varepsilon}_0^{pl}$ are the yield stress and equivalent plastic strain at the onset of damage, and $\bar{\varepsilon}_f^{pl}$ is the equivalent plastic strain at failure; that is, when the overall damage variable reaches the value 1. The overall damage variable D captures the combined effect of all active damage mechanisms [27].

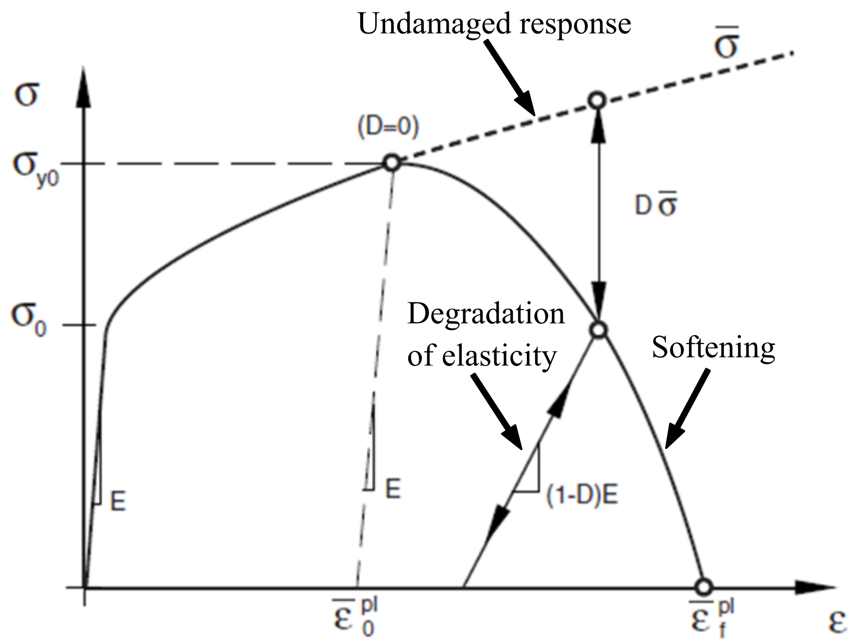

Fig. 2.6. Stress-strain curve with progressive damage degradation [27].

The stress-strain relationship is not able to represent the material's behavior precisely after the material damage initiation. In this situation, there will be a strong mesh dependency in terms of strain localization, if the stress-strain relationship is still applied in simulation.

Hillerborg proposes a different approach which follows the strain-softening branch of the stress-strain response curve, and is used to reduce mesh dependency by creating a stress-displacement response after damage is initiated [28]. In strain-hardening stage, the required flow stress increase with the equivalent strain. In strain-softening stage for further deformation becomes smaller, and the stress-strain response is thus unreliable. Using brittle fracture concepts, he defines the energy required to open a unit area of crack G_f as a material parameter, as shown in Fig. 2.7. With this approach, the softening response after damage initiation is characterized by a stress-displacement response rather than a stress-strain response. The description of G_f is shown below:

$$G_f = \int_{\bar{\varepsilon}_0^{pl}}^{\bar{\varepsilon}_f^{pl}} L\sigma_y d\bar{\varepsilon}^{pl} = \int_0^{\bar{u}_f^{pl}} \sigma_y d\bar{u}_f^{pl} \tag{2.4}$$

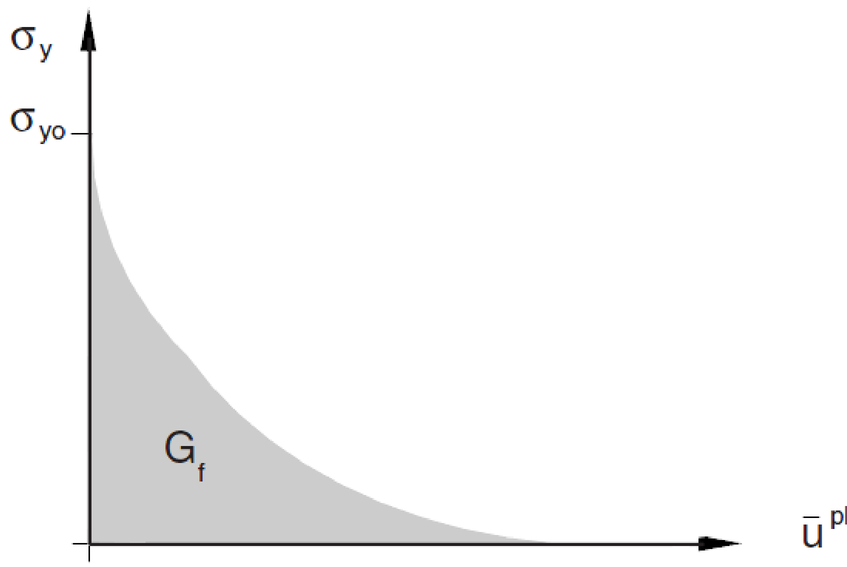

Fig. 2.7. Energy based damage evolution in Abaqus [27].

In Eq (2.4), L is the characteristic length related to mesh. The damage energy can thus be obtained through the simple upsetting and tensile test by getting the true stress and displacement. Fig. 2.8 describes the physical meaning of Hillerborg's theory. In this figure, COD is the crack opening distance and w_t is the crack width when the stress has fallen to zero. According to his theory, although the shaded area is considered damaged, stress will not drop to the zero immediately when the crack opens. Instead, the shaded area contains energy, and the crack will only occur when this energy is absorbed.

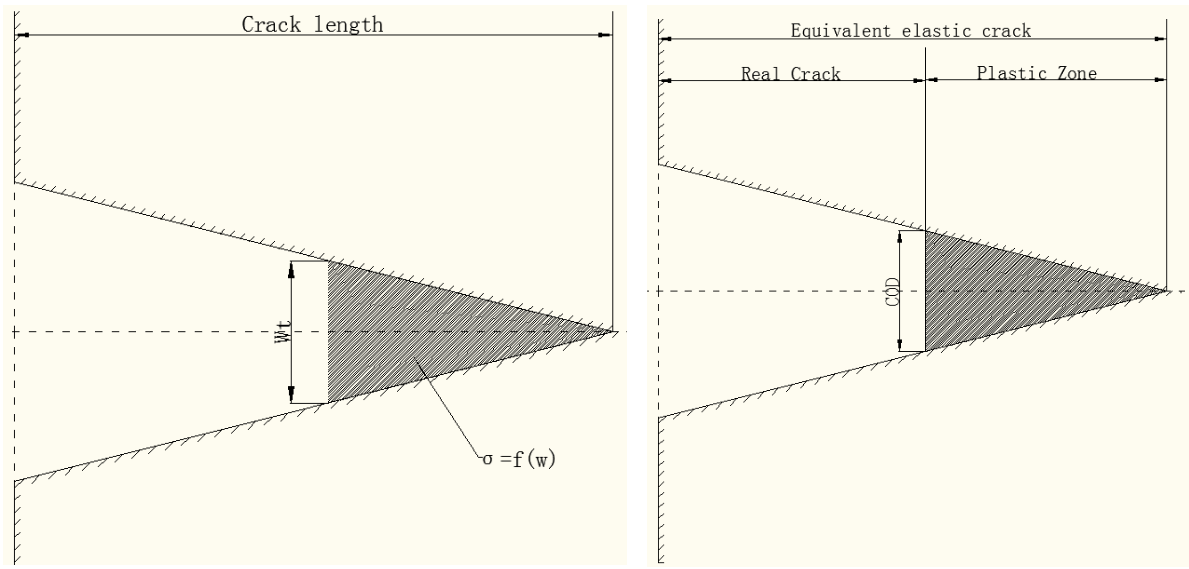

Fig. 2.8. Hillerborg's damage evolution model.

2.6 Summary

The traditional fracture prediction methodology cannot provide a full solution for fracture prediction in micro-scaled plastic deformation. The influence of size effect in constitutive modeling and fracture criterion applicability are discussed separately. A knowledge system which consists of constitutive modeling, fracture criterion calibration and influence evaluation of different size effects is needed. In this research, these research issues are discussed and addressed in micro-scaled plastic deformation. The details will be systematically presented in the following chapters.

Chapter 3 Micro Flanged Upsetting Study

3.1 Introduction

In microforming, the forming limit and defect formation in the process need a systematic research considering size effect and it is critical to explore whether the conventional fracture theory can be used in micro-scaled plastic deformation. Therefore, this chapter aims at addressing this issue via development of a surface layer model considering the size effect in microforming process to model and represent the formation of micro fracture. To realize these thoughts, experiments and numerical simulations in which size effect is taken into account are thus conducted. The simulation and experimental results are compared and the proposed size effect based surface layer model is developed and verified.

3.2 Research procedure

Fig. 3.1 presents the research procedure employed in this chapter. The stress-strain relationship of the testing material (brass) is first established through macro and micro scaled upsetting experiments. After the size factor, which represents the percentage of the surface grains among all the grains in the workpiece, is calculated according to the specimen dimension, a micro-scaled upsetting stress-strain model is established. The simulations of micro flanged upsetting are then conducted using the model and the corresponding simulation results are compared with the experimental ones to determine whether the forming process is influenced by size effect. Finally, the micro-scaled fracture prediction is provided using these results. By implementing the stress-strain model into Freudenthal fracture criterion, the fracture energy of the testing specimen is calculated and the fracture initiation strain is predicted and compared with the experimental results.

3.3 Material behavior modeling considering size effect

In microforming process, when the ratio between the sample dimension and grain size is reduced, both the feature and grain size effects affect the material properties and deformation behaviors in microforming process. In this chapter, the two size effects are considered in the simulation and experiment of the micro flanged upsetting process to investigate the size effect related fracture phenomenon. The flow chart of this chapter is demonstrated in Fig. 3.1.

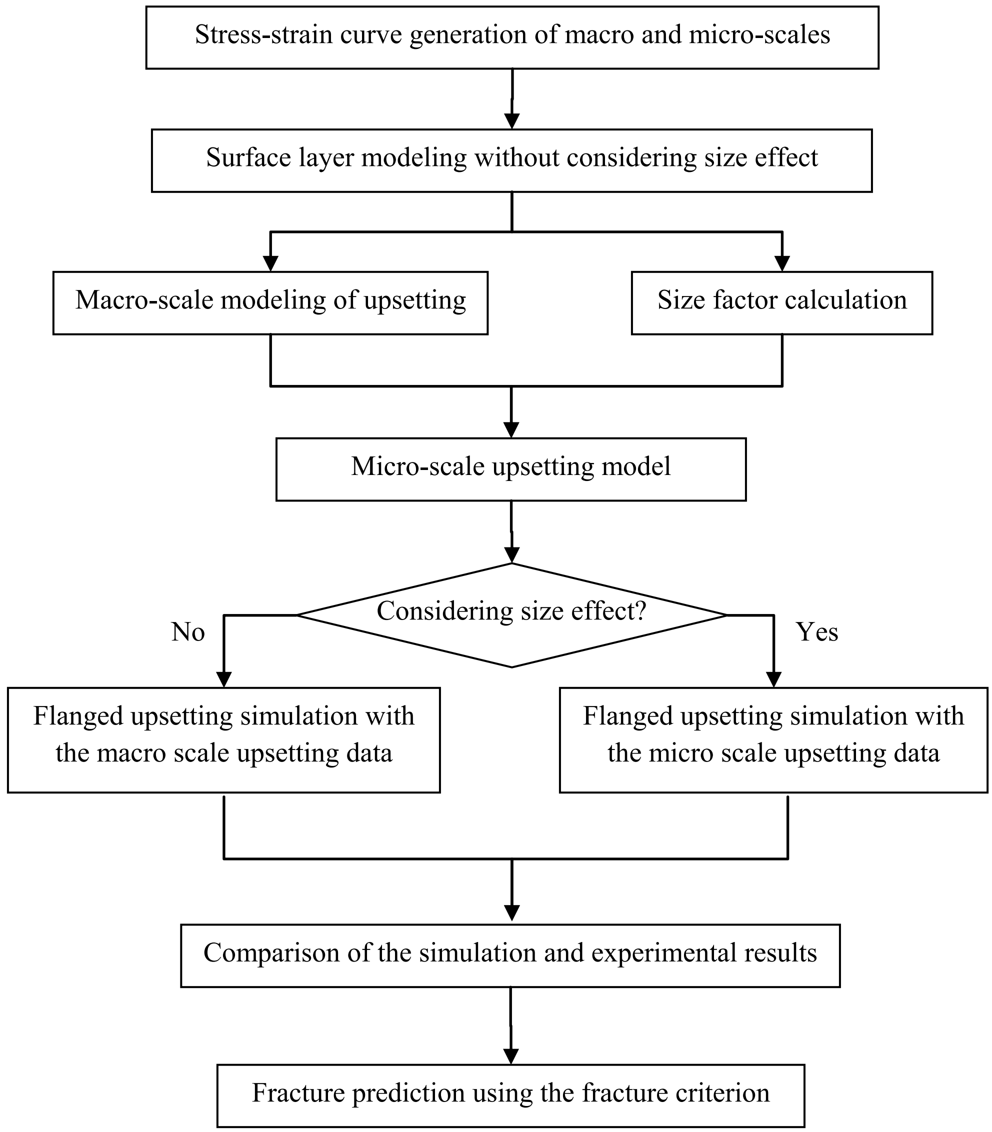

Fig. 3.1. Flow chart of the proposed methodology.

3.4 Surface layer model

A specimen consists of surface and internal grains. The surface grains have less constraints as part of the grains have free surfaces. It is thus easier for them to deform compared with the internal grains. In the conventional macro forming processes, the ratio between the surface and internal grain number is very small such that the contribution of surface grains to the entire deformation can be neglected. In micro forming process, however, this ratio is much larger and the size effect exists. In the surface layer model, the flow stress can be formulated as follows:

$$\sigma = \frac{N_s\sigma_s + N_i\sigma_i}{N} (N = N_s + N_i) \tag{3.1}$$

In Eq. (3.1), σ and N are the flow stress and the total grain number of the specimen. N_i and σ_i are the number and the flow stress of the internal grains, while N_s and σ_s are the number and the flow stress of the surface grains, respectively.

A hybrid material flow stress-strain model is proposed by Lai and Peng [14,29]. In their research, the flow stress of specimen is contributed by two types of flow stresses: the stresses of surface grains and internal grains. The existence of size effect is caused by the ratio change of the surface and internal grains. The mechanical property of the surface grains is similar to single crystal. On the other hand, for the internal grains, a polycrystal model is implemented to represent their material behavior. By applying Schmid Model, Hall-Petch equation and crystal plastic theory [30,31], a hybrid model can be expressed in the following:

$$\begin{cases} \sigma_s(\varepsilon) = m\tau_R(\varepsilon) \\ \sigma_i(\varepsilon) = M\tau_R(\varepsilon) + \dfrac{k(\varepsilon)}{\sqrt{d}} \end{cases} \tag{3.2}$$

In Eq. (3.2), d represents the grain size; m and M are the orientation factors of the surface layer and internal grains; $\tau_R(\varepsilon)$ is the main shear stress; λ is the size factor, which represents the percentage of the surface grains in all the grains of the deformation body. Compared with Eq. (3.1), let $N_s = \lambda \cdot N$, the material flow stress model can thus be designated as:

$$\begin{cases} \sigma(\varepsilon) = \sigma_{ind} + \sigma_{dep} \\ \sigma_{ind} = M\tau_R(\varepsilon) + \dfrac{k(\varepsilon)}{\sqrt{d}} \\ \sigma_{dep} = \lambda\left(m\tau_R(\varepsilon) - M\tau_R(\varepsilon) - \dfrac{k(\varepsilon)}{\sqrt{d}} \right) \end{cases} \tag{3.3}$$

In Eq. (3.3), σ_{ind} represents the conventional polycrystal flow stress which is feature size independent. σ_{dep} is the flow stress related to size factor.

In flanged upsetting process, the raw specimen can be divided into two sections: the surface grain and internal grain sections, as shown in Fig. 3.2. In the figure, the surface grain section is shaded while the internal grain section is not shaded. The height and diameter of the specimen are *H* and *D*, and the grain size is *d*.

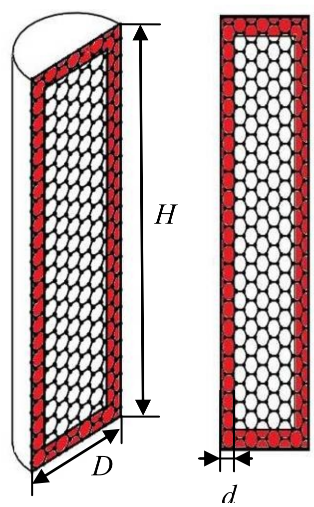

Fig. 3.2. The surface layer model in the micro-scaled simple upsetting and flanged upsetting.

According to Eq. (3.1) and geometrical calculation, the size factor λ is described as follows:

$$\lambda = \frac{N_s}{N} = \frac{\dfrac{\dfrac{\pi D^2 H}{4} - \left(\dfrac{\pi}{4}\left(D-2d\right)^2\left(H-2d\right)\right) - 2\dfrac{\pi D^2}{4}d}{\dfrac{4}{3}\pi\left(\dfrac{d}{2}\right)^3}}{\dfrac{\dfrac{\pi D^2 H}{4}}{\dfrac{4}{3}\pi\left(\dfrac{d}{2}\right)^3}} = \frac{4d}{D}\left(\frac{2d\left(D-d\right)}{DH} + \left(1-\frac{d}{D}\right)\right), \left(d < \frac{D}{2}\right) \quad (3.4)$$

$$\lambda = 1, \left(d \geq \frac{D}{2}\right)$$

Eq. (3.4) represents the size factor when the specimen is still polycrystalline. And when d = D, which means the specimen is single crystalline material and the size factor is 1. It is believed that the billet length must also be considered when the ratio of grain size is close to feature diameter.

3.5 Calculation and comparison of flow stress models in simple upsetting

To demonstrate the influence of size effect over the material flow and compare different models, curve fitting is employed to get the stress-strain curves based on the experimental results. After compared with several mathematical models, the exponential function is considered as the best flow stress model.

First of all, the curve fitting is done with the experimental data of the macro scale billet (2×3*mm*, *H/D* = 1.5) to obtain the coefficients of Hall-Petch equation without consideration of the size effect. The surface layer model is then set up with these coefficients. Finally, the results of the developed model and the conventional bulk forming model without consideration of size effect are compared with the actual data of the micro-scaled simple upsetting experiment.

To establish the size effect dependent flow stress model, the experimental data with small size factor is applied. In this case, the size factor is 0.04 as the grain size of the raw material is 18.54μm. In Fig. 3.3, the four color lines describe the relationship of stress and strain of four series of specimens under different heat treatment conditions with the average grain sizes of 18.54, 24.21, 45.48 and 87.73μm. From Armstrong's flow stress model, the equation below is obtained:

$$\sigma_i(\varepsilon) = M\tau_R(\varepsilon) + \frac{k(\varepsilon)}{\sqrt{d}} \tag{3.5}$$

where M is known as 3.06 for BCC material based on Taylor's model [32]. M is calculated at the yielding process of the material and varies differently when the strain is larger. When the strain exceeds the yield strain, this parameter needs recalculation. $\tau_R(\varepsilon)$ and $k(\varepsilon)$ can be represented by an exponential function of $y = k\varepsilon^n$. If the strain is set to a certain value, the equation will converge to the classic Hall-Petch equation. If a series of strains are given, a series of flow stresses can then be obtained via the simple upsetting experiment [33].

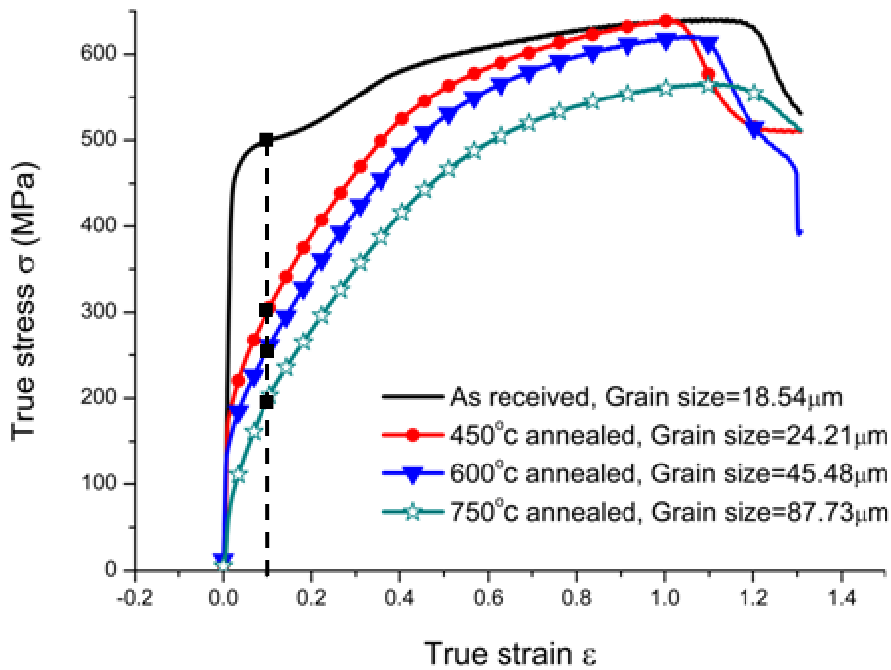

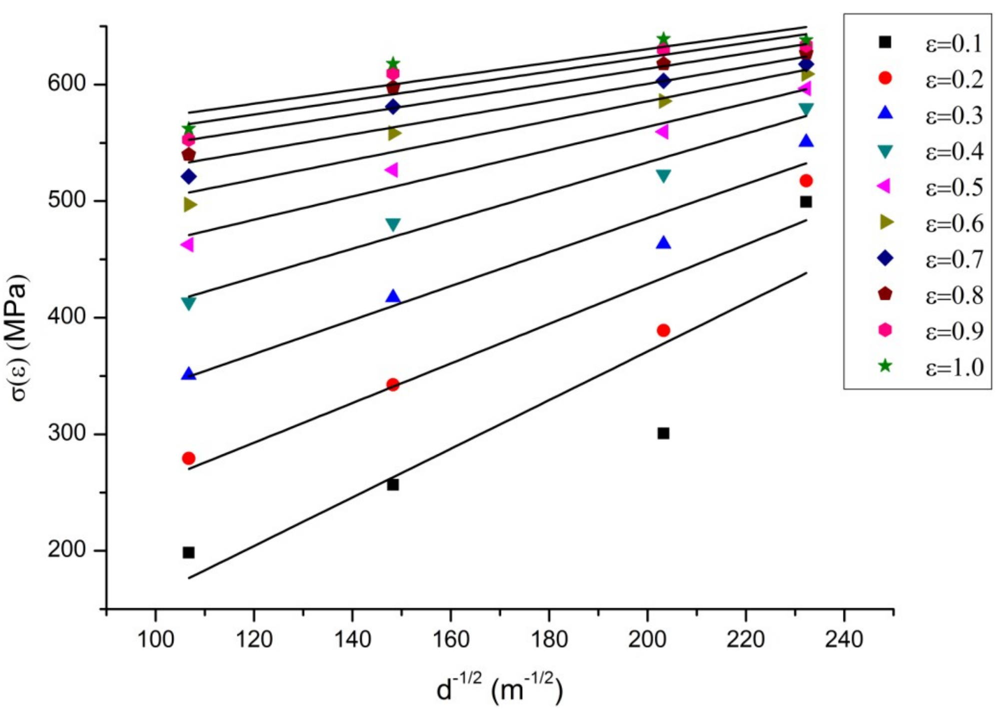

Fig. 3.3. Stress-strain curves of the testing material with different grain sizes.

As mentioned above, if the strain is set to a certain value, $\sigma_i\left(\varepsilon\right)=M\tau_R\left(\varepsilon\right)+\frac{k\left(\varepsilon\right)}{\sqrt{d}}$ will converge to the classic Hall-Petch equation $\sigma_i = M\tau_R + \frac{k}{\sqrt{d}}$. In this equation, both $M\tau_R$ and k are constant. When the grain size d changes after heat treatment, the corresponding true stress will also change. All the grain sizes and stresses can be obtained from experiment. A linear function between grain size d and true stress σ can thus be established and $M\tau_R$ for this certain strain is obtained. Let the strain be 0.1, 0.2, 0.3, and finally to 1.0 with the increasing interval of 0.1, the set of $M\tau_R$, which contains the values for these ten strains can be determined and the relationship between $M\tau_R\left(\varepsilon\right)$ and ε are obtained, as shown in Fig. 3.4.

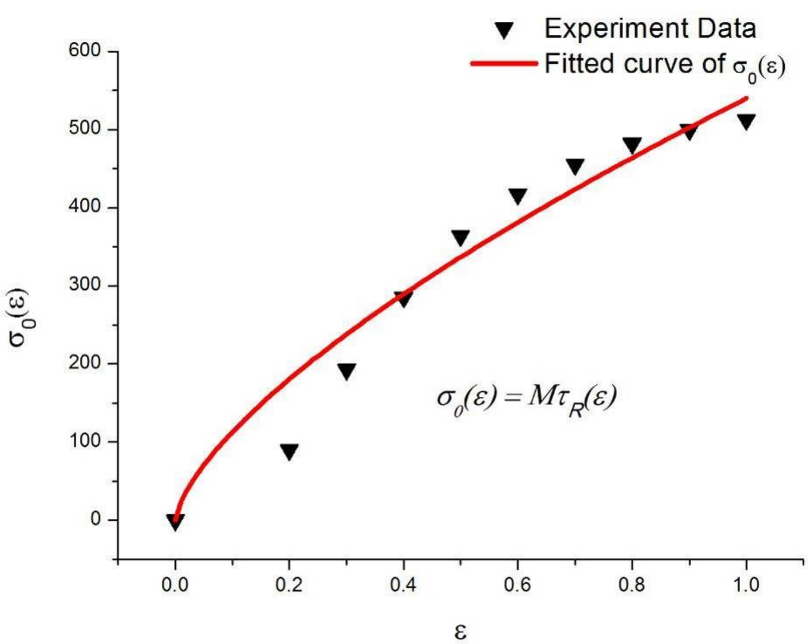

Fig. 3.4. Relationship between $M\tau_R\left(\varepsilon\right)$ and ε.

Therefore, the hypothetic equation of $\tau_R(\varepsilon)$ can be calculated using the nonlinear curve fitting method in the following:

$$\tau_R(\varepsilon) = 176.32\varepsilon^{0.68} \tag{3.6}$$

Integrate Eq. (3.6) with the surface layer model and let the grain orientation factor m equal to 2, which is the minimum limit of this parameter. Conducting the nonlinear fitting with the size factor of $\lambda = 0.6$ and the grain size of d = 18.54μm, $k(\varepsilon)$ is thus obtained as follows:

$$k(\varepsilon) = 73.09\varepsilon^{0.06} \tag{3.7}$$

The final model with M = 3.72 and m =2 (lower bound) are:

$$\begin{cases} \sigma(\varepsilon) = \sigma_{ind} + \sigma_{dep} \\ \sigma_{ind} = M\tau_R(\varepsilon) + \dfrac{k(\varepsilon)}{\sqrt{d}} = 539.53\varepsilon^{0.68} + d^{-\frac{1}{2}}.73.09\varepsilon^{0.06} \\ \sigma_{dep} = \lambda\left(m\tau_R(\varepsilon) - M\tau_R(\varepsilon) - \dfrac{k(\varepsilon)}{\sqrt{d}}\right) = \lambda\left(352.64\varepsilon^{0.68} - 539.53\varepsilon^{0.68} - d^{-\frac{1}{2}}.73.09\varepsilon^{0.06}\right) \end{cases} \tag{3.8}$$

The experimental data and the fit curve are shown in Fig. 3.5.

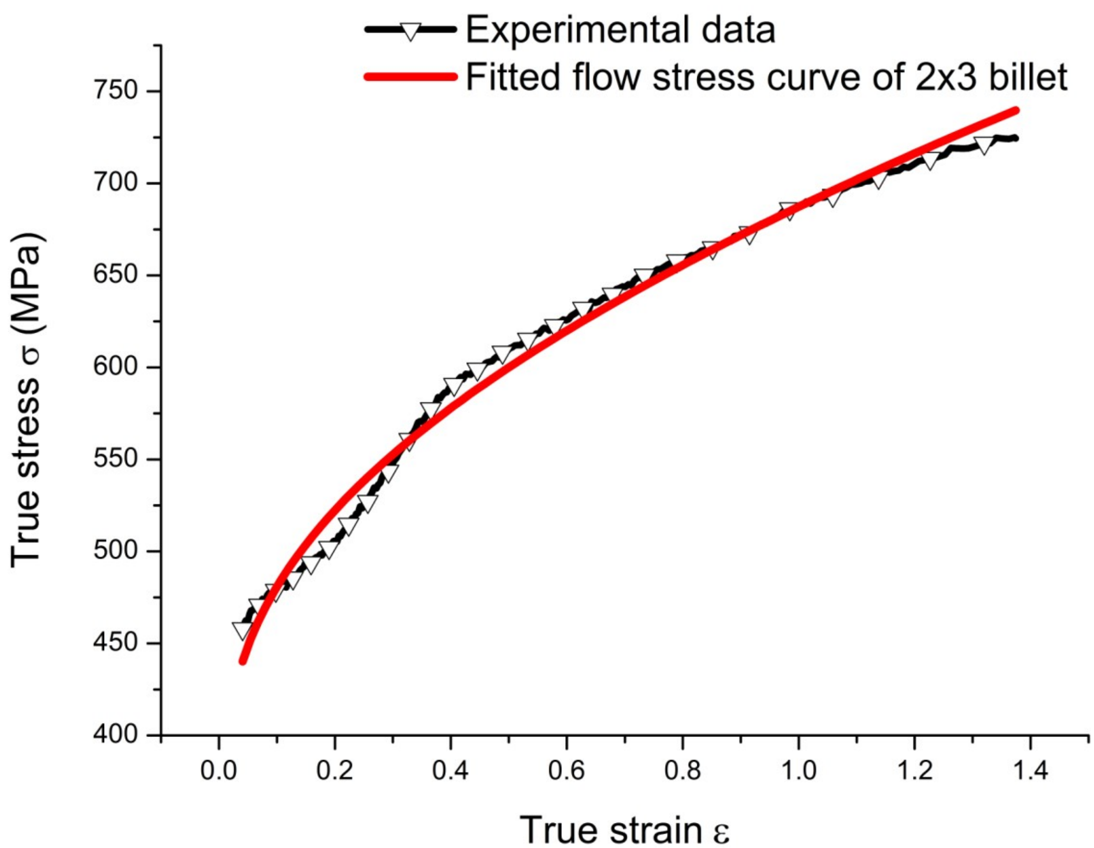

Fig. 3.5. Experimental data and the fitted curve of 2×3*mm* specimens.

Fig. 3.6 shows the two sets of the experimental data by simple upsetting test with the billet dimensions of 2×3*mm* and 0.5×0.75*mm*. From $\varepsilon = 0$ to $\varepsilon = 1.2$, the flow stresses of both the macro and micro scale upsetting increase. In the figure, the area between the curve and the coordinate for the case of 2×3*mm* is obviously larger than the area of the case of 0.5×0.75*mm*, it indicates that the specimen of macro-scaled forming absorbs more energy in deformation process than that of the micro-scaled forming.

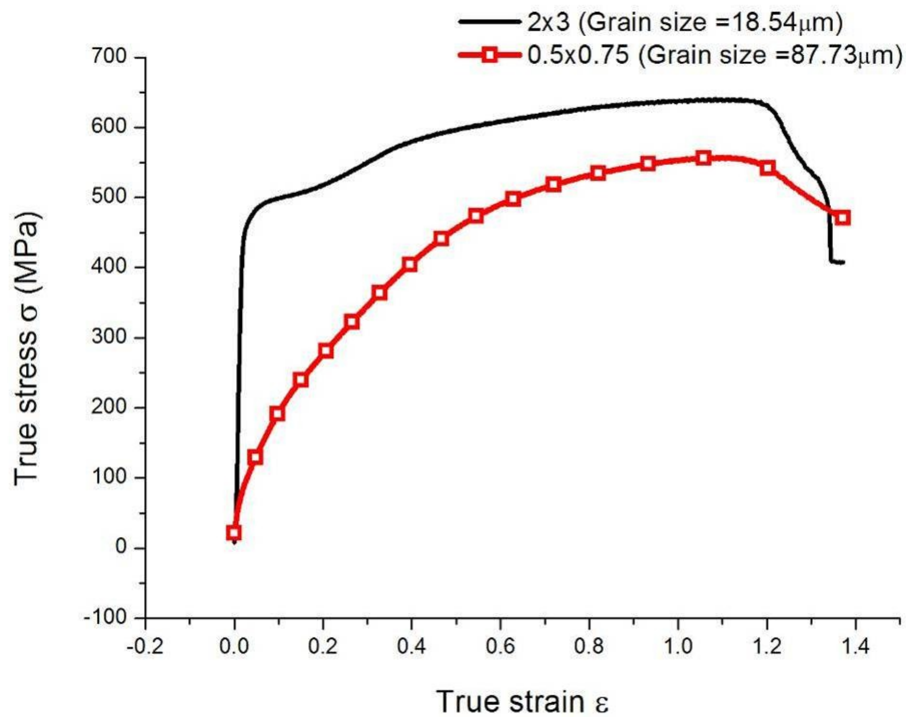

Fig. 3.6. Stress-strain curves generated via simple upsetting experiment.

In order to examine the accuracy of the developed surface layer model, the experimental data, Peng's model and the flow stress curve without consideration of size effect are compared with the model developed in this chapter. By applying different size factors, the flow stress curves are shown in Fig. 3.7. The flow stress curve without consideration of size effect is the conventional model with the size factor $\lambda = 0$. The current surface layer model and Peng's surface layer model are quite similar. The difference in-between is the calculation methodology of $\tau_R(\varepsilon)$ and the definition of the size factor λ. Peng's model is mainly used in micro sheet metal forming and simple upsetting process, while the proposed surface layer model in this chapter is more accurate in the flanged upsetting process as the length of billet is an important parameter and the volume portion of the grains in the top and bottom surfaces cannot be neglected.

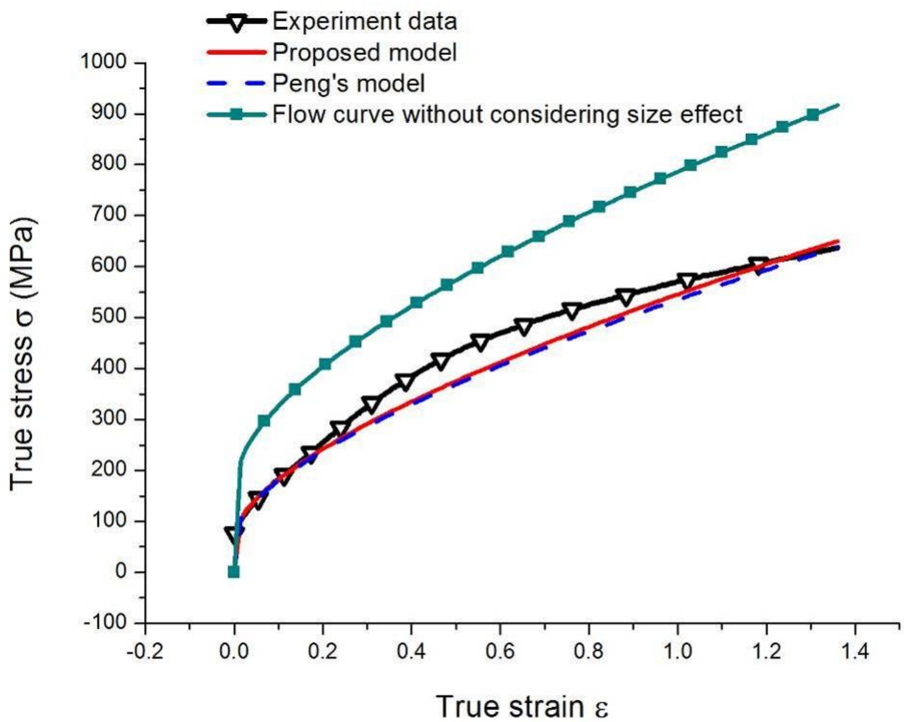

Fig. 3.7. Comparison of the experimental data and different models.

In the curves shown in Fig. 3.7, the flow stress without considering size effect is much higher than the actual experimental result, revealing that the influence of size effect is significant. The flow stress model without considering size effect provides a much higher stress result than the experimental results and other flow stress models. The results of the proposed surface layer model and Peng's surface layer model are quite similar in simple upsetting process as the ratio between the length and diameter is larger than 1, in which the surface volume portion of the grains on top and bottom surfaces can be neglected during forming process.

3.6 Simulation implementation

The purpose of conducting macro-scaled simple upsetting experiment and establishing surface layer model is to obtain a stress-strain curve to predict the fracture behavior of micro-scaled flanged upsetting.

The proposed research can be divided into three stages: the experiment stage, the flow stress and fracture model stage and the CAE simulation stage, as shown in Fig. 3.8. In CAE simulation, the data which is required in material property section all come from the surface layer model and fracture criteria. As has been discussed in previous section, the flow stress data of the macro-scaled simple upsetting will be extracted and input into the surface layer model. By using the fracture criteria, the fracture strain and C value can be generated according to the fracture energy per unit which the specimen absorbs before damage initiation. The results of the expected fracture strain are compared with the actual fracture strain of micro-scaled simple upsetting.

Mesh is implemented according to the requirement of damage evolution function. In compression simulations, which are unlike other microforming processes, mesh must be first applied and a Mesh Part needs to be created before material property being assigned. This is because in the compression simulation, when a mesh element has been damaged and considered as an invalid mesh element, a “blank area” will be formed when the invalid mesh is deleted. As the original boundary condition does not involve this “blank area”, the other elements around this element will overlap with each other when the compression simulation continues. In this simulation, a 4-node bilinear element CAX4R, which is used in simulation with very large mesh distortions, is applied to model the simple upsetting and flanged upsetting sample.

The data which is needed in damage evolution function is extracted in modeling stage. The fracture strain is obtained from the surface layer model in order to demonstrate the absorbed energy per unit during the hardening part of the flow stress curve. In the softening part, however, the flow stress curve cannot represent the material property. To address this issue, damage energy G_f, which is the energy to open a unit area of crack, is adopted in Hillerborg’s proposal [28]. The damage energy to open a unit area can either be found in fracture manual or obtained from a flow stress-displacement curve. By taking into account the mesh sensitivity, the damage evolution law can be specified in terms of damage energy per unit area. When the material stiffness of a damaged element is fully degraded, this invalid element will be removed and the “blank area” left is considered as the result of fracture formation.

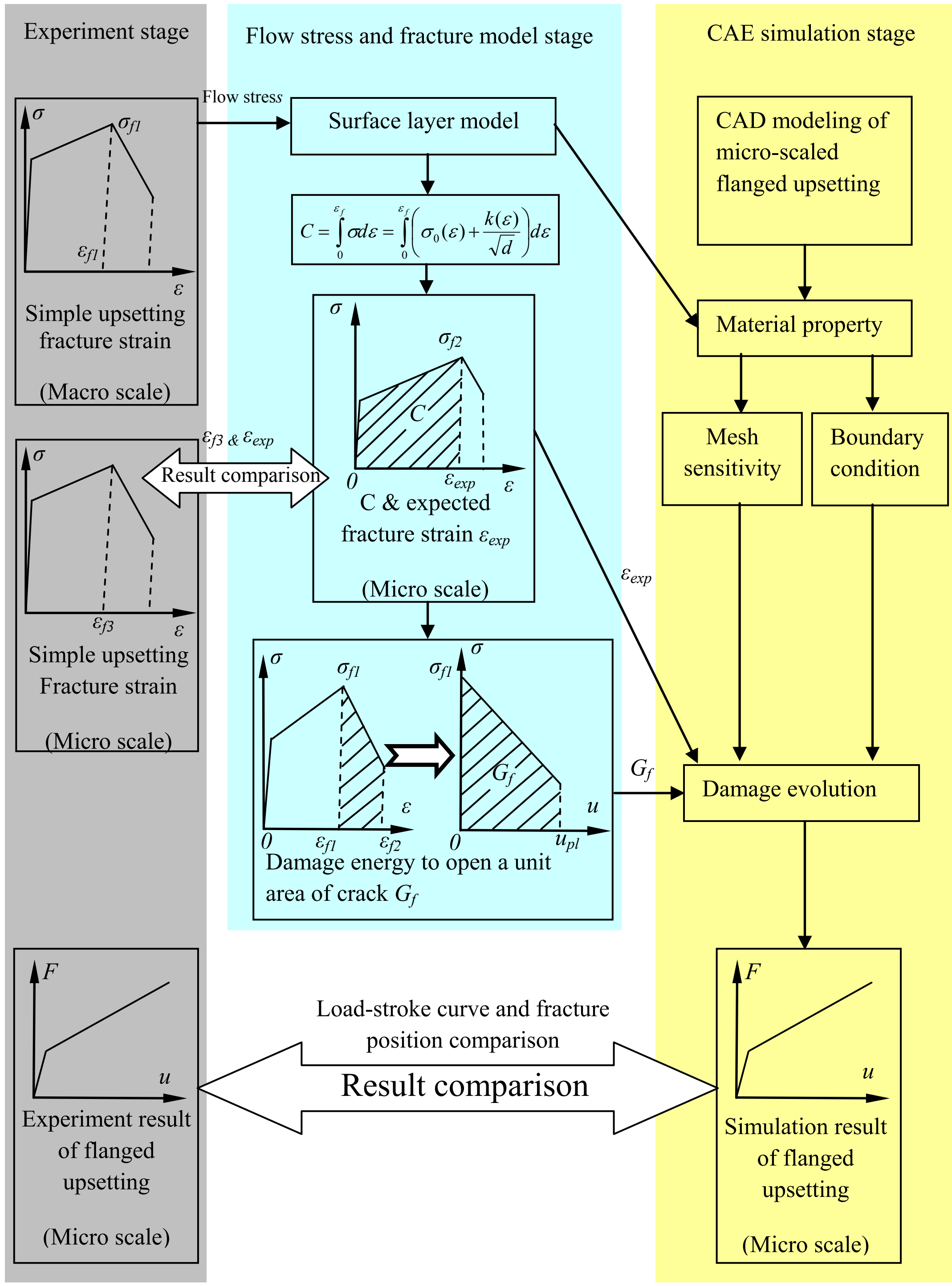

Fig. 3.8. Simulation flow chart.

Finally, when the simulation is over, the predicted result of the micro-scaled flanged upsetting will be compared with the actual experimental result. Load-stroke curve and fracture position comparison will be conducted and the final conclusion of the fracture prediction will be made.

3.7 Experiments

Brass C3602 was used as the testing material in this research. The heat treatment of the specimens was conducted to obtain different microstructures and the heat treatment conditions are presented in Table 3.1. Cylinder samples are annealed at a vacuum condition with different temperatures and holding times, which are $750^{\circ}C$ for 3 hours, $600^{\circ}C$ for 2 hours and $450^{\circ}C$ for 2 hours to obtain different grain sizes. In addition, the metallographic examination is done after the specimen is etched in a solution of 5g of $FeCl_3$, 15ml of HCl and 85ml of H_2O for 15 seconds. The grain sizes were measured correspondingly and also presented in Table 3.1.

Table 3.1 Heat treatment parameters of cold uppseting process.

	Target temperature	Dwelling time	Grain size
Group 1	As-received	As-received	18.54μm
Group 2	$450^{\circ}C$	2h	24.21μm
Group 3	$600^{\circ}C$	2h	45.48μm
Group 4	$750^{\circ}C$	3h	87.73μm

The upsetting experiment was conducted in a MTS testing machine. The tools and specimen were lubricated with machine oil to reduce the friction in between. The punch speed is 0.01*mm/s* to eliminate the strain rate effect.

For the experiment, the original specimens with the dimensions of 2×3, 1×1.5 and 0.5 *mm* ×0.75*mm* are used and their microstructures are shown in Fig. 3.9. These samples are compressed to the height reduction of 75%.

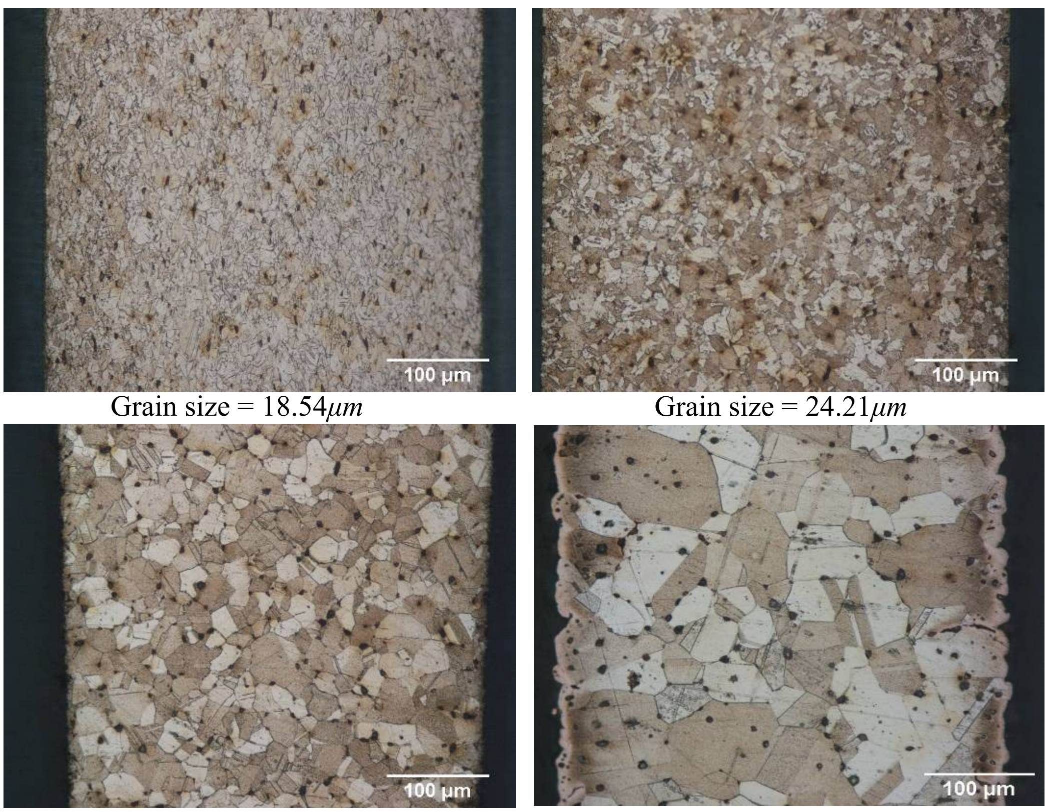

Grain size = 18.54μm Grain size = 24.21μm

Grain size = 45.48μm Grain size = 87.73μm

Fig. 3.9. Microstructures of the billets under different heat treatment conditions.

The flanged upsetting process was then conducted. Scanning electron microscope (SEM) was used to investigate the potential fracture location in the barreling surface predicted by FEM simulation. The specimen was sectioned perpendicular to the bottom surface to study the interior fracture in the workpiece.

Fig. 3.10 shows the die structure and assembly used in this research. The tooling components can be changed to do different micro-upsetting experiments with the specimens of different dimensions. By changing the pins with different sizes, the die can also be used to realize different microforming processes.

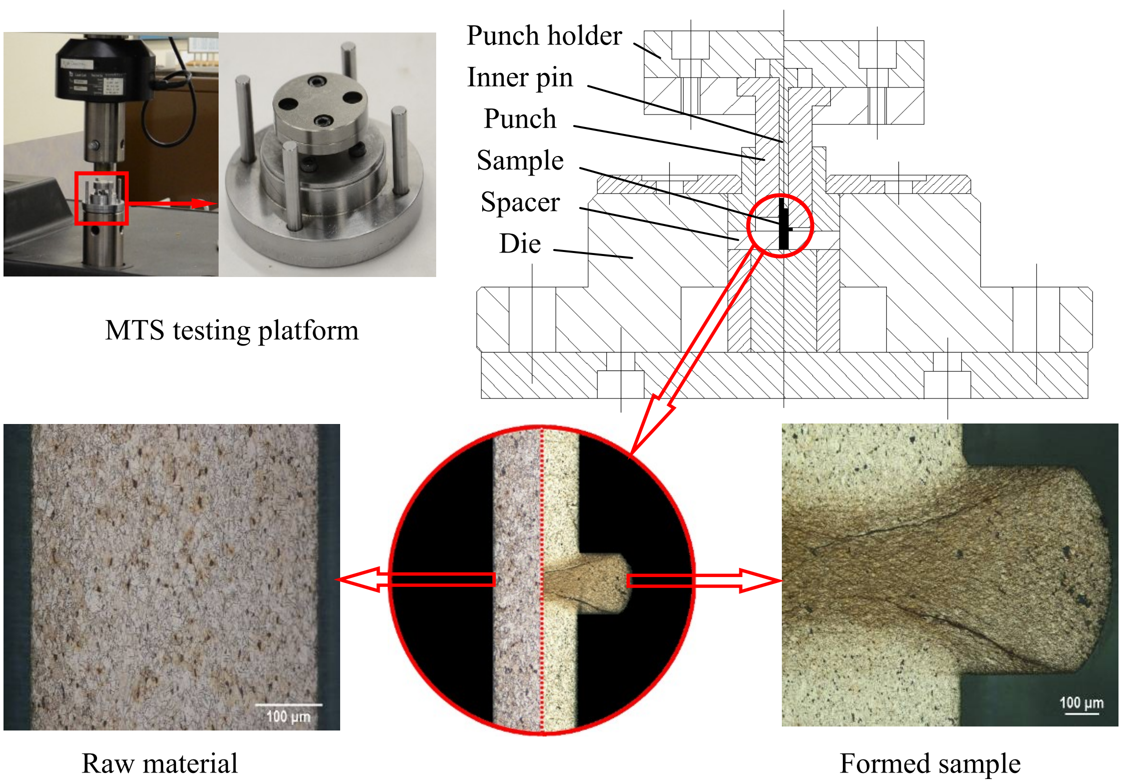

Fig. 3.10. Die assembly for micro-scale flanged upsetting.

3.8 Results and discussion

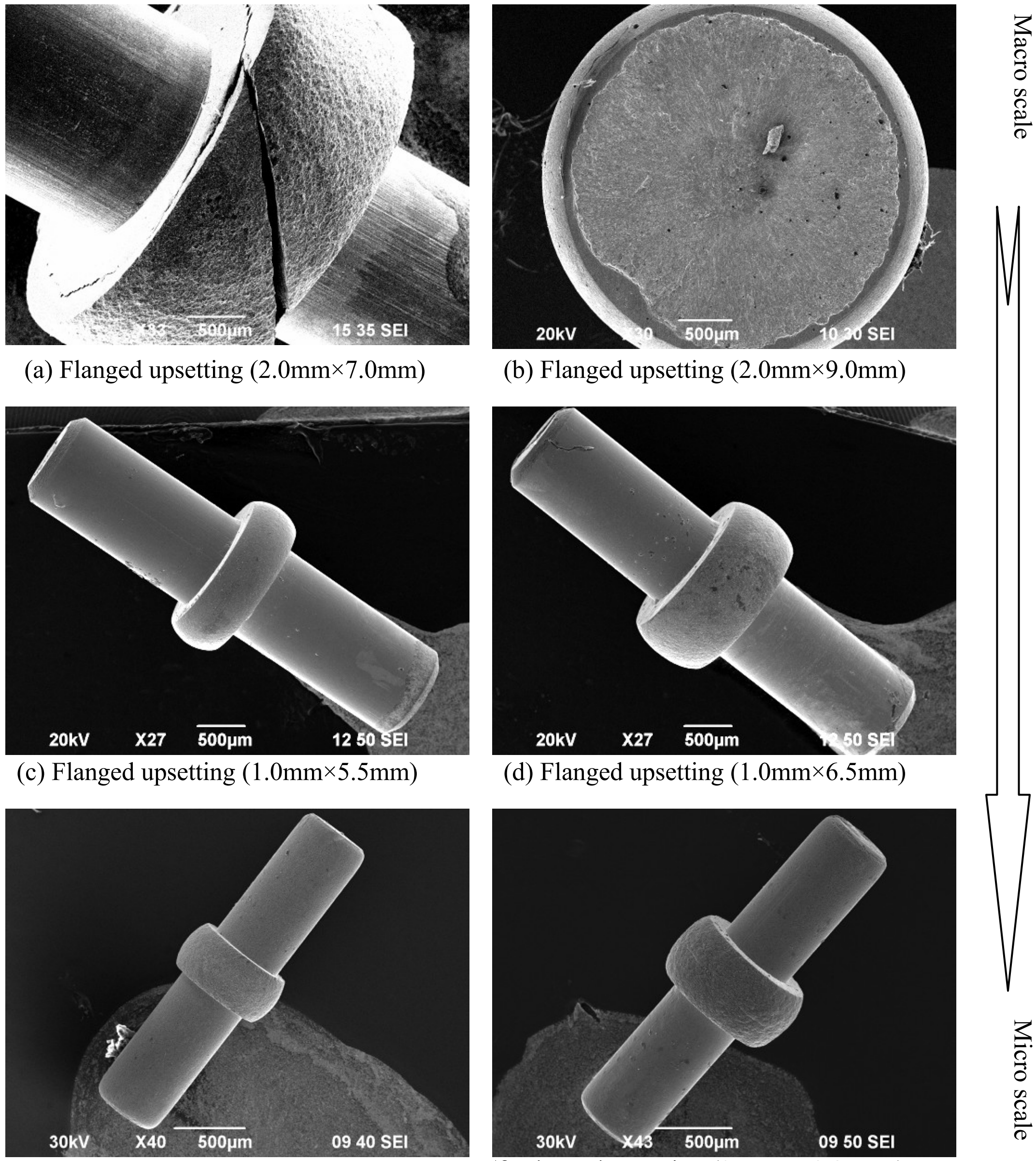

(a) Flanged upsetting (2.0mm×7.0mm)

(b) Flanged upsetting (2.0mm×9.0mm)

(c) Flanged upsetting (1.0mm×5.5mm)

(d) Flanged upsetting (1.0mm×6.5mm)

(e) Flanged upsetting (0.5mm×2.75mm)

(f) Flanged upsetting (0.5 mm×3.25mm)

H/D=1.5:1

H/D=2.5:1

Fig. 3.11. SEM photos for different scales and H/D ratios (the ratio of free height to diameter) in the flanged upsetting. Each sample is compressed with the height reduction of 75%. Samples (a) and (b) are considered as macro-scale flanged upsetting, while (e) and (f) are considered as micro-scale flanged upsetting.

The implementation of macro and micro scale flanged upsetting is shown in Fig. 3.11. The macroscopic crack propagates along one shear band until fracture happens when the stroke reaches its limit with the height reduction of 75%.

In order to determine the size effect in micro-scaled flanged upsetting, simulation of the process was conducted based on the surface layer model and the size independent model. Their corresponding results are further compared with the experiments. From the load-stroke curves presented in Fig. 3.12, it can be seen that the proposed surface layer model is more accurate than the conventional one.

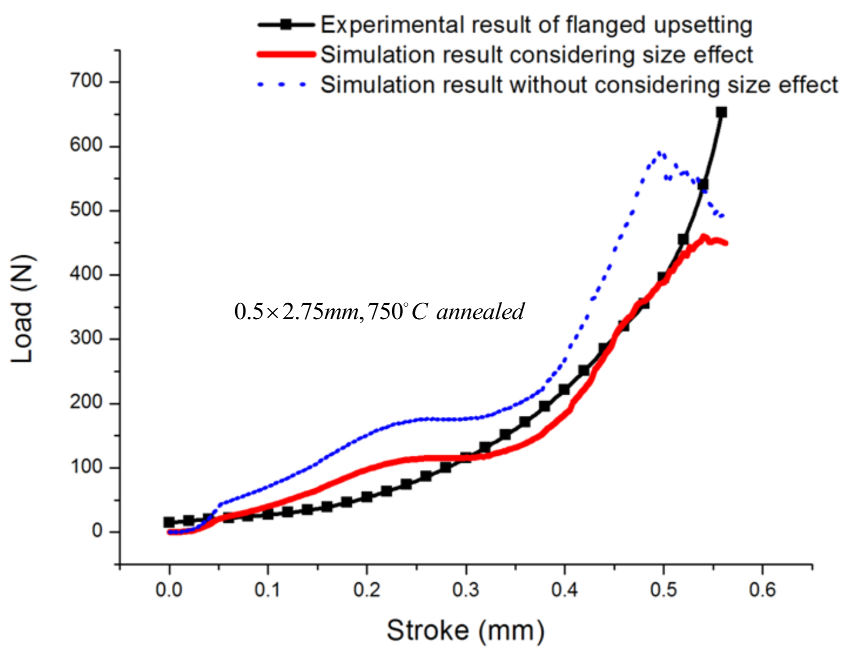

Fig. 3.12. Comparison of the FEM results using the proposed surface layer model and the conventional model.

Fig. 3.13 shows the mechanism of fracture formation in micro-scaled flanged forming process. The picture in the left top corner shows the expected fracture location and the actual defect place of the micro flanged upsetting. In this research, there are two types of energy: The fracture energy is the required energy to start damage initiation, while the damage energy is the required energy from damage initiation till major crack occurs. When the absorbed energy of a mesh exceeds the damage energy, which is obtained from the stress-strain curves determined by the actual experiment, this mesh will be considered as an invalid one. And the Young's modules of these invalid meshes will be automatically set to a very small value and become invisible in simulation. The blank area is used to represent those failed elements. In the figure, a slight difference between the actual experimental and simulation result can be found at the bottom of the flange. This is mainly caused by the mesh distortion of the model. The typical shear dimple is found at the fracture section of the specimen. When the punch contacts the top surface of the specimen, the material in the main deformation area, viz., the flanged part, flows in two opposite directions along the shear bands, as shown in Fig. 3.13, which tallies with the research done by Saanouni et al. [34]. The step-like elongated dimples are formed in the two fracture surfaces in the broken specimen.

In macro upsetting process, the specimen dimension is much larger than grain size and the size factor is approximately equal to zero. In micro flanged upsetting process, the deformation is much easier to initiate and the ductility of the specimen decreases accordingly with the increase of grain size, which is caused by the reduction of grain boundary constraint as the total amount of grain boundaries is reduced accordingly. This is because the grain boundary in polycrystalline acts as a barrier of dislocation movement in polycrystalline. When the grain size increases due to heat treatment, less grain boundaries exist in this specimen. Thus, there are fewer barriers which makes deformation easier.

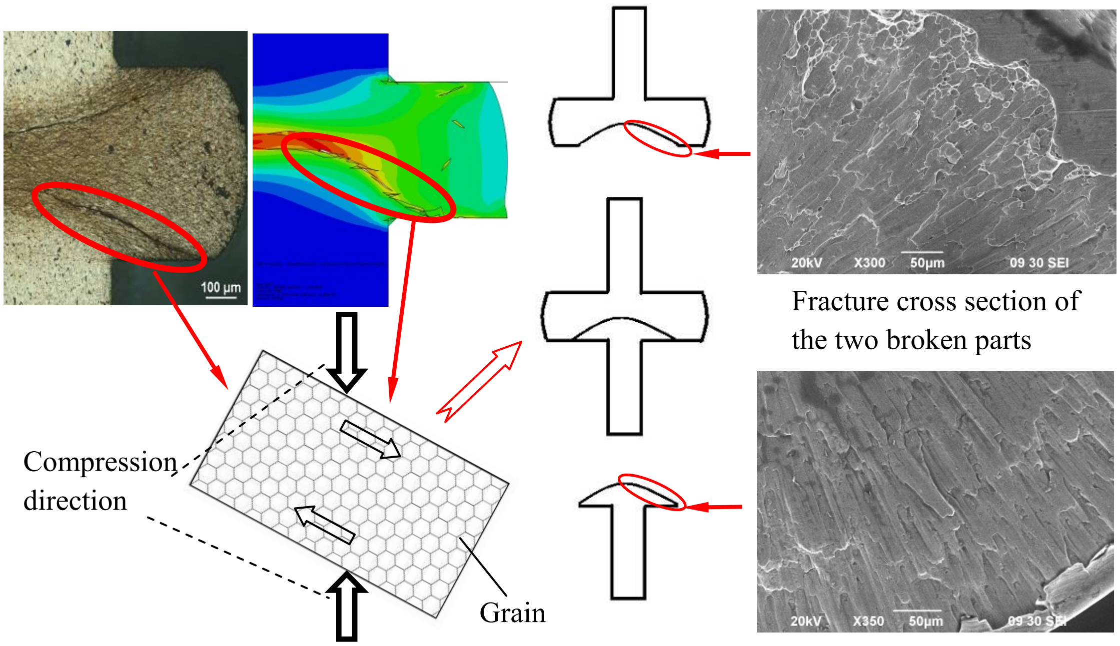

Fig. 3.13. Shear fracture in the micro-scaled flanged upsetting process.

To predict the fracture in macroforming, damage evolution is judged by the fracture energy, which is considered as constant for the same material. Freudenthal defined this constant with the fracture stress and equivalent strain [35-37]. Using Hall-Petch equation and Armstrong's methodology, the damage evolution equation can be re-designated in the following equation proposed in this research:

$$C = \int_0^{\varepsilon_f} \sigma d\varepsilon = \int_0^{\varepsilon_f} \left(\sigma_0(\varepsilon) + \frac{k(\varepsilon)}{\sqrt{d}} \right) d\varepsilon \tag{3.9}$$

As discussed above, when the size effect is considered in microforming process, the surface layer model established above is more accurate compared with the conventional macroforming model. Therefore, the damage evolution equation can be represented in the following form.

$$C = \int_0^{\varepsilon_f} \left(\sigma_{ind} + \sigma_{dep} \right) d\varepsilon = \int_0^{\varepsilon_f} \left(M\tau_R(\varepsilon) + \frac{k(\varepsilon)}{\sqrt{d}} + \lambda \left(m\tau_R(\varepsilon) - M\tau_R(\varepsilon) - \frac{k(\varepsilon)}{\sqrt{d}} \right) \right) d\varepsilon \tag{3.10}$$

For the material annealed with the same heat treatment process and having a strain gradient during experiment, it should follow the fracture criterion in Eq. (3.11) with the same C. Figs. 3.14 to 3.16 present the relationship between the expected strain when achieving the maximum stress and the actual strain under the same heat treatment condition. In these figures, the vertical lines represent the existence of the maximum flow stress during the deformation. The area, which is formed by the vertical lines indicated in the figures, the stress-strain curves and the coordinate axis, represents the energy the specimen absorbed in the hardening process.

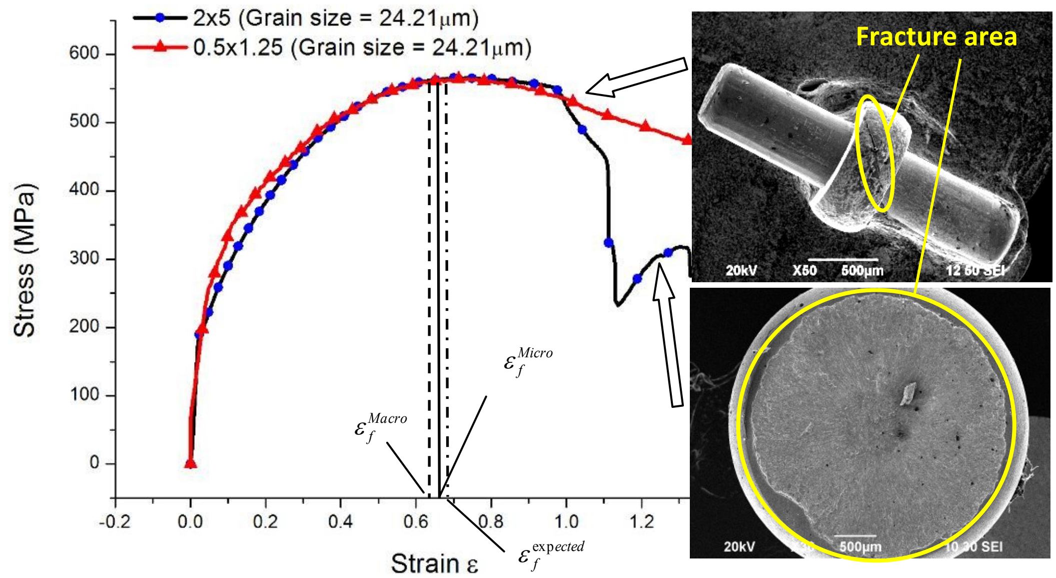

Fig. 3.14. The expected and the actual maximum fracture strains of the brass annealed at $450^{\circ}C$.

In Eq. (3.11), the first one represents the fracture criterion of macro-scaled forming and the second one is for micro-scaled forming. The fracture factor C and the grain size d in both the macro and micro scaled specimens are all the material constants with the same value. By solving Eq. (3.11), the relationship of the fracture strain in macro and micro scales is obtained and the prediction of micro scaled fracture strain can be made. As shown in Fig. 3.14, when the grain size equals to 24.21μm, the micro scaled fracture strain $\varepsilon_f^{\exp ected} = 1.07\varepsilon_f^{Macro}$. And in Fig. 3.15, it can be predicted that the micro-scaled fracture strain $\varepsilon_f^{\exp ected} = 1.09\varepsilon_f^{Macro}$. This explains the reason why the micro fracture is difficult to form in micro scaled plastic deformation process.

$$\begin{cases} C = \int_0^{\varepsilon_{f1}} (\sigma_{ind} + \sigma_{dep}) d\varepsilon = \int_0^{\varepsilon_{f1}} \left(539.53\varepsilon^{0.68} + d^{-\frac{1}{2}}.73.09\varepsilon^{0.06} + \eta_1 \cdot \left(352.64\varepsilon^{0.68} - 539.53\varepsilon^{0.68} - d^{-\frac{1}{2}}.73.09\varepsilon^{0.06} \right) \right) d\varepsilon \\ C = \int_0^{\varepsilon_{f2}} (\sigma_{ind} + \sigma_{dep}) d\varepsilon = \int_0^{\varepsilon_{f2}} \left(539.53\varepsilon^{0.68} + d^{-\frac{1}{2}}.73.09\varepsilon^{0.06} + \eta_2 \cdot \left(352.64\varepsilon^{0.68} - 539.53\varepsilon^{0.68} - d^{-\frac{1}{2}}.73.09\varepsilon^{0.06} \right) \right) d\varepsilon \end{cases} \quad (3.11)$$

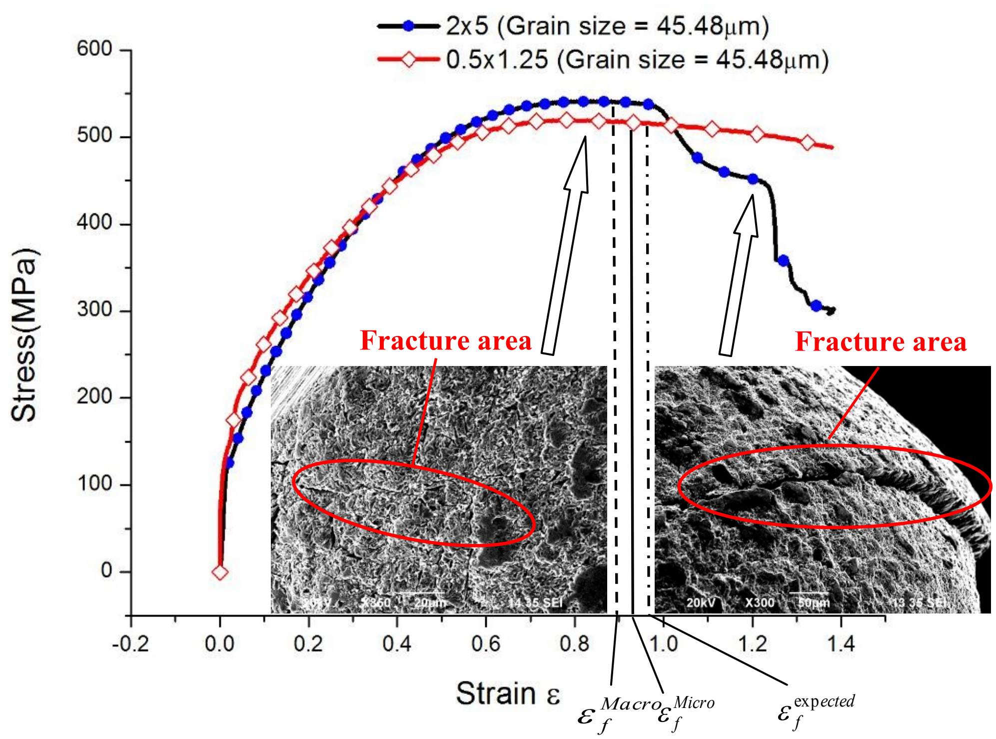

Fig. 3.15. The expected and the actual maximum fracture strain of brass annealed at $600^{\circ}C$.

In Fig. 3.16, the maximum fracture strain is determined as $\varepsilon_f^{\exp ected} = 1.28\varepsilon_f^{Macro}$ using Eq. (3.11). With the height reduction of 75% in upsetting deformation, the micro scaled specimen is difficult to break due to the contribution of size effect. However, it is also obvious that the actual maximum fracture strain of the micro scaled specimens is much larger than the expected fracture strain. This can be illustrated by the SEM photos shown in Fig. 3.16. In the SEM photos, although the micro fractures are observed on the barreling surface of specimen, the continuous fracture has not yet formed when the strain reaches the maximum fracture strain. This may be due to the error caused by the friction force between the specimen and the die.

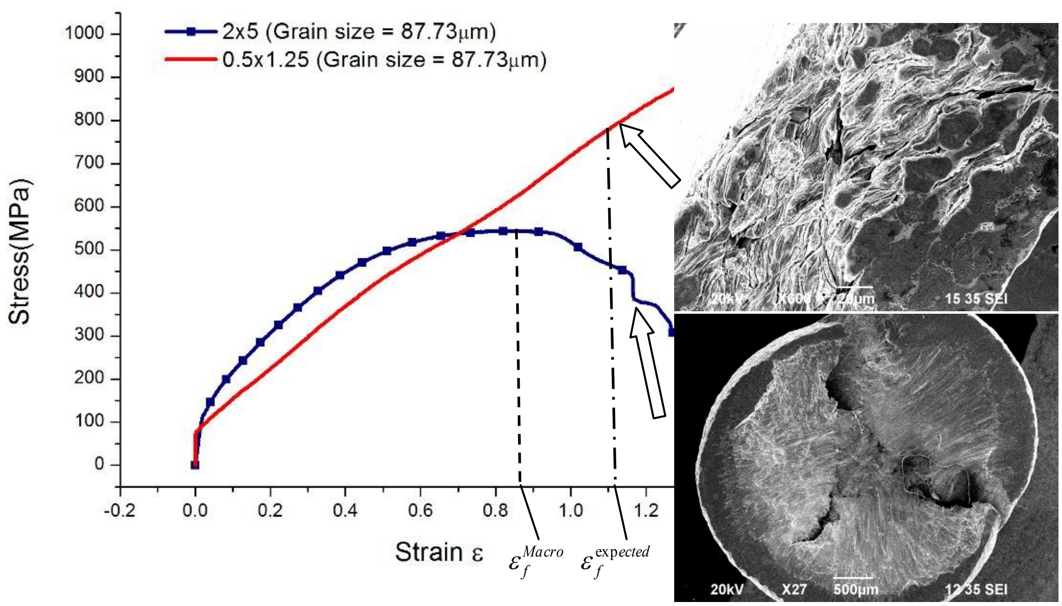

Fig. 3.16. The expected and the actual maximum fracture strain of brass annealed at $750^{\circ}C$.

With the support of experimental results, the stress without consideration of size effect is much higher than the size dependent one. As the damage energy is considered as the same, the fracture strain predicted by the size dependent model is believed to be larger than that of the size independent model [28]. Therefore, a larger deformation is needed in micro-scaled flange upsetting to reach its damage evolution energy.

Figs. 3.17 and 3.18 illustrate the simulation and experimental results of the macro and micro flanged upsetting. In Fig. 3.17, two fractures are found on the surface of the macro scale specimen. The fracture located at the barreling surface with about 45 degrees to the axis direction of the sample is considered as the main fracture. The other is the second fracture located at the flanged surface perpendicular to the sample axis. The simulation results show that when the main fracture is initiated and grows to a certain level, the second fracture will happen.

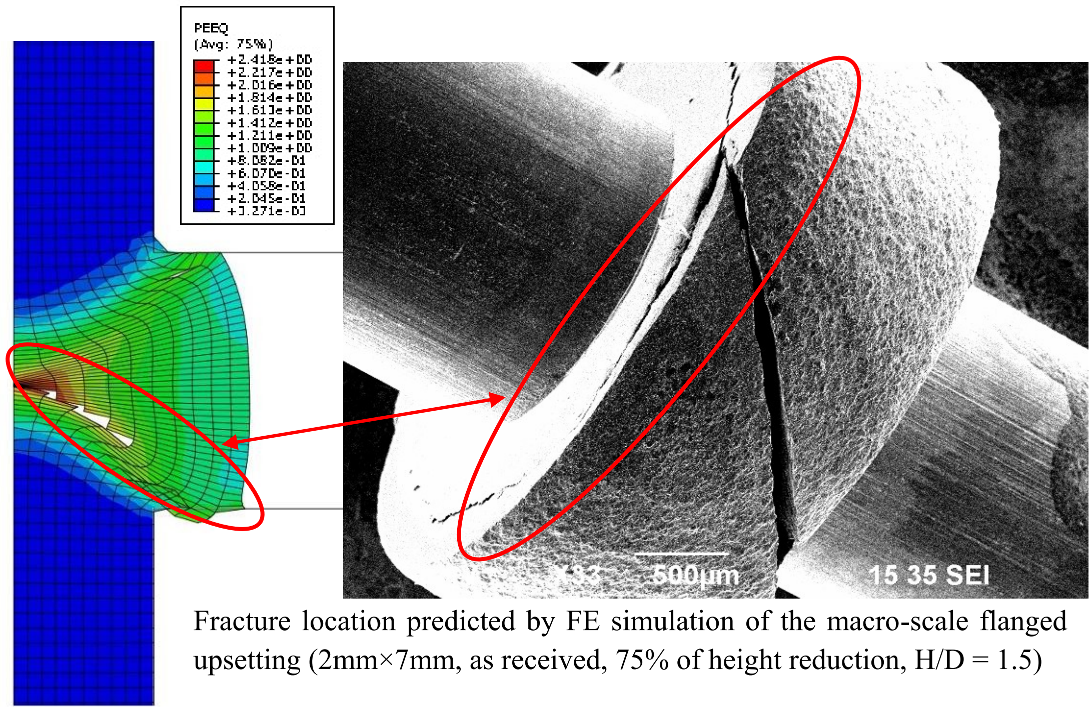

Fracture location predicted by FE simulation of the macro-scale flanged upsetting (2mm×7mm, as received, 75% of height reduction, H/D = 1.5)

Fig. 3.17. The experimental and simulation results of the macro-scaled flanged upsetting.

As discussed before, fracture is more difficult to form in micro-scaled specimen. The pictures in Fig. 3.18 are the SEM photo and FEM simulation of the micro-scaled specimen with H/D = 1.5 and the dimensions of 0.5mm ×2.75mm and the height reduction of 75%. From the picture, it can be found that there is no continuous ductile fracture existing on the barreling surface or the flange surface in micro-scaled forming. Compared with the simulation result of the macro-scaled flanged part, the equivalent strain of the micro-scaled flanged part in the shear band is smaller than that in macro-scaled case with the same height reduction percentage. According to the explanation of Fig. 3.16, the damage initiation in the micro part will occur only when the specimen undergoes more deformation. The simulation result and SEM photo are the direct result of ductile fracture formation affected by size effect.

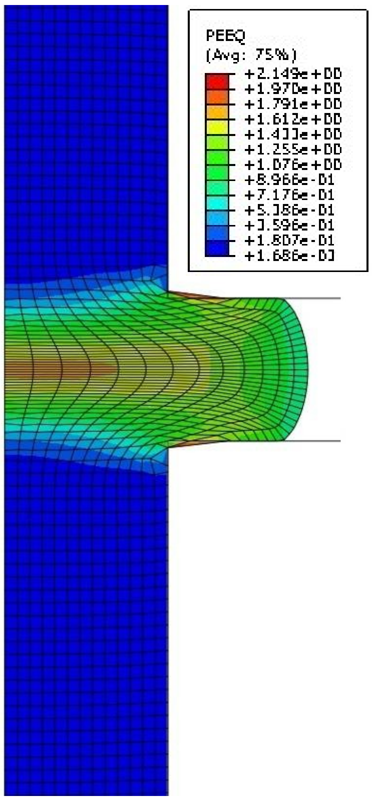

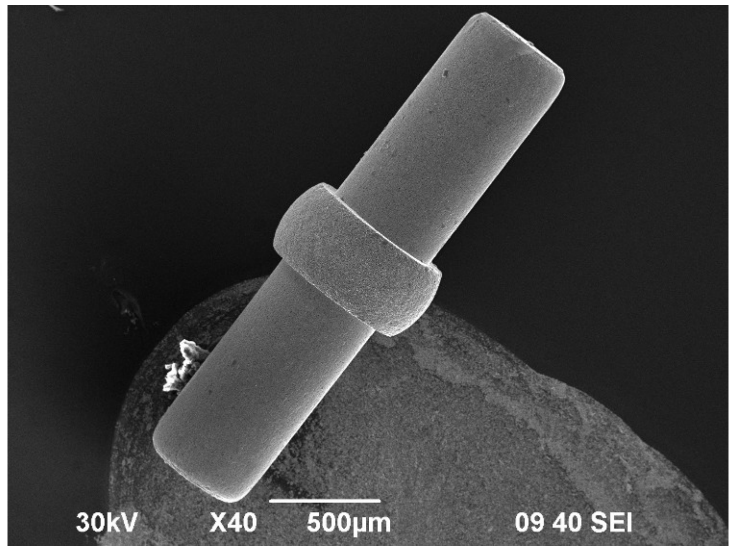

The samples with the dimension of 0.5mm×2.75mm, annealed at 750℃ and compressed with the height reduction of 75%, H/D = 1.5.

Fig. 3.18. The experimental and simulation results of the micro-scaled flanged upsetting.

Fig. 3.19 shows the fractography of the specimen with different scaling factors. The image on the left illustrates the fractography of specimen without heat-treatment. The fracture is transgranular and the dimple size is quite different. The image on the right is a shear fracture showing the elongated shear dimples with uniform distribution [38].

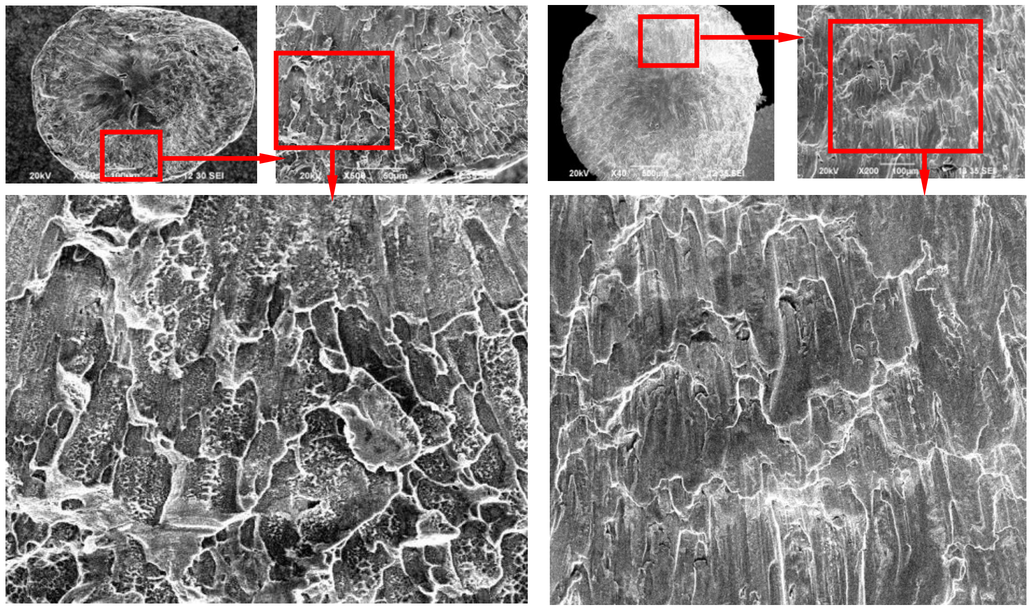

Grain size = 18.54μm　　　　Grain size = 87.73μm

Fig. 3.19. Fractography of the samples with different grain sizes.

3.9 Summary

The size effect is considered as an important factor in microforming processes, which affects micro fracture formation in the process. In this chapter, a size-effect-based surface layer model is developed to predict the fracture formation in micro-scaled plastic deformation processes. Using micro flanged upsetting process as a case study process, the proposed model is implemented and FEM simulation is conducted via ABAQUS. The physical experiments are also done. Based on the experimental results, it is found that the simulation results using the proposed surface layer model are more accurate than that of the conventional mathematical models. The following concluding remarks can thus be drawn:

1. In micro-scaled forming, it is hard to reach the damage energy when applying the same equivalent strain as in macroforming. The fracture on the flange surface is easier to form in the large scale flanged upsetting process.
2. The result of flow stress curve generated based on this model is similar to Peng's model when the ratio of height to diameter of the cylinder specimen is large. However, the proposed model is more accurate in dealing with the specimen with the H/D ratio less than 1.5:1.
3. Fractography illustrates that the step-like elongated shear dimples exist in the two fracture surfaces of the broken flanged part. The dimple size on the transgranular fractures surfaces is affected by different scaling factors. The existence of these fracture behaviors is caused by size effect.
4. Axisymmetrical flanged parts are widely used in industries and their fracture behaviors in microforming need to be investigated. Through this study, the size effect in microforming is found to have a significant effect in forming and fracture formation process. According to simulation and experiment results in simple upsetting and flanged upsetting, the ductility of micro scaled parts are much better than macro parts. This is because the reduction of feature size has increased the proportion of surface grains, which have more free surface than internal grains in plastic deformation.

Chapter 4 Hybrid Constitutive Fracture Model for Microforming

4.1 Introduction

As a critical issue in micro-scaled plastic deformation, viz., microforming, the effects of workpiece geometry and material grain sizes on ductile fracture behavior have been studied. However, the flow stress contribution of each phase in multiphase alloys to the ductile fracture and deformation behaviors in microforming has not yet been fully addressed. In this chapter, a hybrid model is proposed for modeling and representing the fracture and deformation behaviors in microforming processes. The proposed model can be used to calculate fracture energy and then predict the fracture strain of the alloys with single- or multi-phase. The model is proven to be more accurate in fracture prediction as it considers the influence of size effect over material fracture energy. Using brass C3602 with different grain sizes obtained via heat treatment as the testing material, the grain and feature size effects are investigated. Through the finite element simulation by using the developed hybrid model and physical experiment, the methodology to represent and model the influence of metal phase over deformation and fracture behaviors in micro-scaled plastic deformation of multiphase alloys is presented. Also, to compare the difference between grain and geometry size effects, the stress-induced fracture map, which articulates the relationship of size effect, fracture energy and the expected fracture strain in microforming, is proposed.

In Chapter 3, a constitutive flow stress model, which can represent the fracture deformation behavior in most micro-scaled deformation scenarios, is developed. The simulation results, however, do not have a good agreement with the actual experimental results when the size factor λ, which is defined as the percentage of surface grains in all the grains of the deformation body, is larger than 58%. As Hall-Petch equation is employed in the constitutive model, the fracture prediction is reliable for single phase alloy. For multiphase alloys, which may contain both BCC and FCC structures, they have not been considered in this model. The objective of this chapter is thus to establish a hybrid model to represent the influence of different phases of the materials over their micro-scaled deformation behaviors, especially for the ductile fracture deformation in microforming processes, via, simulation and experiment. The model is implemented in FE simulation and verified by experiment.

4.2 Hybrid flow stress modeling and research methodology

Stress modeling is important in micro-scaled fracture prediction. The most important issue of flow stress modeling is to distinguish the contribution of size effect in the macro- and micro-scaled scenarios in this research. The proposed hybrid flow stress modeling introduces the size factor λ to the conventional stress model. Thus the flow stress in micro-scaled deformation can be more accurately described.

4.2.1 Macro-scaled flow stress modeling

In forming process, the flow stress σ can be represented by the micro-scaled shear stress τ in the following [39]:

$$\sigma = M\tau \tag{4.1}$$

where M is the Taylor factor, which is not related to the grain size of material [40]. Generally, the flow stress model needs to consider two parts of contribution. One is the grain size independent part and the other is the dependent part [39]. The famous Hall-Petch equation is established by considering both the two parts:

$$\sigma = \sigma_0 + kd^{-\frac{1}{2}} \tag{4.2}$$

where σ_0 is a material constant representing the stress of single crystalline, k is also a material constant and d is the grain size [41].

For the Armstrong's model in the following, it considers the flow stress at a certain strain and takes the form of:

$$\tau(\varepsilon) = \tau_0(\varepsilon) + k(\varepsilon)d^{-\frac{1}{2}} \tag{4.3}$$

In Eq. (4.3), $\tau_0\left(\varepsilon\right)$ and k are constants for a given strain. Eq. (4.1) is then designated as:

$$\sigma\left(\varepsilon\right)=M\left(\tau_0\left(\varepsilon\right)+k(\varepsilon)d^{-\frac{1}{2}}\right) \tag{4.4}$$

Eq. (4.4) is used to calculate the macro-scaled flow stress in Peng's research and Ran's work [3,29]. Based on the crystal plasticity theory, shear stress $\tau\left(\varepsilon\right)$ can be represented by the lattice friction stress $\tau_0\left(\varepsilon\right)$ and the interaction among dislocations in the following [12]:

$$\tau\left(\varepsilon\right)=\tau_0\left(\varepsilon\right)+\alpha\mu b\sqrt{\rho_T} \tag{4.5}$$

In Eq. (4.5), α is a particular constant for the phase of alloy and describes the dislocation interaction. μ is the corresponding shear module for different phases. b is the Burgers vector and different for FCC and BCC phases. ρ_T is the total dislocation density. To explain the strengthening effect, which is related to the grain size change, Ashby (1970) proposed a model which classifies the dislocations into statistically stored dislocation density $\rho_s\left(\varepsilon\right)$ and geometrically necessary dislocation density $\rho_G\left(\varepsilon\right)$. The statistically stored dislocation density is considered as a monotonic function and represented as:

$$\rho_s\left(\varepsilon\right)=\frac{C_2\varepsilon}{bL^s} \tag{4.6}$$

where C_2, ε, b and L^s are the material constant, strain, Burgers vector and slip length, respectively [39]. The geometrically necessary dislocation density is generally expressed as:

$$\rho_G(\varepsilon) = \frac{C_1 \varepsilon}{bd} \tag{4.7}$$

where C_1 is the material constant. Therefore, the total dislocation density takes the following form:

$$\rho_T = \rho_s(\varepsilon) + \rho_G(\varepsilon) = \rho_s(\varepsilon) + \frac{C_1 \varepsilon}{bd} = \frac{C_2 \varepsilon}{bL^s} + \frac{C_1 \varepsilon}{bd} \tag{4.8}$$

When there is almost no coarse grain in the deformation body, the grain boundary strengthening becomes critical in the deformation. This means the influence of the statistically stored dislocation can be neglected, viz., $\rho_s(\varepsilon) \approx 0$. In Eq. (4.4), it is known that $\sigma_0(\varepsilon)$ is equivalent to $M\tau_0(\varepsilon)$ and can be described by an exponential function of $y = k\varepsilon^n$. Thus, the constitutive model for a single phase metal in macro-scaled deformation is proposed in Eq. (4.9).

$$\sigma(\varepsilon) = M\left(\tau_0(\varepsilon) + \alpha\mu b\sqrt{\rho_s(\varepsilon) + \frac{C_1 \varepsilon}{bd}}\right) = Mk_1\varepsilon^{n_1} + \alpha M\mu b\sqrt{\frac{C_1 \varepsilon}{bd}} \tag{4.9}$$

Compared with the previous model developed and presented in Chapter 3, the present constitutive model specifically articulates the form of $k(\varepsilon)d^{-\frac{1}{2}}$ instead of using the curve fitting approach. The model in Eq. (4.9) has been proven to be valid for single phase alloys. For multiphase alloys, the coefficients μ, b and C_1 in Eq.

(4.9) are different for each phase. The flow stress can be combined with the stress of each phase by adding the volume fraction of each phase and designated as:

$$\sigma = \sum \sigma_i f_j \tag{4.10}$$

Eq. (4.10) is the multiphase mixture rule in which σ_i and f_j are the corresponding stress and the volume fraction of each phase, respectively.

4.2.2 Hybrid constitutive model

As mentioned in Chapter 3, the flow stress of the deformation material can be expressed as:

$$\sigma = \frac{N_s\sigma_s + N_i\sigma_i}{N} = \eta\sigma_s + \left(1-\eta\right)\sigma_i, \left(N = N_s + N_i, \lambda = \frac{N_s}{N}\right) \tag{4.11}$$

where σ and N are the total flow stress and the grain number; the flow stress and grain number of the surface grains are N_s and σ_s, while N_i and σ_i for the internal grains. The independent stress-strain relationship is as follows:

$$\begin{cases} \sigma_s\left(\varepsilon\right) = m\tau_0\left(\varepsilon\right) = mk_1\varepsilon^{n_1} \\ \sigma_i\left(\varepsilon\right) = \sigma_\alpha f_\alpha + \sigma_\beta\left(1-f_\alpha\right) \\ \qquad = \left(Mk_2\varepsilon^{n_2} + \alpha M\mu_\alpha b_\alpha\sqrt{\dfrac{C_1\varepsilon}{b_\alpha d}}\right)f_\alpha + \left(Mk_2\varepsilon^{n_2} + \alpha M\mu_\beta b_\beta\sqrt{\dfrac{C_2\varepsilon}{b_\beta d}}\right)\left(1-f_\alpha\right) \\ \qquad = Mk_2\varepsilon^{n_2} + f_\alpha\alpha M\mu_\alpha b_\alpha\sqrt{\dfrac{C_1\varepsilon}{b_\alpha d}} + \left(1-f_\alpha\right)\alpha M\mu_\beta b_\beta\sqrt{\dfrac{C_2\varepsilon}{b_\beta d}} \end{cases} \tag{4.12}$$

where σ_α, σ_β, f_α and f_β are the stress and volume fraction of α phase and β phase; m is the grain orientation factor. By combining Eqs. (4.11) and (4.12), the final formulation of the hybrid model is thus obtained:

$$\begin{aligned}\sigma_{total}(\varepsilon) &= Mk_2\varepsilon^{n_2} + f_\alpha \alpha M \mu_\alpha b_\alpha \sqrt{\frac{C_1\varepsilon}{b_\alpha d}} + (1-f_\alpha)\alpha M \mu_\beta b_\beta \sqrt{\frac{C_2\varepsilon}{b_\beta d}} \\ &+\lambda\left(mk_1\varepsilon^{n_1} - \left(Mk_2\varepsilon^{n_2} + f_\alpha \alpha M \mu_\alpha b_\alpha \sqrt{\frac{C_1\varepsilon}{b_\alpha d}} + (1-f_\alpha)\alpha M \mu_\beta b_\beta \sqrt{\frac{C_2\varepsilon}{b_\beta d}}\right)\right)\end{aligned} \tag{4.13}$$

Eq. (4.13) is suitable for both the macro- and micro-scaled deformation when there are only few coarse grains in the specimen. For the processed specimens with heat treatment, the contribution of grain boundary to dislocation density is small as the grain becomes coarse and the volume of grain boundary is smaller. Thus, the effect of statistically stored dislocation cannot be ignored and Eq. (4.13) is further formulated as:

$$\begin{aligned}\sigma_{total}(\varepsilon) &= Mk_2\varepsilon^{n_2} + f_\alpha \alpha M \mu_\alpha b_\alpha \sqrt{\frac{C_3\varepsilon}{b_\alpha L^s} + \frac{C_1\varepsilon}{b_\alpha d}} + (1-f_\alpha)\alpha M \mu_\beta b_\beta \sqrt{\frac{C_3\varepsilon}{b_\beta L^s} + \frac{C_2\varepsilon}{b_\beta d}} \\ &+\lambda\left(mk_1\varepsilon^{n_1} - \left(Mk_2\varepsilon^{n_2} + f_\alpha \alpha M \mu_\alpha b_\alpha \sqrt{\frac{C_3\varepsilon}{b_\alpha L^s} + \frac{C_1\varepsilon}{b_\alpha d}} + (1-f_\alpha)\alpha M \mu_\beta b_\beta \sqrt{\frac{C_3\varepsilon}{b_\beta L^s} + \frac{C_2\varepsilon}{b_\beta d}}\right)\right)\end{aligned} \tag{4.14}$$

where C_3 is a material constant.

4.3 Research methodology

Fig. 4.1 schematically illustrated the methodology to establish the hybrid model for ductile fracture analysis of multiphase alloys. In this figure, the macro-scaled material properties are obtained from the load-stroke curve via simple upsetting experiment. The flow stress curve of the material can then be calculated. By observing the microstructure and using energy dispersive X-Ray spectroscopy (EDX), the volume fraction of each phase in the multiphase alloys can be obtained. The coefficient of the macro-scaled constitutive model of the multiphase materials is thus calculated using curve fitting based on the data of volume fraction and flow stress curve. To identify the influence of size effect, the macro-scaled constitutive model is implemented into the surface layer model. The surface layer model introduces the size factor λ into the macro-scaled constitutive model to describe the influence of size effect in micro-scaled forming. The final form of this hybrid model can be used to calculate the flow stress of all the other scenarios of the multiphase materials. For ductile fracture prediction, the fracture energy C is calculated based on this hybrid constitutive model. After that, it goes to FE simulation stage. In this stage, the meshing of computer-aided design (CAD) model is conducted and the boundary condition is set up. The damage energy G_f obtained from the flow stress-displacement curve is applied to the material property so that the damage evolution behavior of the material can be demonstrated during the deformation process. Finally, the load-stroke curve of the flanged upsetting simulation is extracted for the result comparison with the actual experiment.

In most of the previous researches, the influence of feature and grain size effects is considered separately and no report is found so far on revealing of the interaction and interplay of these two size effects in micro-scaled ductile fracture. The so-called Stress-induced Fracture Map (SFM) is generated in this chapter for micro-scaled fracture prediction. SFM schematically articulates the interaction relationship among the size effect, fracture energy and the expected fracture strain in micro-scaled plastic deformation of the multi-phase alloys. It can be used to reveal the influence level of different size effects with the same size factor. The expected fracture strain of the multiphase alloys in different scenarios can thus be predicted. Finally, the load-stroke curve of the micro-scaled flanged upsetting generated by FE simulation based on the established hybrid model is compared with the experiment results to verify the efficiency of the developed hybrid model.

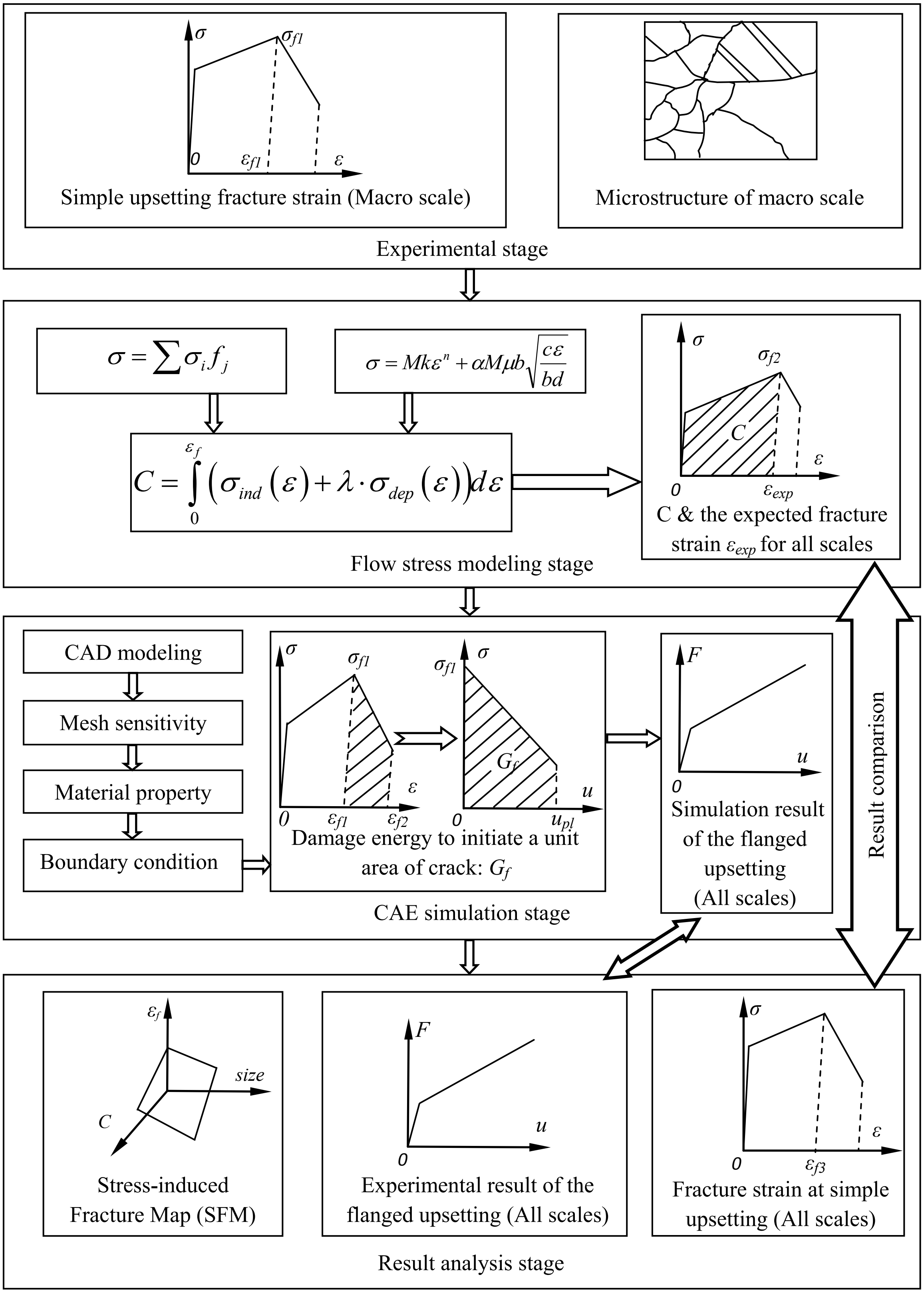

Fig. 4.1. Research methodology of the hybrid fracture method.

4.4 Experiment

Brass C3602 is selected as the testing material for multiphase alloys. The material was annealed to obtain different microstructures. The annealing was conducted in a protective Argon atmosphere with different temperatures and holding times, which are $750^{\circ}C$ for 3 hours, $600^{\circ}C$ for 2 hours and $450^{\circ}C$ for 2 hours, to get different microstructures and grain sizes. In addition, the metallographic examination is done to observe microstructure after the specimen is etched in a solution of $5g$ of $FeCl_3$, 15ml of HCl and $85ml$ of H_2O for 15 seconds. The original specimens have the dimensions of 2×3 *mm* and 0.5×0.75 *mm*. The grain sizes of the samples are 18.54, 24.21, 45.48 and 87.73 μm and shown in Fig. 4.2.

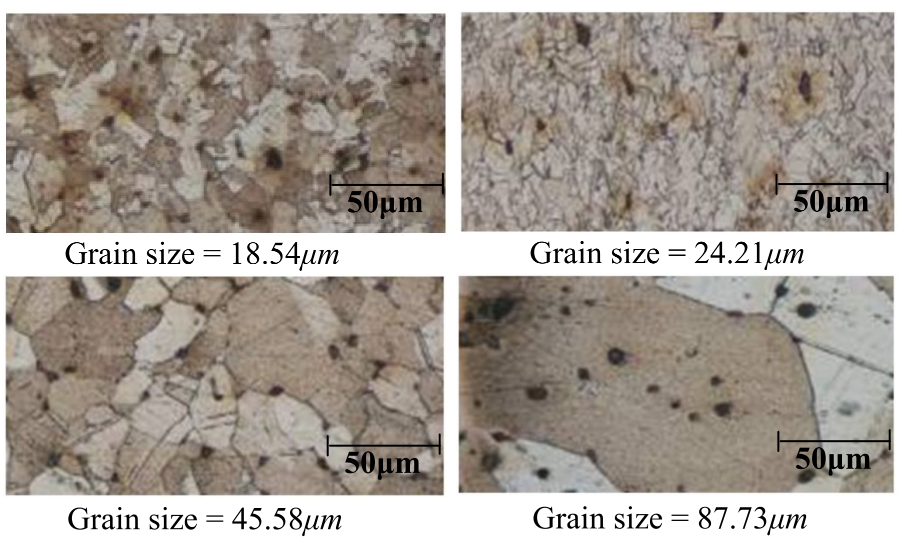

Fig. 4.2. Microstructures of the Brass C3602 billets using different heat treatment conditions.

The samples are compressed with the punch velocity of 0.01 *mm/s* to the height reduction of 75%. In order to verify the applicability of the proposed model, the micro-scaled flanged upsetting is chosen as the microforming method. The height and diameter ratio *H/D* of 1.5 is selected for the flanged upsetting, as shown in Fig. 4.3.

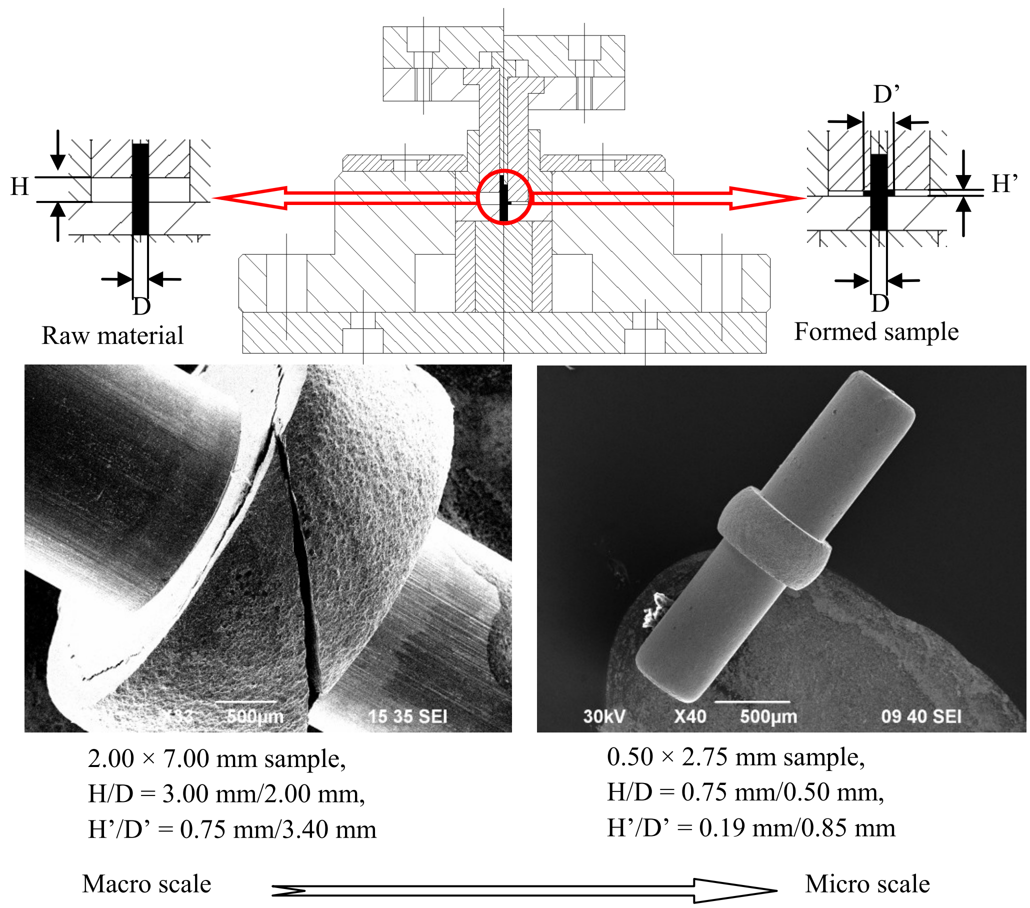

Fig. 4.3. Micro-scaled flanged upsetting.

Other verification experiments are also conducted to prove the influence of size effect in micro-scaled compression-dominative plastic deformation. In Fig. 4.4, three types of upsetting process are conducted in both macro and micro scale. The dimension of the specimens in these upsetting processes has been scaled down from 2×3 *mm* to 0.5×0.75 *mm*. The specimen shapes of these three upsetting process are different in order to distinguish the stress contribution of the removed material of cylinder shape specimen. The specimens have been compressed to 25% of their original height and observed by using SEM, as shown in Fig. 4.5. For the as-received samples, it is discovered that major cracks exist in all three types of specimens in Scenario 1, while no major cracks exist in all three types of specimen in Scenario 3 and 4. For the samples annealed at $800^{\circ}C$, major crack only exists in Type B of Scenario 1. This is a proof of the existence of feature size effect in microforming.

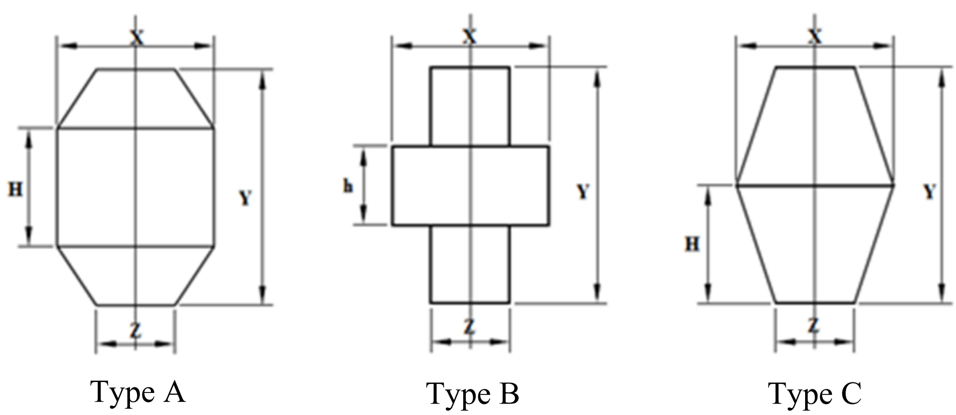

	Scenario 1	Scenario 2	Scenario 3	Scenario 4
X (*mm*)	2	1	0.5	0.25
Y (*mm*)	3	1.5	0.75	0.375
Z (*mm*)	1	0.5	0.25	0.125
H (*mm*)	1.5	0.75	0.375	0.1875
h (*mm*)	1	0.5	0.25	0.125

Fig. 4.4. Three types of billets for verification upsetting experiments.

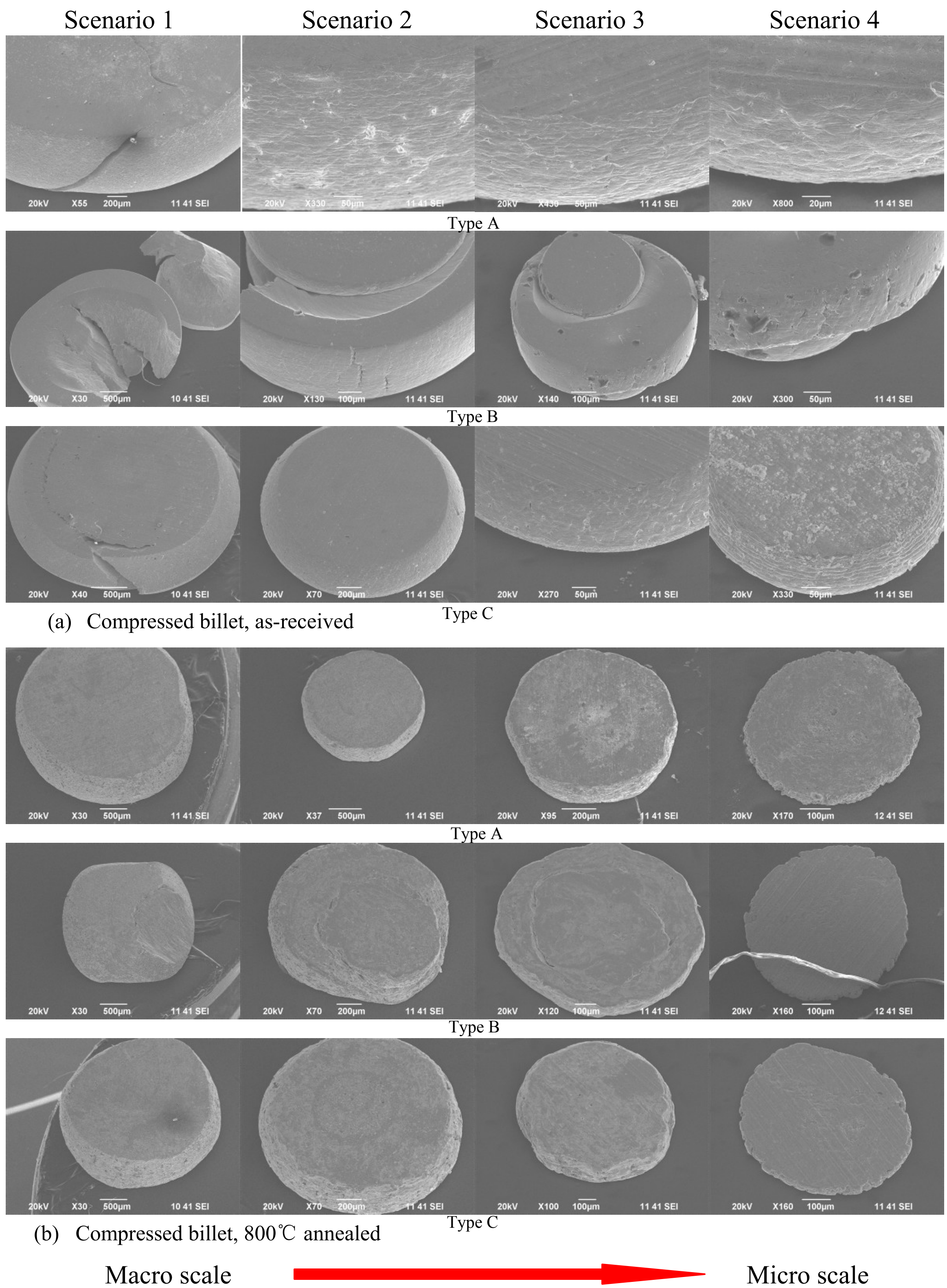

Fig. 4.5. SEM photos of verification upsetting experiments.

4.5 Implementation and result discussion

4.5.1 Coefficient calibration procedure of the hybrid constitutive model

Eq. (4.14) is the final format of the hybrid constitutive model. The unknown coefficients of the equation are determined by curve fitting method based on the flow stress data of the macro-scaled upsetting experiment. How the experimental data is used for coefficient calibration is presented in Table 4.1. The stress-strain curve of the sample with the dimension of $2\times3mm$ is used for curve fitting, while the experimental data of the samples with other three dimensions is used for result comparison with simulation.

Table 4.1. Experimental data processing.

Heat treatment / Size	As received	450°C annealed	600°C annealed	750°C annealed
2×3mm	Macro-scaled experimental result, used for curve fitting			
1×1.5mm	Micro-scaled experimental result, used for result comparison			
0.5×0.75mm	Micro-scaled experimental result, used for result comparison			
0.25×0.375mm	Micro-scaled experimental result, used for result comparison			

Eq. (4.14) is applicable for all scenarios as it is suitable for both the fine and coarse grains. The equation contains five unknown coefficients, viz., k_2, n_2, C_1, C_2 and

C_3. Fig. 4.6 presents the curve fitting procedure used to determine the five unknown coefficients in this research. In the figure, the coefficients marked with red color are unknown and to be decided in the shown curve fitting stage, while the volume fraction of alpha phase f_α, grain size d and size factor λ can be determined using the experimental result before the curve fitting.

There are three curve fitting stages as shown in Fig. 4.6. The first curve fitting uses the flow stress data of the as-received specimen with the dimension of $2\times3mm$. The size factor λ of this scenario, which is calculated from the information of metallographic photo, is 4% and its size effect is ignored. Thus, only the independent part of Eq. (4.13) needs to be considered. With the flow stress data of the as-received specimens and those annealed at $450^\circ C$ with the dimension of $2\times3mm$, the unknown coefficients k_2, n_2, C_1 and C_2 of Eq. (4.13), are calculated and determined by using curve fitting method, which is only suitable for the deformation of specimen with fine grains.

The second curve fitting uses the flow stress data of the specimen annealed at $450^\circ C$ with the dimension of $2\times3mm$. The coefficients k_2, n_2, C_1 and C_2 are recalculated and adjusted to ensure the hybrid model fits both the experimental results of the as-received scenarios and those annealed at $450^\circ C$.

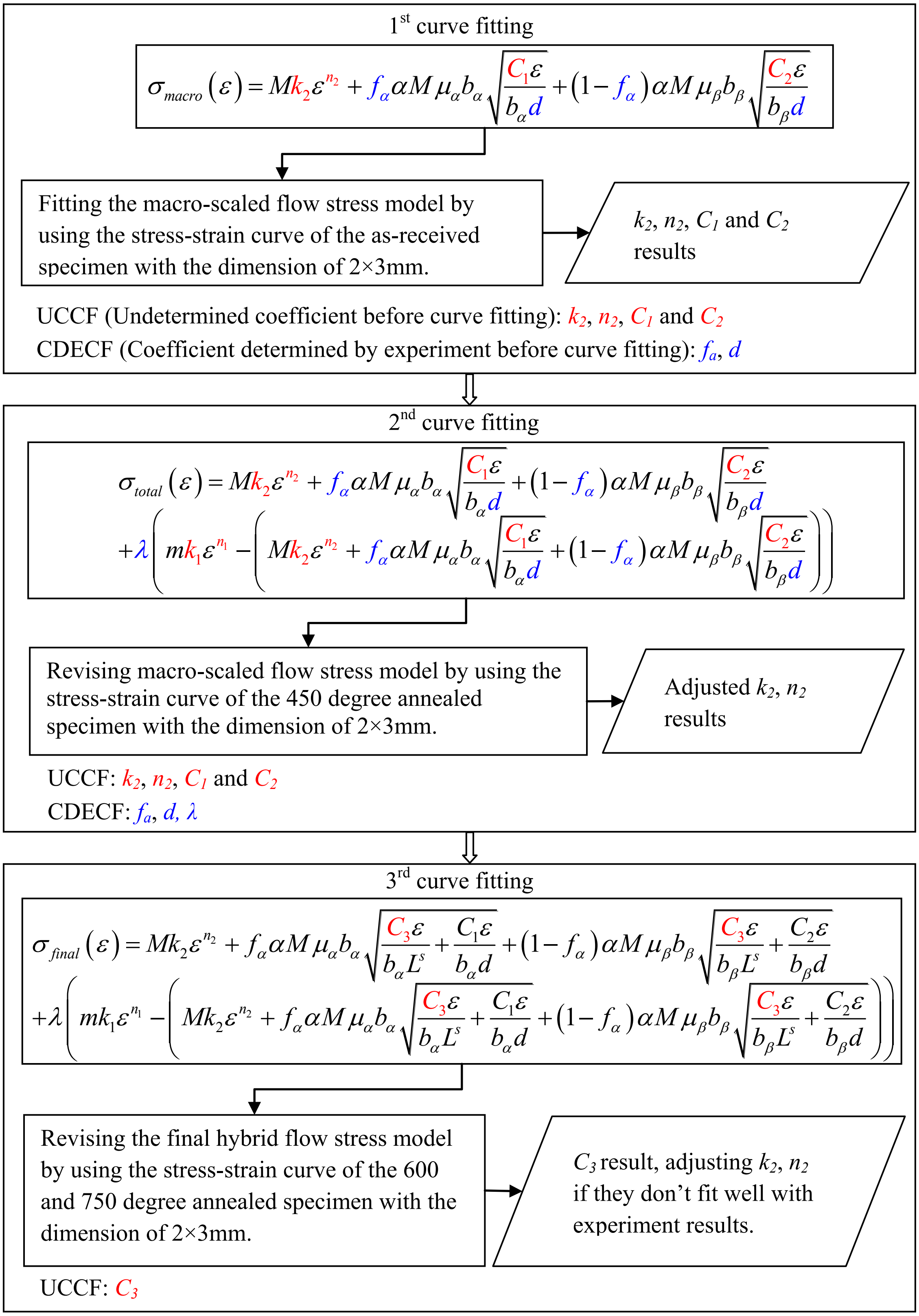

Fig. 4.6. Curve fitting procedure.

After the two rounds of curve fitting, the remaining unknown coefficient C_3 can be determined via curve fitting of the flow stress data of the specimens annealed at 600 and $750^{\circ}C$ with the dimension of $2\times3mm$. A slight adjustment of the coefficients k_2, n_2, C_1 and C_2 is necessary if the fitted curve has a significant difference from any experimental result of the four scenarios with the sample dimension of $2\times3mm$.

4.5.2 Coefficients calculation of micro-scaled deformation

According to Eq. (4.10), the macro-scaled stress obtained from the simple upsetting experiment can be decomposed into the stresses of various phases. As there is only 2% lead in Brass C3602, the deformation body can be specified into α and β phases without consideration of the stress influence of lead phase.

In Fig. 4.7, there are about 5% of the total pixels of EDX picture with black color. It indicates that there is no spectrum to be detected. By sharpening the metallurgical photo as shown in Fig. 4.8, it shows that the volume fraction of the white area is 77%, representing α phase, while the black area is about 22%, representing β and lead phases. This result is closed to the EDX result and the final volume fractions of α, β and lead phases are 81, 17 and 2%, respectively.

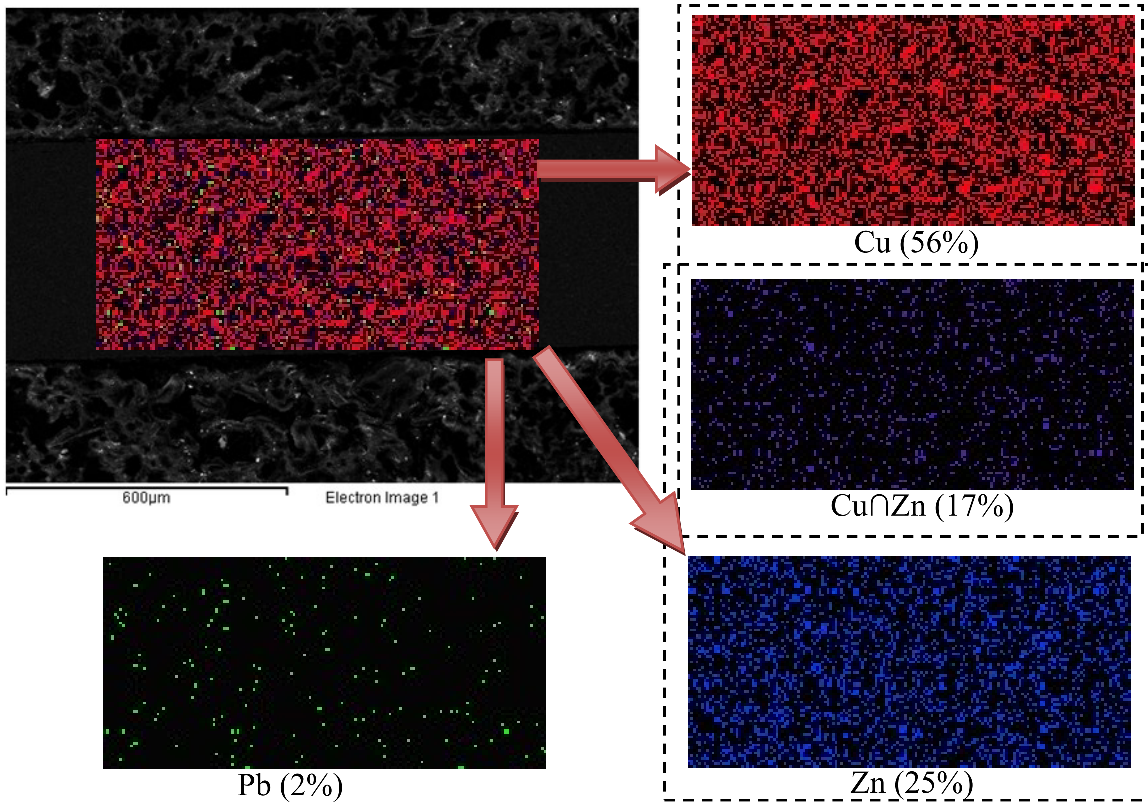

Fig. 4.7. Determination of the phase volume fraction by EDX.

In Eq. (4.13), $\alpha = 0.34$ (Rodriguez, 2003); $\mu_\alpha = 78500$ MPa (shear modulus for FCC phase); $\mu_\beta = 72000$ MPa (shear modulus for BCC phase); $b_\alpha = \frac{\sqrt{2}}{2} \times 3.69 \times 10^{-10} = 2.608 \times 10^{-10} m$ (Burgers vector for FCC phase); $b_\beta = \frac{\sqrt{3}}{2} \times 2.94 \times 10^{-10} = 2.546 \times 10^{-10} m$ (Burgers vector for BCC phase); the volume fraction of each phase is obtained based on the EDX results, which is 83% for α phase and 17% for β phase. The unknown coefficients in Eq. (4.13) are the constants of dislocation density in α and β phases. By using the curve fitting approach, the constants C_1 and C_2 can be determined and Eq. (4.13) thus becomes:

$$\sigma_{total}(\varepsilon) = 587.52\varepsilon^{0.23} + 0.498\varepsilon^{0.5} \cdot d^{-\frac{1}{2}} - \lambda\left(203.52\varepsilon^{0.23} + 0.498\varepsilon^{0.5} \cdot d^{-\frac{1}{2}}\right) \tag{4.15}$$

where $C_1 = 0.14$, $C_2 = 0.18$, $k_1 = k_2 = 192$, $n_1 = n_2 = 0.23$, $M = 3.06$, $m = 2$. k_1 and k_2, n_1 and n_2 here are actually the same coefficients in the equation of $\tau_0(\varepsilon) = k\varepsilon^n$. The subscript is used to distinguish the stress of surface grain in Eq. (4.12).

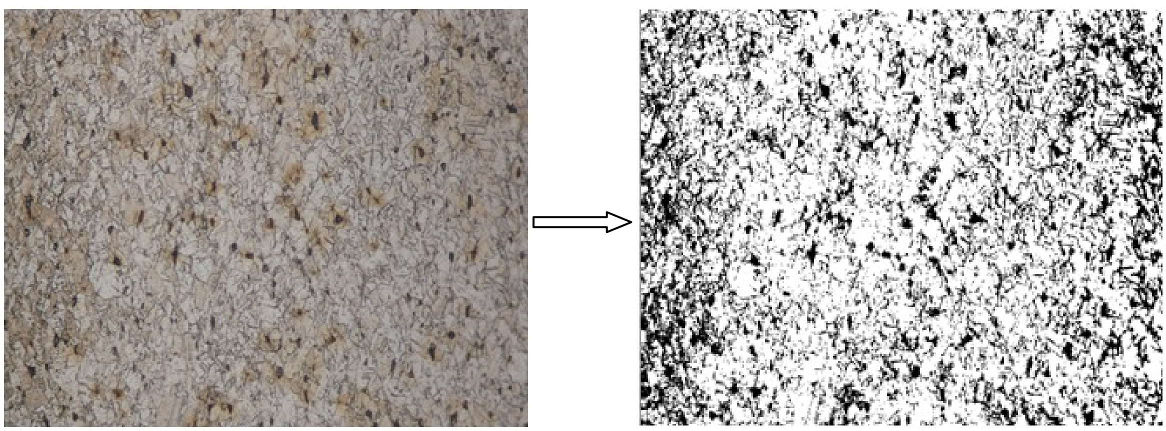

Microstructure of Brass C3602

The sharpened metallurgical photo for phase distinguishing

Fig. 4.8. Determination of the phase volume fraction via metallurgical photo.

The comparison between the calculation result and the true stress-strain curve from the actual experiment is shown in Figs. 4.9 and 4.10. In Fig. 4.9 (a), the solid curve without star is the true stress-strain curve obtained from the actual experiment and the curve with star is the curve fitting result of macro-scaled simple upsetting. By using the data in Eq. (4.15), the unknown coefficient in Eq. (4.14) can be determined.

The final description of flow stress and size factor η is obtained and presented in Eq. (4.16)

$$\sigma_{total}\left(\varepsilon\right)=587.52\varepsilon^{0.23}+0.681\varepsilon^{0.5}\cdot d^{-\frac{1}{2}}-\lambda\left(203.52\varepsilon^{0.23}+0.681\varepsilon^{0.5}\cdot d^{-\frac{1}{2}}\right) \tag{4.16}$$

Fig. 4.10 shows the simulation result of the flow stress model using Eq. (4.16). It indicates that when the size factor λ is higher, the simulation result is closer to the actual experimental result.

Although Figs. 4.9 and 4.10 show a good variation trend between the simulation results and the experimental ones, some part of the simulated stress curve has deviation with the experimental results. This is caused by the fact that the unknown coefficients of Eq. (4.14) are calibrated with the flow stress data of all the four scenarios with the sample dimension of $2\times3mm$. If the four unknown coefficients k_2, n_2, C_1 and C_2 are determined without adjustment after the first curve fitting, the simulation result of the as received scenario is quite close to the experimental results. However, the simulation results of other three scenarios, including 450, 600 and $750^{\circ}C$ annealed series, all deviate from the actual experimental results. Thus, the coefficients k_2 and n_2 need to be calibrated and adjusted after the two rounds of curve fitting to ensure all the simulation results are as close as possible to the corresponding experimental results.

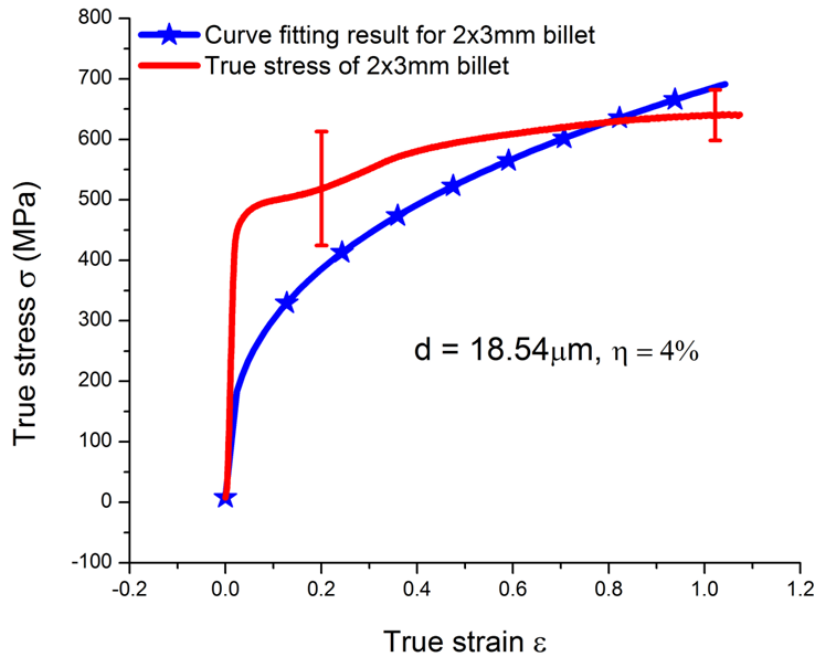

(a) 2 ×3 mm billet, As-received.

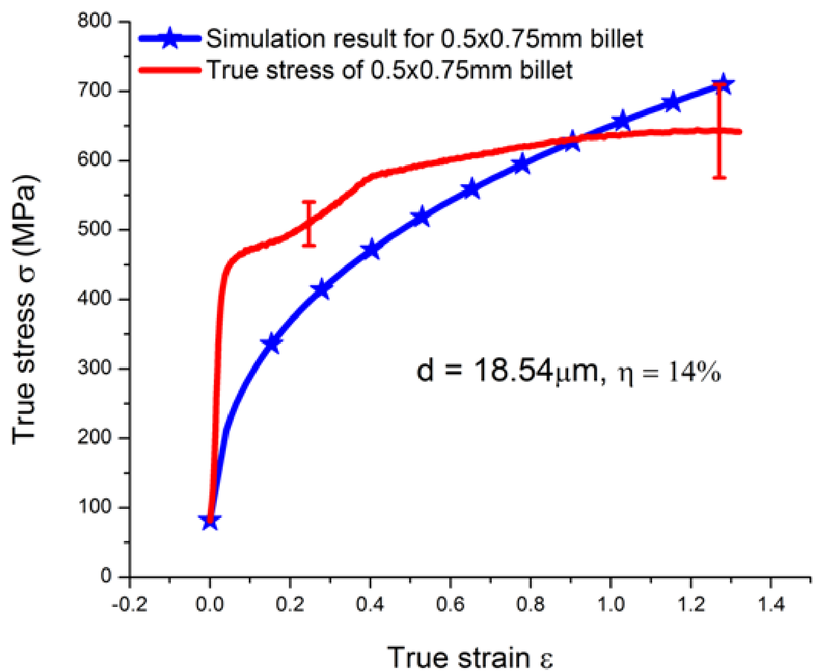

(b) 0.5 ×0.75 mm billet, As-received.

Fig. 4.9. Comparison of the curve fitting and the experimental results (As-received sample).

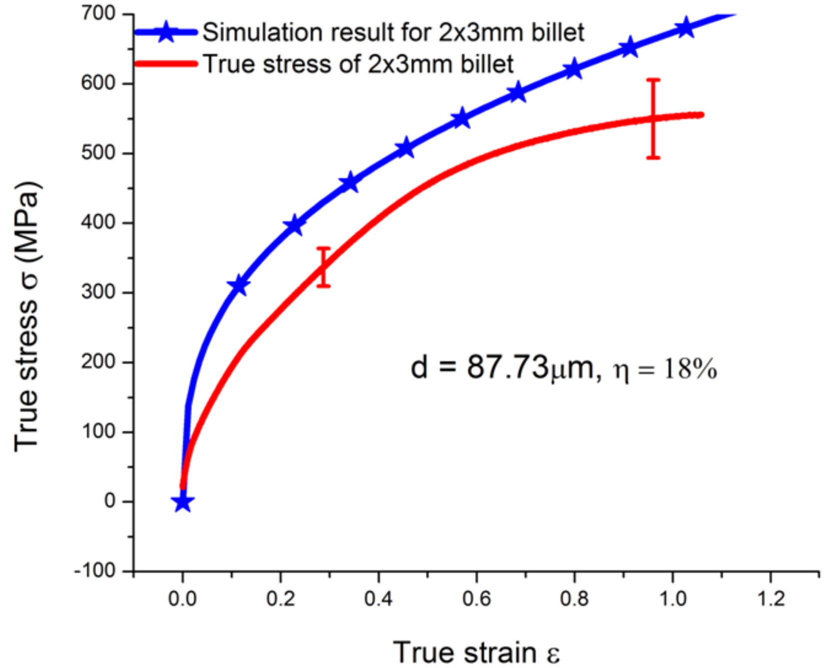

(a) 2 × 3 mm billet, 750°C annealed.

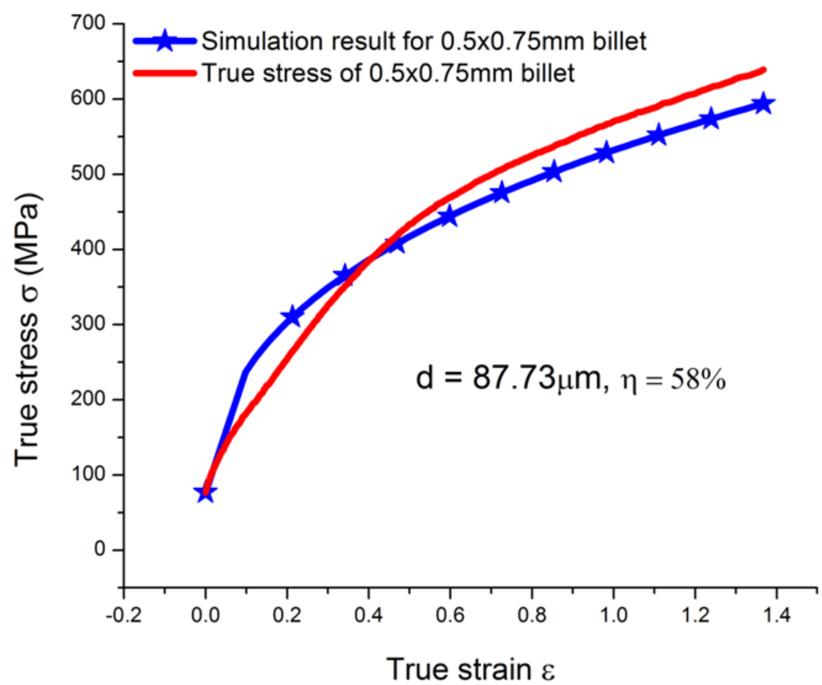

(b) 0.5 × 0.75 mm billet, 750°C annealed.

Fig. 4.10. Comparison of the simulation and experimental results (750°C annealed).

When the experimental data of macro-scaled upsetting is used, the unknown coefficients of Eqs. (4.13) and (4.14) can be calculated via curve fitting and Eqs. (4.15) and (4.16) are thus obtained. Eq. (4.15) is suitable for macro- and micro-scaled deformation when there are few coarse grains in the specimen, while Eq. (4.16) is applicable for macro- and micro-scaled deformation of all kinds of scenarios. Therefore, the stress-strain curve of micro-scaled upsetting process can be calculated via Eqs. (4.15) and (4.16) and compared with the experimental result.

4.6 Ductile fracture prediction

In order to predict the ductile fracture, the fracture energy of the deformation material, which is considered as a material-related constant, must first be determined. Based on Freudenthal's criterion [42], the damage evolution equation can be expressed in the following form:

$$C = \int_0^{\varepsilon_f} \sigma(\varepsilon) d\varepsilon \tag{4.17}$$

To use the fracture energy C to predict the ductile fracture, the size effect needs to be considered. By combining Eqs. (4.15) and (4.17), the fracture energy C is presented as follows:

$$C = \int_0^{\varepsilon_f} \left(587.52\varepsilon^{0.23} + 0.681\varepsilon^{0.5} \cdot d^{-\frac{1}{2}} - \lambda \left(203.52\varepsilon^{0.23} + 0.681\varepsilon^{0.5} \cdot d^{-\frac{1}{2}} \right) \right) d\varepsilon \tag{4.18}$$

Using the original $2 \times 3mm$ billet without heat treatment, the fracture strain of $\varepsilon = 1.15$ is obtained. With the corresponding grain size $d = 18.54\mu m$ and the size factor $\lambda = 0.04$, the C value can thus be determined as:

$$C = \int_0^{1.15} \left(587.52\varepsilon^{0.23} + 0.681 \times \varepsilon^{0.5} \times \left(18.54 \times 10^{-6}\right)^{-\frac{1}{2}} \right. \\ \left. -0.04 \times \left(203.52\varepsilon^{0.23} + 0.681 \times \varepsilon^{0.5} \times \left(18.54 \times 10^{-6}\right)^{-\frac{1}{2}} \right) \right) d\varepsilon = 684.09 \tag{4.19}$$

With the hybrid fracture model shown in Eq. (4.18) and the fracture energy C, the fracture strain and grain size of other scenarios can thus be calculated. In Fig. 4.11, the dash line represents the corresponding expected fracture strains of different scenarios, which are $\varepsilon_{0.5\times0.75,AS} = 1.19$, $\varepsilon_{2\times3,750^\circ C} = 1.19$ and $\varepsilon_{0.5\times0.75,750^\circ C} = 1.39$. These results are quite close to the actual experimental results.

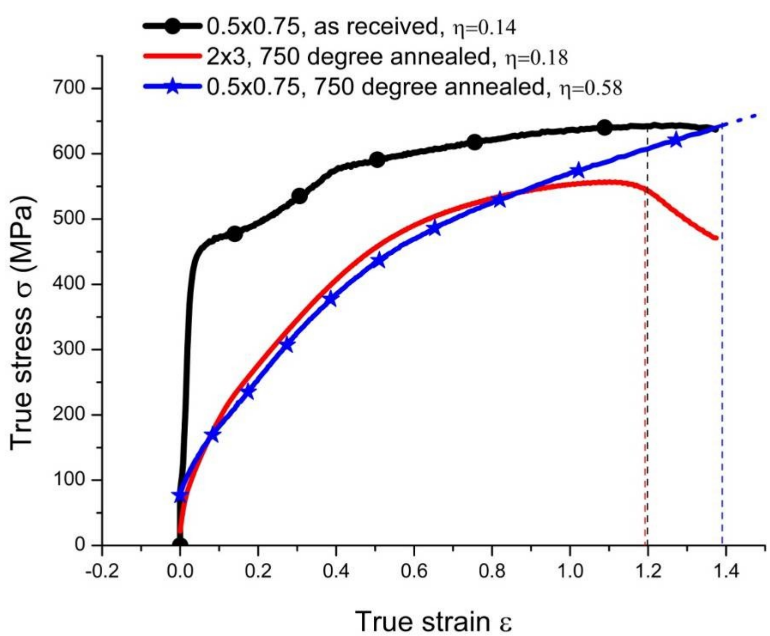

Fig. 4.11. Fracture strain prediction for different size factors.

4.7 Numerical implementation

In this chapter, the finite element simulation was conducted in ABAQUS, which has powerful nonlinear analysis function. In addition, the 4-node bilinear element CAX4R mesh is employed as it is suitable for processing of large plastic deformation. The total number of elements is 1794 and the total number of nodes is 1946. By setting the damage evolution condition with the calculated expected fracture strain in Table 4.2, the mesh elements, which are damaged and considered as invalid mesh elements, will be deleted automatically.

Table 4.2. The expected fracture strain and size factor of Brass C3602.

C \ Size	2×3mm	1×1.5mm	0.5×0.75mm	0.25×0.375mm
684 (As received)	$\varepsilon_f = 1.15$, $\lambda = 4\%$	$\varepsilon_f = 1.16$, $\lambda = 7\%$	$\varepsilon_f = 1.19$, $\lambda = 14\%$	$\varepsilon_f = 1.26$, $\lambda = 27\%$
578 ($450^{\circ}C$ annealed)	$\varepsilon_f = 1.03$, $\lambda = 5\%$	$\varepsilon_f = 1.05$, $\lambda = 9\%$	$\varepsilon_f = 1.08$, $\lambda = 18\%$	$\varepsilon_f = 1.16$, $\lambda = 35\%$
598 ($600^{\circ}C$ annealed)	$\varepsilon_f = 1.11$, $\lambda = 9\%$	$\varepsilon_f = 1.15$, $\lambda = 18\%$	$\varepsilon_f = 1.22$, $\lambda = 33\%$	$\varepsilon_f = 1.36$, $\lambda = 59\%$
606 ($750^{\circ}C$ annealed)	$\varepsilon_f = 1.19$, $\lambda = 18\%$	$\varepsilon_f = 1.25$, $\lambda = 32\%$	$\varepsilon_f = 1.39$, $\lambda = 58\%$	$\varepsilon_f = 1.63$, $\lambda = 91\%$

As mentioned in Section 4.2, Eq. (4.16) is the final format of the hybrid constitutive model. Eq. (4.16) can be used not only to calculate the expected fracture strain of specimens annealed at 450, 600 and $750^{\circ}C$, but also provides the expected flow stress data of the upsetting deformation of these scenarios when the size factor is determined via the metallographic photo. When a series of strains are provided, the expected flow stress of each scenario can be obtained from Eq. (4.16). These expected flow stress curves are then implemented into ABAQUS to simulate the micro-scaled flanged upsetting process. Fig. 4.12 shows the simulation result of the deformation load in micro-scaled flanged upsetting by using multiphase hybrid model and it indicates that the load predicted by simulation is close to the actual experimental result. In addition, there is no ductile fracture occurrence in this deformation scenario. In this figure, it is obvious that the stress-strain curve obtained from experiment is smoother than the one from simulation. This is because the load amplitude type used in this simulation is “tabular”. It will cause “force vibration” in the force-time curve which is obtained via ABAQUS. Changing the amplitude type to “smooth” or increase the simulation time and mesh number is an acceptable option in simulation, but these measures will significantly increase the simulation time. Since the simulation result and experimental result have an agreement, the measures above will not be changed in this research in consideration of the simulation efficiency.

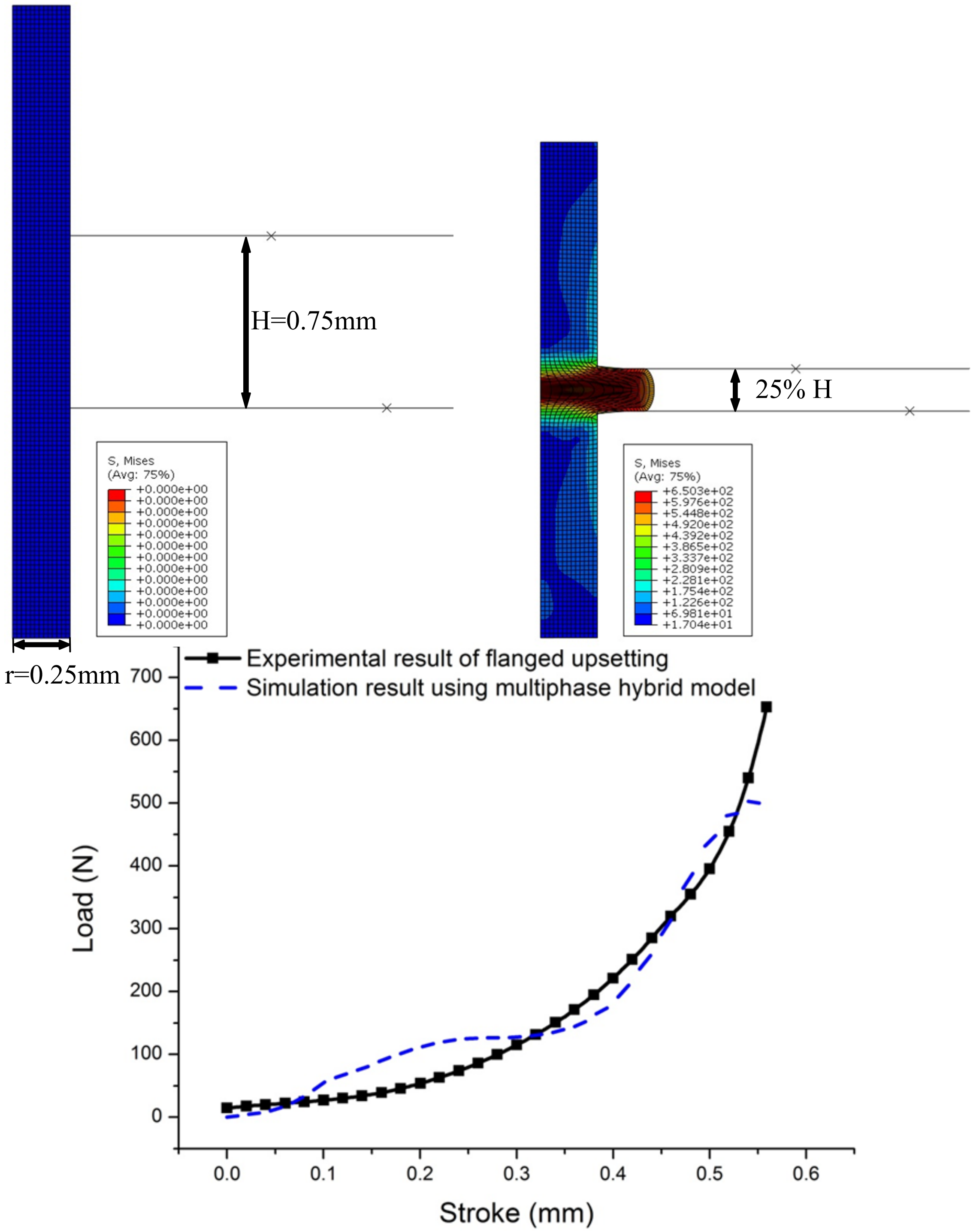

Fig. 4.12. The expected and the actual load-stroke curves in micro-flanged upsetting.

4.8 Stress-induced fracture map

The FE simulation of micro-scaled flanged upsetting can be implemented after the *C* value and the fracture strain are determined. Table 4.2 shows the expected fracture strain and the size factor for each case. In the table, the fracture energy *C* for each scenario of the material with different heat treatment conditions is calculated from Eq. (4.19). The size factor λ is determined based on Eq. (4.11). The expected fracture strain is calculated from Eq. (4.18) when the fracture energy *C* is confirmed via Eq. (4.18) for each scenario.

Upon acquisition of the data from simulation, the stress-induced fracture map (SFM) for multiphase alloys is proposed. In Fig. 4.13, all the expected fracture strains calculated by the hybrid ductile fracture model are presented in the map. For the multiphase alloys such as C3602, the SFM is established by using the data shown in Table 4.2. In SFM, each axis stands for specimen size, fracture energy and the expected fracture strain of the material. As the grain size effect occurs when the grain size is changed while the specimen size remains constant, the fracture energy *C* represents this type of size effect as *C* is a material constant for the material with the same microstructure. For feature size effect, the dimension of the specimen represents the influence of feature size change. Therefore, the SFM demonstrates the influence of grain and feature size effects in micro-scaled ductile fracture deformation.

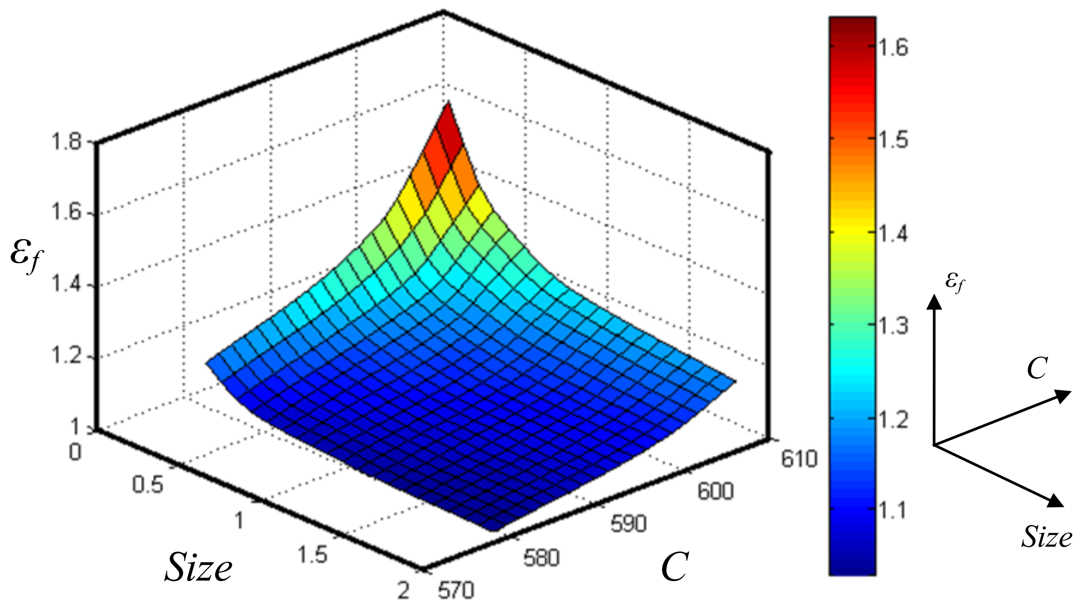

Fig. 4.13. Stress-induced fracture map.

By using the data in Table 4.2, a pre-stress-induced fracture map is first established. From Fig. 4.14, it is clear that the original material without heat treatment has the highest fracture energy ($C_{As\ Received} = 650^{\circ}C$), but its fracture strain is considered to be lower than that of the material annealed at $750^{\circ}C$. This indicates that the "original samples" may have received other types of heat treatment. The final of SFM can be constructed after the "as-received" series is removed, which is shown in Fig. 4.15.

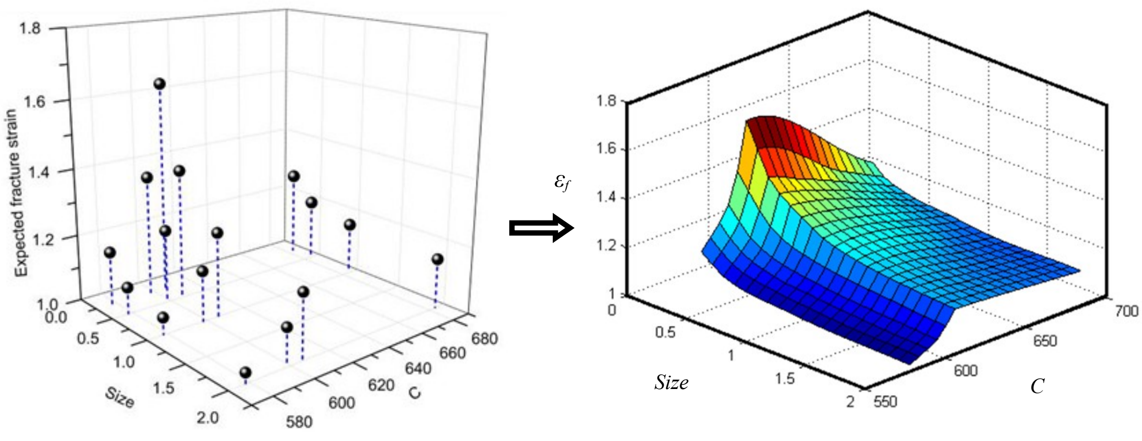

Fig. 4.14. Pre-stress-induced fracture map of Brass C3602.

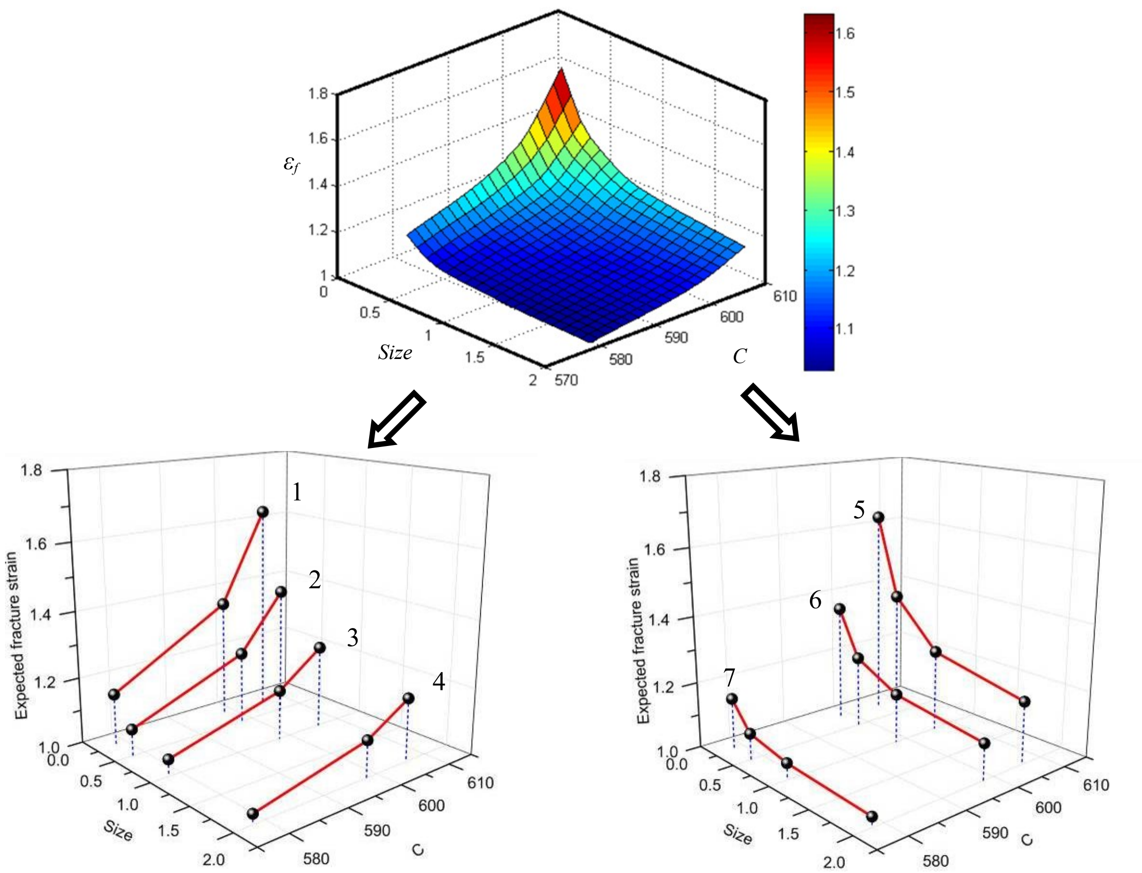

(a) Grain size effect

(b) Feature size effect

Fig. 4.15. Change of the fracture strain in different types of size effects.

When SFM is completed, each scenario in the range of size and fracture energy can have a unique fracture strain from SFM. This fracture strain is a damage initiation condition for the ideally isotropic metal alloys. Analysis of these scenarios is thus conducted in the following:

(1) The change of the expected fracture strain with the two size effects is different for each scenario. For grain size effect, the change of fracture strain in each size scale can be considered as the same. From Fig. 4.15 (a), lines 1, 2, 3 and 4, which indicate the tendency mentioned above, are considered as linear curve. On the other hand, the fracture strain change affected by feature size effect in Fig. 4.15 (b) is not the same in each scenario. When the annealing temperature is high such as $600^{\circ}C$ and $750^{\circ}C$, the gradient of these curves increases rapidly when the specimen diameter is smaller than 0.5 *mm*.

(2) For the two types of size effects, grain size effect has greater influence on fracture strain than feature size effect when the size factor λ is the same. As shown in Fig. 4.16, the scenarios which are linked by lines have the same size factor. It is found that the expected fracture strain affected by grain size effect is larger than those affected by feature size effect when the size factor is the same. This phenomenon can be explained based on Eq. (4.20) in the following:

$$C = 77.1\varepsilon_f^{1.5} + 477.7\varepsilon_f^{1.23} - \lambda \cdot \left(77.1\varepsilon_f^{1.5} + 165.5\varepsilon_f^{1.23}\right) \tag{4.20}$$

Eq. (4.20) is the solution of Eq. (4.18). For feature size effect, the fracture energy C remains the same for each scenario as feature size effect does not change the grain size or fracture energy. When the size factor λ increases, the expected fracture strain must increase to maintain the same *C*. For the grain size effect, the fracture energy *C* also increases with size factor λ. Therefore, the expected fracture strain needs to increase much more than that in the feature size effect scenario.

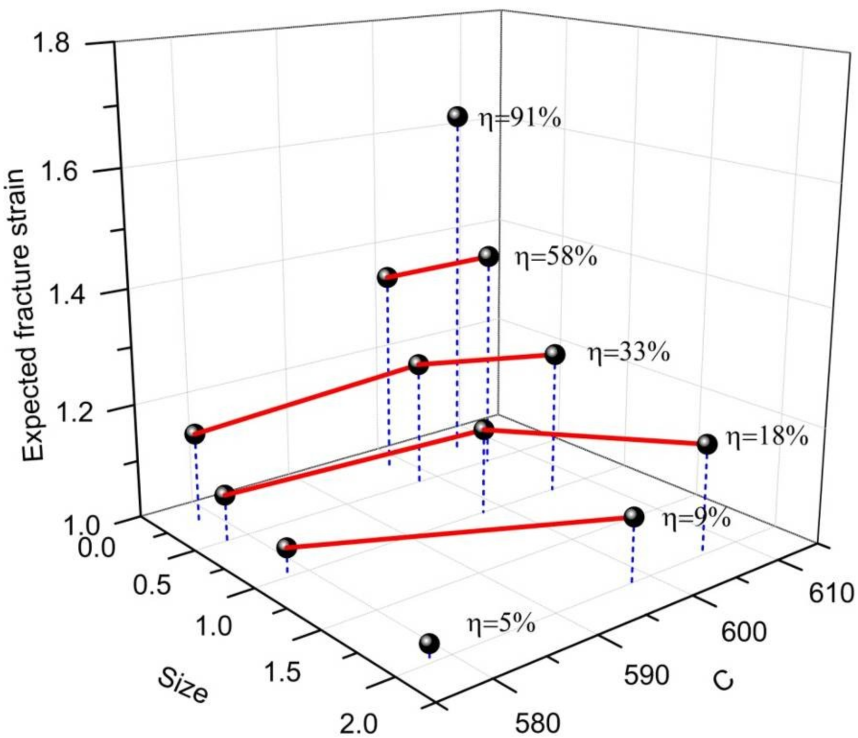

Fig. 4.16. The expected fracture strain with the same size factor λ.

The SFM not only predicts the fracture strain of certain multiphase alloy, but also reveals the in-depth relationship of grain size effect and feature size effect in ductile fracture of microforming. It can be considered as a useful tool in predicting the stress-induced fracture in microforming process.

Fig. 4.17 demonstrates the simulation results and the actual experimental result via SFM. In this figure, the surface marked with stars represents the real fracture map with the actual experimental result. This real fracture map is drawn after all the actual fracture strains of different scenarios in Table 4.2 are obtained. Compared with the simulation result, it is obvious that there is an agreement between this new model and the experimental result. When the deformation is large, the result of the new model is much closer to the experimental results.

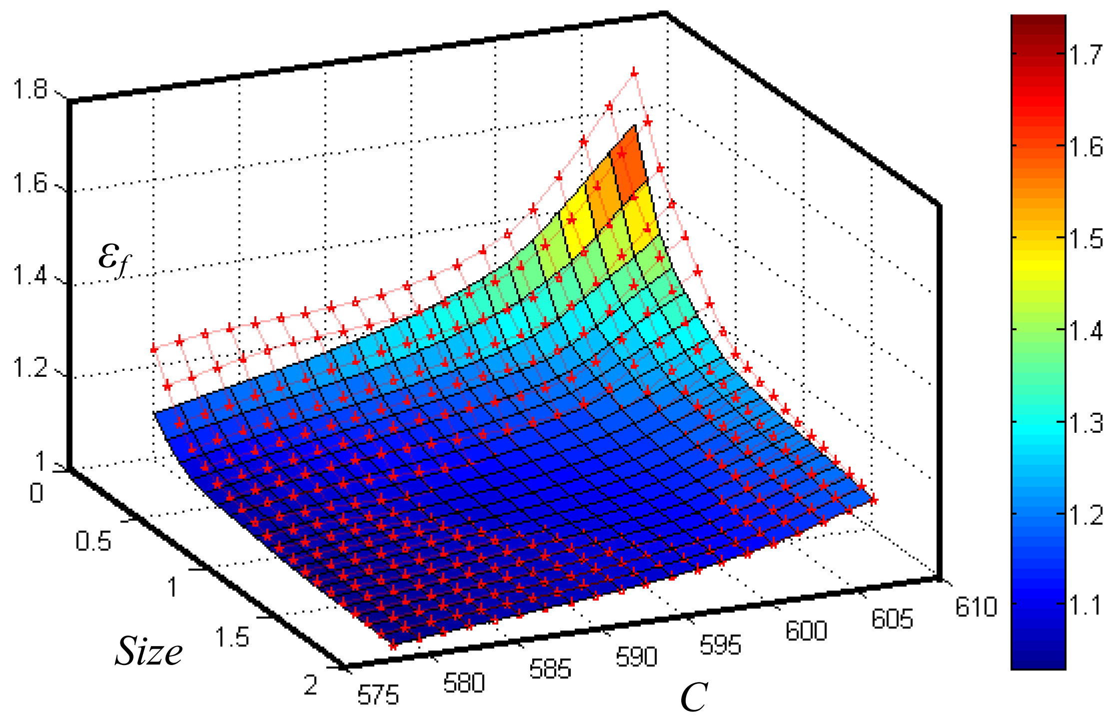

Fig. 4.17. Comparison of the simulation and the actual experimental results.

4.9 Summary

A hybrid flow stress model for multiphase alloys, which determines the contribution of each phase to the mechanical deformation behavior of material and uses fracture energy to predict the ductile fracture in microforming, is proposed. The fracture energy of the testing material brass C3602 is calculated and the fracture strain of each scenario is obtained for fracture prediction. As the simulation results based on the proposed hybrid model have a good agreement with the actual experimental ones, the proposed model is thus considered to be more reliable in ductile fracture prediction. In this chapter, the following concluding remarks can be drawn:

1. It is found that the dislocation density and phase volume fraction affect the flow stress of materials in micro-scaled deformation process and the proposed multiphase hybrid model can effectively describe this effect.
2. By using the macro-scaled upsetting flow stress data, the coefficients of the hybrid model can be determined and the expected fracture strain and flow stress of the materials with different geometry sizes can be obtained directly and used for flow-induced fracture prediction.
3. The stress-induced fracture map is constructed for predicting the fracture strain of multiphase alloys and revealing the in-depth relationship of grain size effect and geometry size effect in micro-scaled ductile fracture deformation. It thus provides a useful tool for prediction of ductile fracture in micro-scaled plastic deformation.
4. For micro-scaled bulk material forming process, the grain size effect has greater influence on the stress-induced fracture formation than the feature size effect.

When the size factor of the two size effects is the same, the fracture strain of the grain size effect is considered higher than the one of feature size effect.

Chapter 5 Applicability of Fracture Criteria in Microforming

5.1 Introduction

As mentioned in prior chapters, most of the previous fracture researches are focused on macroforming, in-depth research on the fracture behavior in micro-scaled plastic deformation has not yet been extensively conducted [22-26,43-51]. The essential issues of ductile fracture and the applicability of ductile fracture criteria (DFC) in microforming are thus needed to be systematically studied.

This chapter investigates the applicability of six uncoupled fracture criteria which are widely used in macro-scaled forming processes. To explain their applicability in micro-scaled deformation, the hybrid constitutive model developed in chapter 4 is used in FE simulation and the six DFCs are implemented [3,4]. The critical value of each DFC is calculated by using the hybrid constitutive model. To describe the flow stress change in micro-scaled plastic deformation, the size factor is determined and included in the hybrid constitutive model. The influence of size effect on fracture behavior is quantified by SFM. Finally, the applicability of the six DFCs are identified by comparing the FE simulation results with the experimental results including load-stroke curve and the SFM.

5.2 The uncoupled ductile fracture criteria

Table 5.1 lists six widely used uncoupled DFCs. Each DFC has its own critical value, and fracture occurs when the integral value is larger than its critical value.

Table 5.1. Uncoupled fracture criteria.

Macro scale fracture criteria	Criteria formula	Criteria description
Cockcroft and Latham model	$\int_0^{\varepsilon_f} \bar{\sigma}\left(\frac{\sigma^*}{\bar{\sigma}}\right) d\bar{\varepsilon} = \int_0^{\varepsilon_f} \sigma^* d\varepsilon = C$	Cockcroft-model-based criterion
Oyane model	$\int \left(\frac{1}{\alpha_0}\frac{\sigma_m}{\bar{\sigma}} + 1\right) d\bar{\varepsilon} = C$	Cockcroft-model-based criterion
Ayada model	$\int_0^{\bar{\varepsilon}_f} \left(\frac{\sigma_m}{\bar{\sigma}}\right) d\bar{\varepsilon} = C$	Cockcroft-model-based criterion
Brozzo model	$\int_0^{\bar{\varepsilon}_f} \frac{2\sigma^*}{3\left(\sigma^* - \sigma_m\right)} d\bar{\varepsilon} = C$	Cockcroft-model-based criterion
Johnson-Cook model	$\varepsilon_f = A_1 + A_2 e^{A_3 \frac{\sigma_m}{\bar{\sigma}}}$	Stress-triaxiality-based criterion
Rice and Tracey model	$\int_0^{\varepsilon_f} e^{\alpha \frac{\sigma_m}{\bar{\sigma}}} = C$	Stress-triaxiality-based criterion
Freudenthal model	$\int_0^{\bar{\varepsilon}_f} \bar{\sigma} d\bar{\varepsilon} = C$	Energy-based criterion

Eq. (1.1) is the representation of the uncouple DFCs. The critical value C is material constant and usually determined by upsetting and tensile tests. For the material with a specific heat treatment condition, its unique C value can be obtained.

Among the six DFCs, Cockcroft and Latham criterion is one of the pioneer criteria in ductile fracture arena, which is proposed based on Freudenthal criterion [36]. It is found that the yield stress at fracture point is not affected by the shape of the necked region in tensile test, which is different from the actual experiment scenario. The Cockcroft criterion is thus developed for bulk forming and applicable to the deformation with low stress triaxility. The simplified form of the criterion is designated as:

$$\int_0^{\bar{\varepsilon}_f} \bar{\sigma} \cdot \frac{\sigma_1}{\bar{\sigma}} d\varepsilon = \int_0^{\bar{\varepsilon}_f} \sigma_1 d\varepsilon = C \tag{5.1}$$

In Eq. (5.1), σ_1 is the maximum principal stress and $\left(\frac{\sigma_1}{\bar{\sigma}}\right)$ is a non-dimensional stress-concentration factor.

Oyane model articulates the concept of ductile fracture with four development stages, viz., micro-scaled void formation caused by dislocation pile-up, void distance becoming closer due to void growth, plastic deformation concentration, and the dimple initiation on the surfaces of material [52]. For porous materials, by employing the relationship between equivalent strain $\bar{\varepsilon}$ and volumetric strain ε_v, the stress strain relationship can be represented by Eq. (5.2) in the following.

$$d\varepsilon_v = \frac{d\bar{\varepsilon}}{\gamma f^2}\left(\frac{\sigma_m}{\bar{\sigma}} + \alpha_0\right) \tag{5.2}$$

where γ is the ratio between the nominal density and the constituent metal density of porous material and f is a function of γ. σ_m is the hydrostatic stress and α_0 is a material constant. The volumetric strain ε_v represents the volume alternation of porous materials and can be represented as the ratio between the volume of the porous material and the volume of the constituent metal with the same weight and denoted as:

$$\varepsilon_v = In\frac{v}{v_0} = -In\frac{\rho}{\rho_0} = -In\gamma \tag{5.3}$$

In Eq. (5.2), the fracture strain can be determined if the fracture occurs at a particular volumetric strain. Eq. (5.2) can be further formulated in the form below:

$$\int \frac{\gamma f^2}{\alpha_0} d\varepsilon_v = \int \left(\frac{1}{\alpha_0} \cdot \frac{\sigma_m}{\bar{\sigma}} + 1 \right) d\bar{\varepsilon} \tag{5.4}$$

As α_0, γ and f are all material constant, Eq. (5.4) can be written as:

$$\int_0^{\bar{\varepsilon}_f} \left(\frac{1}{\alpha_0} \cdot \frac{\sigma_m}{\bar{\sigma}} + 1 \right) d\bar{\varepsilon} = C \tag{5.5}$$

where *C* is the critical value of this criterion.

Ayada criterion is proposed based on Cockcroft and Oyane criteria to provide an evaluation of fracture in compression-dominative deformation, since the result predicted by Cockcroft criterion is beyond satisfactory when the strain is large and the tensile stress is small [53]. The form of Ayada criterion is shown in Eq. (5.6).

$$\int_0^{\bar{\varepsilon}_f} \left(\frac{\sigma_m}{\bar{\sigma}} \right) d\bar{\varepsilon} = C \tag{5.6}$$

where σ_m is the mean stress. *C* is the critical value of this criterion and considered to be inversely proportional to the hardness of material according to experiment.

Brozzo criterion in Eq. (5.7) is established on the basis of Cockcroft criterion and articulates the relationship between the maximum stress and mean stress at fracture [54].

$$\int_0^{\bar{\varepsilon}_f} \bar{\sigma} d\bar{\varepsilon} = const = a \int_0^{\bar{\varepsilon}_f} \bar{\varepsilon}^n d\bar{\varepsilon} = \frac{a}{n+1} \bar{\varepsilon}_f^{n+1} \tag{5.7}$$

By introducing the stress concentration factor $\frac{\sigma_1}{\bar{\sigma}}$ in Cockcroft criterion, Eq. (5.8) is obtained.

$$\bar{\varepsilon}_f \left(\frac{\sigma_1}{\bar{\sigma}} \right) = const \tag{5.8}$$

To consider the influence of the maximum strain, the weighting value $\left(\frac{\bar{\varepsilon}}{\varepsilon_1} \right)^2$ is introduced to satisfy the experimental result. Eq. (5.8) can be rewritten in the following form:

$$\bar{\varepsilon}_f \left(\frac{\bar{\varepsilon}}{\varepsilon_1} \right)^2 \left(\frac{\sigma_1}{\bar{\sigma}} \right) = const = \bar{\varepsilon}_f \frac{\bar{\varepsilon}}{\varepsilon_1} \frac{d\bar{\varepsilon}}{d\varepsilon_1} \left(\frac{\sigma_1}{\bar{\sigma}} \right) \tag{5.9}$$

In addition, the stress-strain relationship can be expressed as:

$$d\varepsilon_1 = \frac{d\bar{\varepsilon}}{\bar{\sigma}} \left(\sigma_1 - \frac{\sigma_2}{2} - \frac{\sigma_3}{2} \right) = \frac{3}{2} \frac{d\bar{\varepsilon}}{\bar{\sigma}} \left(\sigma_1 - \frac{\sigma_1 + \sigma_2 + \sigma_3}{3} \right) = \frac{3}{2} \frac{d\bar{\varepsilon}}{\bar{\sigma}} (\sigma_1 - \sigma_m) \tag{5.10}$$

By combining Eqs. (5.9) and (5.10), the fracture criterion is described as:

$$\bar{\varepsilon}_f \frac{\bar{\varepsilon}}{\varepsilon_1} \frac{2\sigma_1}{3(\sigma_1 - \sigma_m)} = const \tag{5.11}$$

If the criterion is presented in a general form, Eq. (5.11) can thus be redesignated as:

$$\int_0^{\bar{\varepsilon}_f} \frac{2\sigma_1}{3(\sigma_1 - \sigma_m)} d\bar{\varepsilon} = C \tag{5.12}$$

where C is a material constant.

Rice and Tracey model is more focused on the modeling of fracture growth of micro void with sphere shape [55]. The model assumes that the fracture growth rate is affected by stress triaxiality $\frac{\sigma_m}{\bar{\sigma}}$. When stress triaxiality is high, the fracture growth rate of micro voids approximate to:

$$\frac{\dot{V}}{\dot{\varepsilon} V} = 0.85 e^{\frac{3\sigma_m}{2\bar{\sigma}}} \tag{5.13}$$

In Eq. (5.13), $\dot{V}$ is the volume growth rate of the micro voids. The final fracture criterion can be denoted as:

$$\int_0^{\varepsilon_f} e^{\alpha \frac{\sigma_m}{\bar{\sigma}}} = C \tag{5.14}$$

where α is material constant and C is the critical value of the criterion

The last criterion to be investigated in this chapter is Freudenthal criterion, which describes the influence of damage accumulation in plastic deformation process [42]. The integral of the equivalent stress provides the physical meaning of the energy required to initiate a crack tip per unit area. Freudenthal criterion is formulated as follows:

$$\int_0^{\varepsilon_f} \bar{\sigma} d\bar{\varepsilon} = C \tag{5.15}$$

Considering size effect, Freudenthal criterion is used in the fracture prediction of micro-scaled flanged upsetting process and the result is acceptable [4].

In this chapter, the above six DFCs are extensively investigated and identified via FEM simulation and experiment. Their applicability in micro-scaled plastic deformation is systematically explored and analyzed.

5.3 Research methodology and experiment

The purpose of this chapter is to study the applicability of DFCs in micro-scaled plastic deformation via comparing the difference of the prediction results in compression deformation process using the above six commonly used DFCs. These DFCs are widely used in macro-scaled plastic deformation. By using the conventional flow stress model and the hybrid flow stress model developed in previous chapters, the influence of size effect on the applicability of the six DFCs in ductile fracture prediction in micro-scaled deformation is considered. The prediction deviation of each criterion by using the conventional and hybrid flow stress models is calculated and compared. A generalized formulation for describing the common-used uncoupled DFCs is proposed and the explanation for prediction deviation is presented. The entire research methodology is illustrated in Fig. 5.1.

From experimental realization perspective, micro flanged upsetting is used to examine the applicability of different DFCs in this chapter. The main reason to choose this microforming process is that the process has a cross-shape shear band and the ductile fracture is easy to occur in this shear band. The multiphase alloy brass C3602 is used as the testing material. To obtain the different microstructures of the testing material, annealing of the materials was conducted. The heat treatment conditions and the average grain sizes of the material after annealing are presented in Table 3.1.

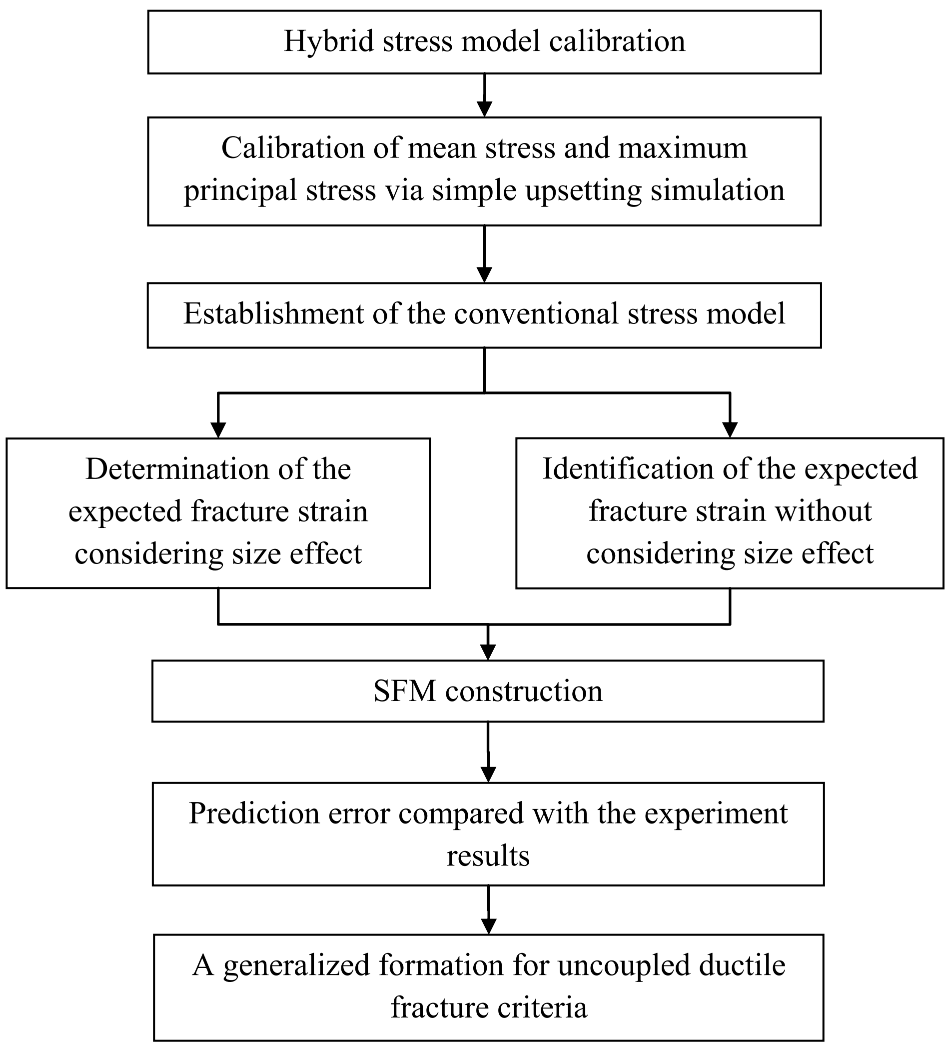

Fig. 5.1. A general research methodology.

For the micro flanged upsetting process, the punch velocity is set to the minimum value of the machine which is 0.01*mm/s* to ensure that the strain rate does not affect the experimental result. All the specimens are compressed to 75%, to ensure the occurrence of the macro-scaled fracture.

5.4 Criteria calibration in micro-scaled plastic deformation

5.4.1 Hybrid constitutive model

To explore the applicability of different DFCs, the hybrid model which considers the influences of size effect and each phase of the multiphase alloy in micro-scaled plastic deformation is presented in Eq. (4.14). By implying all the known coefficients and using curve fitting to determine all the unknown coefficients in Eq. (4.14), the final form of the hybrid constitutive model is shown in Eq. (4.16).

This model is used to predict the flow stress behavior in both the macro-scaled and micro-scaled deformation scenarios. As this model is established using the data of micro-scaled upsetting process, it can also be used to describe the equivalent stress in other micro-scaled deformation processes.

5.4.2 Hybrid-constitutive-model-based fracture prediction

The hybrid constitutive model shown in Eq. (4.16) is used for analysis of micro-scaled plastic deformation. This model is implemented to obtain the fracture critical value *C* for the testing material.

$$C = \int_0^{\varepsilon_f} \left(587.52\varepsilon^{0.23} + 0.681\varepsilon^{0.5} \cdot d^{-\frac{1}{2}} - \lambda \cdot \left(203.52\varepsilon^{0.23} + 0.681\varepsilon^{0.5} \cdot d^{-\frac{1}{2}} \right) \right) d\varepsilon \tag{4.18}$$

The formulation of the hybrid constitutive model is the integral of equivalent stress, and the physical meaning is the threshold energy required to initiate the stress-induced fracture with the fracture strain. When other uncoupled DFCs such as Cockcroft-model-based and stress-triaxiality-based fracture criteria are implemented, the mean stress and the maximum principal stress are needed for calculation of the critical value of each DFC. The upsetting simulation of each scenario with a specific heat treatment condition to obtain the principal stresses is conducted by using DEFORM 3D. All the upsetting simulation results are extracted and summarized into the form of $\sigma = k\varepsilon^n$ via curve fitting. The summarized results of the mean stress and the maximum principal stress are listed in Table 5.2.

Table 5.2 Mean stress and maximum principle stress for each scenario

	$2\times3mm$		$1\times1.5mm$		$0.5\times0.25mm$		$0.25\times0.375mm$	
	σ_m	σ^*	σ_m	σ^*	σ_m	σ^*	σ_m	σ^*
As Received	$368\varepsilon^{0.21}$	$725\varepsilon^{0.17}$	$716\varepsilon^{0.85}$	$1679\varepsilon^{0.93}$	$186\varepsilon^{0.21}$	$359\varepsilon^{0.14}$	$572\varepsilon^{0.24}$	$907\varepsilon^{0.09}$
$450°C$ *annealed*	$397\varepsilon^{0.51}$	$733\varepsilon^{0.38}$	$373\varepsilon^{0.45}$	$586\varepsilon^{0.29}$	$630\varepsilon^{0.95}$	$970\varepsilon^{0.64}$	$471\varepsilon^{0.23}$	$903\varepsilon^{0.15}$

$600°C$ *annealed*	$405\varepsilon^{0.65}$	$719\varepsilon^{0.46}$	$287\varepsilon^{0.49}$	$705\varepsilon^{0.52}$	$305\varepsilon^{0.53}$	$714\varepsilon^{0.54}$	$341\varepsilon^{0.43}$	$663\varepsilon^{0.31}$
$750°C$ *annealed*	$406\varepsilon^{1.1}$	$733\varepsilon^{0.72}$	$424\varepsilon^{0.92}$	$708\varepsilon^{0.69}$	$297\varepsilon^{0.66}$	$673\varepsilon^{0.64}$	$286\varepsilon^{0.7}$	$569\varepsilon^{0.56}$

By incorporating the corresponding parameters into each criterion, the critical value is thus determined. The expected fracture strain in simple upsetting process for each case is calculated and presented in Table 5.3.

Table 5.3 Expected fracture strain predicted with different fracture criteria

Fracture Criteria	Critical Value	Specimen Dimension			
		$2\times3mm$	$1\times1.5mm$	$0.5\times0.25mm$	$0.25\times0.375mm$
Freudenthal model	C = 684 (As received)	$\varepsilon_f = 1.15$	$\varepsilon_f = 1.16$	$\varepsilon_f = 1.19$	$\varepsilon_f = 1.26$
	C = 578 ($450^{\circ}C$ annealed)	$\varepsilon_f = 1.03$	$\varepsilon_f = 1.05$	$\varepsilon_f = 1.08$	$\varepsilon_f = 1.16$
	C = 698 ($600^{\circ}C$ annealed)	$\varepsilon_f = 1.11$	$\varepsilon_f = 1.15$	$\varepsilon_f = 1.22$	$\varepsilon_f = 1.36$
	C = 606 ($750^{\circ}C$ annealed)	$\varepsilon_f = 1.19$	$\varepsilon_f = 1.25$	$\varepsilon_f = 1.39$	$\varepsilon_f = 1.63$
Cockcroft model	C = 730 (As received)	$\varepsilon_f = 1.15$	$\varepsilon_f = 0.91$	$\varepsilon_f = 2.1$	$\varepsilon_f = 0.89$
	C = 553 ($450^{\circ}C$ annealed)	$\varepsilon_f = 1.03$	$\varepsilon_f = 1.17$	$\varepsilon_f = 0.96$	$\varepsilon_f = 0.74$
	C = 574 ($600^{\circ}C$ annealed)	$\varepsilon_f = 1.11$	$\varepsilon_f = 1.12$	$\varepsilon_f = 1.15$	$\varepsilon_f = 1.1$
	C = 575 ($750^{\circ}C$ annealed)	$\varepsilon_f = 1.19$	$\varepsilon_f = 1.21$	$\varepsilon_f = 1.23$	$\varepsilon_f = 1.34$

Oyane model	C = 2.68 (As received)	$\varepsilon_f = 1.15$	$\varepsilon_f = 1.03$	$\varepsilon_f = 1.58$	$\varepsilon_f = 0.82$
	C = 2.2 ($450^{\circ}C$ annealed)	$\varepsilon_f = 1.03$	$\varepsilon_f = 1.03$	$\varepsilon_f = 0.93$	$\varepsilon_f = 0.73$
	C = 2.39 ($600^{\circ}C$ annealed)	$\varepsilon_f = 1.11$	$\varepsilon_f = 1.22$	$\varepsilon_f = 1.16$	$\varepsilon_f = 0.99$
	C = 2.43 ($750^{\circ}C$ annealed)	$\varepsilon_f = 1.19$	$\varepsilon_f = 1.11$	$\varepsilon_f = 1.15$	$\varepsilon_f = 1.07$
Ayada model	C = 0.61 (As received)	$\varepsilon_f = 1.15$	$\varepsilon_f = 0.98$	$\varepsilon_f = 2.25$	$\varepsilon_f = 0.67$
	C = 0.47 ($450^{\circ}C$ annealed)	$\varepsilon_f = 1.03$	$\varepsilon_f = 1.03$	$\varepsilon_f = 0.9$	$\varepsilon_f = 0.57$
	C = 0.5 ($600^{\circ}C$ annealed)	$\varepsilon_f = 1.11$	$\varepsilon_f = 1.3$	$\varepsilon_f = 1.19$	$\varepsilon_f = 0.89$
	C = 0.46 ($750^{\circ}C$ annealed)	$\varepsilon_f = 1.19$	$\varepsilon_f = 1.07$	$\varepsilon_f = 1.11$	$\varepsilon_f = 0.96$
Brozzo model	C = 1.51 (As received)	$\varepsilon_f = 1.15$	$\varepsilon_f = 1.15$	$\varepsilon_f = 1.15$	$\varepsilon_f = 1$
	C = 1.34 ($450^{\circ}C$ annealed)	$\varepsilon_f = 1.03$	$\varepsilon_f = 0.9$	$\varepsilon_f = 0.97$	$\varepsilon_f = 1.03$
	C = 1.46 ($600^{\circ}C$ annealed)	$\varepsilon_f = 1.11$	$\varepsilon_f = 1.28$	$\varepsilon_f = 1.88$	$\varepsilon_f = 1.16$
	C = 1.45 ($750^{\circ}C$ annealed)	$\varepsilon_f = 1.19$	$\varepsilon_f = 1.07$	$\varepsilon_f = 1.86$	$\varepsilon_f = 1.18$
Rice&Tracey model	C = 2.55 (As received)	$\varepsilon_f = 1.15$	$\varepsilon_f = 0.96$	$\varepsilon_f = 1.69$	$\varepsilon_f = 0.58$
	C = 2.05 ($450^{\circ}C$ annealed)	$\varepsilon_f = 1.03$	$\varepsilon_f = 1.02$	$\varepsilon_f = 0.89$	$\varepsilon_f = 0.61$
	C = 2.04 ($600^{\circ}C$ annealed)	$\varepsilon_f = 1.11$	$\varepsilon_f = 1.15$	$\varepsilon_f = 1.09$	$\varepsilon_f = 0.88$
	C = 2.34 ($750^{\circ}C$ annealed)	$\varepsilon_f = 1.19$	$\varepsilon_f = 1.1$	$\varepsilon_f = 1.17$	$\varepsilon_f = 1.08$

5.4.3 Fracture prediction with the conventional stress model (without considering size effect)

As the size factor is introduced in the hybrid-constitutive-model-based fracture model (HFM), the conventional-constitutive–model-based fracture model (CFM) is thus needed to reveal the influence of size effect by comparing with the prediction accuracy of HFM. The size factor dependent part of Eq. (4.14) is removed and the flow stress model without considering the size effect is described in the following:

$$\sigma_{total}\left(\varepsilon\right) = Mk_2\varepsilon^{n_2} + f_\alpha \alpha M \mu_\alpha b_\alpha \sqrt{\frac{C_3\varepsilon}{b_\alpha L^s} + \frac{C_1\varepsilon}{b_\alpha d}} + \left(1 - f_\alpha\right)\alpha M \mu_\beta b_\beta \sqrt{\frac{C_3\varepsilon}{b_\beta L^s} + \frac{C_2\varepsilon}{b_\beta d}} \qquad (5.16)$$

By applying Eq. (5.16) to each fracture criterion, the expected fracture strain of CFM is obtained and presented in Table 5.4.

Table 5.4 Expected fracture strain using conventional stress model

Fracture Criteria	Critical Value	Specimen Dimension			
		$2\times3mm$	$1\times1.5mm$	$0.5\times0.25mm$	$0.25\times0.375mm$
Freudenthal model	C = 697 (As received)	$\varepsilon_f = 1.15$	$\varepsilon_f = 1.15$	$\varepsilon_f = 1.15$	$\varepsilon_f = 1.15$
	C = 592 ($450^\circ C$ annealed)	$\varepsilon_f = 1.03$	$\varepsilon_f = 1.03$	$\varepsilon_f = 1.03$	$\varepsilon_f = 1.03$
	C = 621 ($600^\circ C$ annealed)	$\varepsilon_f = 1.11$	$\varepsilon_f = 1.11$	$\varepsilon_f = 1.11$	$\varepsilon_f = 1.11$
	C = 654 ($750^\circ C$ annealed)	$\varepsilon_f = 1.19$	$\varepsilon_f = 1.19$	$\varepsilon_f = 1.19$	$\varepsilon_f = 1.19$
Cockcroft model	C = 730 (As received)	$\varepsilon_f = 1.15$	$\varepsilon_f = 0.91$	$\varepsilon_f = 2.1$	$\varepsilon_f = 0.89$
	C = 553 ($450^\circ C$ annealed)	$\varepsilon_f = 1.03$	$\varepsilon_f = 1.17$	$\varepsilon_f = 0.96$	$\varepsilon_f = 0.74$
	C = 574 ($600^\circ C$ annealed)	$\varepsilon_f = 1.11$	$\varepsilon_f = 1.12$	$\varepsilon_f = 1.15$	$\varepsilon_f = 1.1$

	C = 575 ($750^{\circ}C$ annealed)	$\varepsilon_f = 1.19$	$\varepsilon_f = 1.21$	$\varepsilon_f = 1.23$	$\varepsilon_f = 1.34$
Oyane model	C = 2.66 (As received)	$\varepsilon_f = 1.15$	$\varepsilon_f = 1.01$	$\varepsilon_f = 1.55$	$\varepsilon_f = 0.89$
	C = 2.18 ($450^{\circ}C$ annealed)	$\varepsilon_f = 1.03$	$\varepsilon_f = 1.04$	$\varepsilon_f = 0.96$	$\varepsilon_f = 0.81$
	C = 2.33 ($600^{\circ}C$ annealed)	$\varepsilon_f = 1.11$	$\varepsilon_f = 1.24$	$\varepsilon_f = 1.22$	$\varepsilon_f = 1.13$
	C = 2.34 ($750^{\circ}C$ annealed)	$\varepsilon_f = 1.19$	$\varepsilon_f = 1.14$	$\varepsilon_f = 1.25$	$\varepsilon_f = 1.28$
Ayada model	C = 0.6 (As received)	$\varepsilon_f = 1.15$	$\varepsilon_f = 0.99$	$\varepsilon_f = 2.41$	$\varepsilon_f = 0.75$
	C = 0.46 ($450^{\circ}C$ annealed)	$\varepsilon_f = 1.03$	$\varepsilon_f = 1.05$	$\varepsilon_f = 0.93$	$\varepsilon_f = 0.67$
	C = 0.49 ($600^{\circ}C$ annealed)	$\varepsilon_f = 1.11$	$\varepsilon_f = 1.35$	$\varepsilon_f = 1.31$	$\varepsilon_f = 1.13$
	C = 0.46 ($750^{\circ}C$ annealed)	$\varepsilon_f = 1.19$	$\varepsilon_f = 1.11$	$\varepsilon_f = 1.29$	$\varepsilon_f = 1.34$
Brozzo model	C = 1.51 (As received)	$\varepsilon_f = 1.15$	$\varepsilon_f = 1.15$	$\varepsilon_f = 1.15$	$\varepsilon_f = 1$
	C = 1.34 ($450^{\circ}C$ annealed)	$\varepsilon_f = 1.03$	$\varepsilon_f = 0.9$	$\varepsilon_f = 0.97$	$\varepsilon_f = 1.03$
	C = 1.46 ($600^{\circ}C$ annealed)	$\varepsilon_f = 1.11$	$\varepsilon_f = 1.28$	$\varepsilon_f = 1.88$	$\varepsilon_f = 1.16$
	C = 1.45 ($750^{\circ}C$ annealed)	$\varepsilon_f = 1.19$	$\varepsilon_f = 1.07$	$\varepsilon_f = 1.86$	$\varepsilon_f = 1.18$
Rice&Tracey model	C = 2.52 (As received)	$\varepsilon_f = 1.15$	$\varepsilon_f = 0.97$	$\varepsilon_f = 1.71$	$\varepsilon_f = 0.76$
	C = 2.41 ($450^{\circ}C$ annealed)	$\varepsilon_f = 1.03$	$\varepsilon_f = 1.22$	$\varepsilon_f = 1.03$	$\varepsilon_f = 0.87$
	C = 2.19 ($600^{\circ}C$ annealed)	$\varepsilon_f = 1.11$	$\varepsilon_f = 1.27$	$\varepsilon_f = 1.25$	$\varepsilon_f = 1.14$
	C = 2.21 ($750^{\circ}C$ annealed)	$\varepsilon_f = 1.19$	$\varepsilon_f = 1.14$	$\varepsilon_f = 1.28$	$\varepsilon_f = 1.32$

5.5 Result analysis and discussion

5.5.1 Comparison of the expected fracture strain

After the expected fracture strain is calculated, it can be compared with the actual experimental results. Fig. 5.2 shows the actual fracture strain and the expected fracture strain using different fracture criteria in upsetting process. In Fig. 5.2 (a), it is found that the prediction results using Brozzo and Ayada DFCs in macro-scaled plastic deformation are the closest to the experimental ones with the deviation of 4.9%. Meanwhile, Freudenthal model, which gives the worst performance, has the deviation of 12.6% compared with experiment. This could be caused by the different grain sizes of macro and micro-scaled specimens. To distinguish the different stress contribution arising from the grain and feature size effects, the macro- and micro-scaled specimens are annealed with the same heat treatment condition. Fig. 5.2 (b) shows the result comparison in micro scale. In the simple upsetting process with the specimen dimension of $0.5 \times 0.75mm$, the specimen does not show a major crack when the specimen height is reduced to 25% of its original one via compression. The long dash line in the picture is the predicted flow stress curve if no fracture occurs during the deformation process. For micro-scaled simple upsetting, however, Freudenthal criterion provides the best result with the deviation of only 3.7% between the calculation and experiment. Brozzo model has the worst performance with the deviation of 38.2%. It seems that the energy based method has a better performance in analysis of the micro-scaled compression forming.

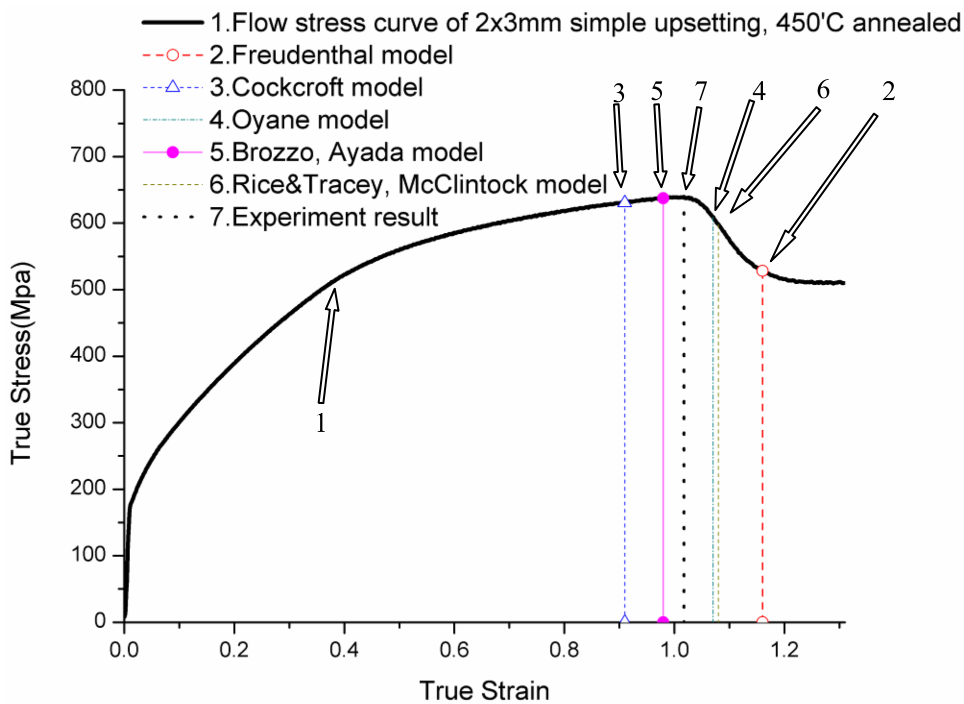

(a) macro scale

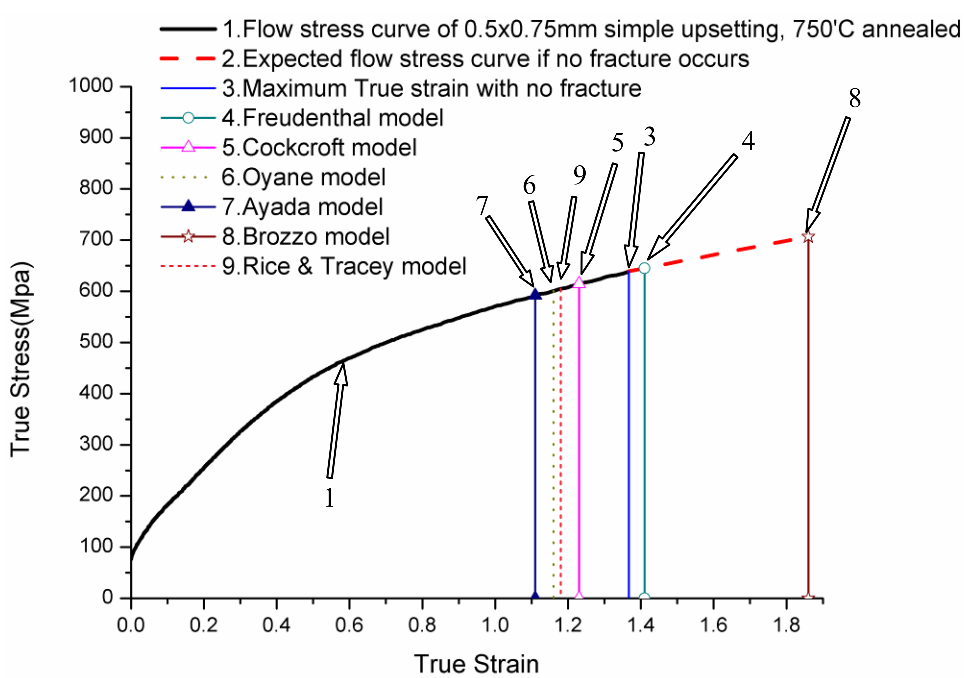

(b) micro scale

Fig. 5.2. Calculation and experimental result of fracture strain in macro and micro scale.

5.5.2 Stress-induced fracture map in DFC evaluation

SFM is a useful tool to analyze the different contribution of both grain and feature size effects. It is a three-dimensional diagram to schematically articulate the interaction relationship among the size effect, fracture energy and the expected fracture strain in micro-scaled plastic deformation of the multi-phase alloys. By using the expected fracture strain in Tables 5.3 and 5.4, the SFM based on the hybrid model and the conventional model can thus be constructed. Fig. 5.3 shows the SFM comparison between experiment and simulation. The experimental result represented by red star has the similar shape with the SFM of Freudenthal criterion. It indicates that the Freudenthal criterion can be used for both the macro-scaled and micro-scaled fracture prediction and provides a relatively accurate result.

Fig. 5.3 also shows the SFMs of Cockcroft & Latham, Rice & Tracey and SFM of Oyane criteria. Compared with the experimental results, these three criteria perform relatively well when the billet diameter is larger than 1 *mm*. When the billet diameter is 0.5 and 0.25*mm*, which is in the micro-scaled forming category, the SFM has an deviation of 28%, 36% and 41% by comparing the expected fracture strain obtained from simulation and experiment. The SFM indicates that these three DFCs should be used to predict fracture in macro-scaled deformation processes.

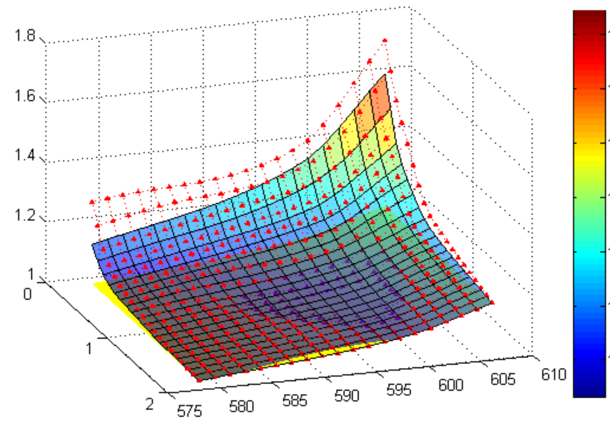

(a) Freudenthal

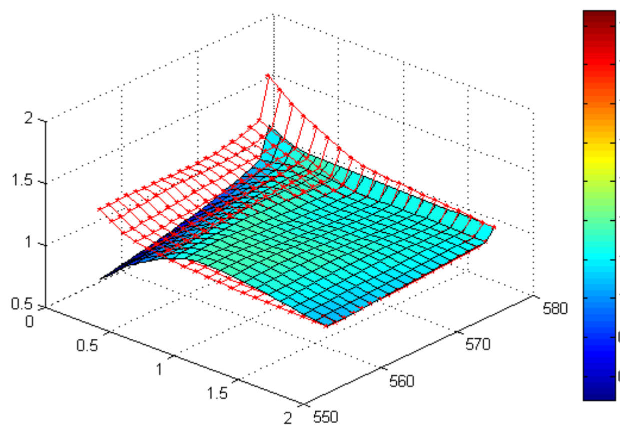

(b) Cockcroft & Latham

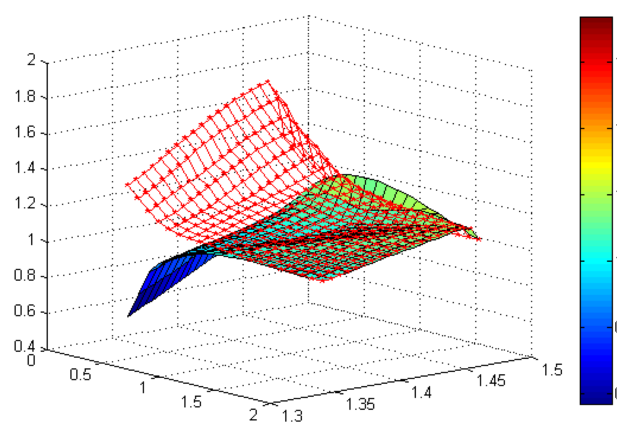

(c) Brozzo

Fig. 5.3. SFM of uncoupled fracture criteria.

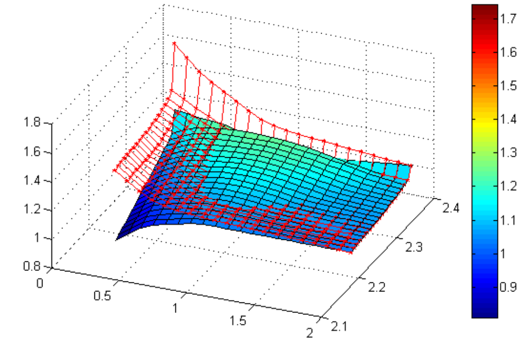

(d) Oyane (without considering size effect)

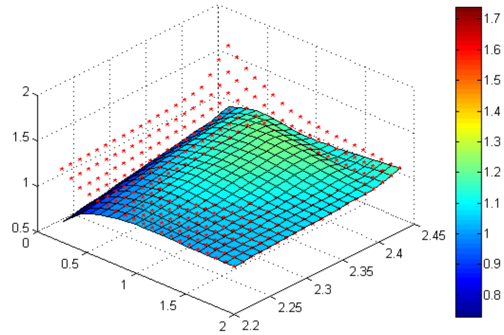

(e) Oyane (considering size effect)

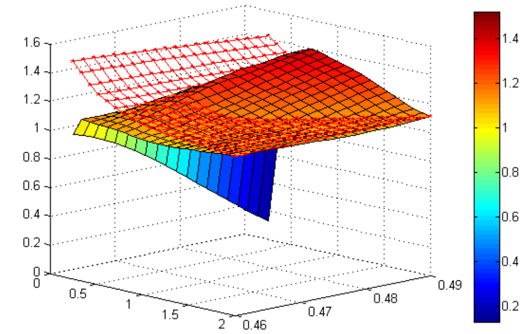

(f) Ayada (without considering size effect)

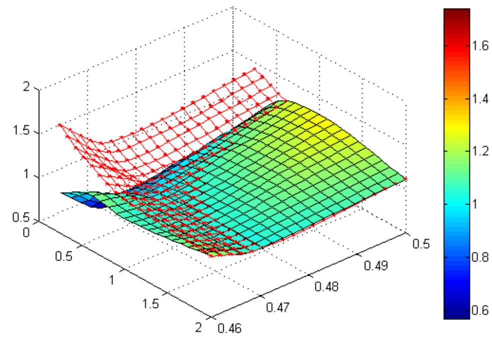

(g) Ayada (considering size effect)

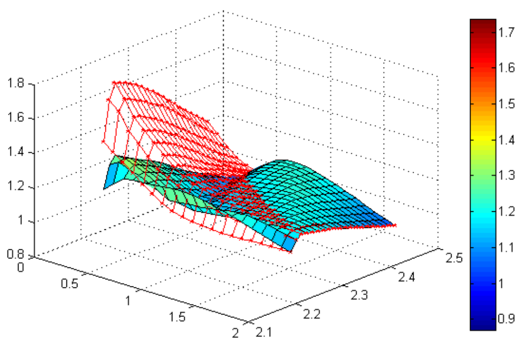

(h) Rice & Tracey (without considering size effect)

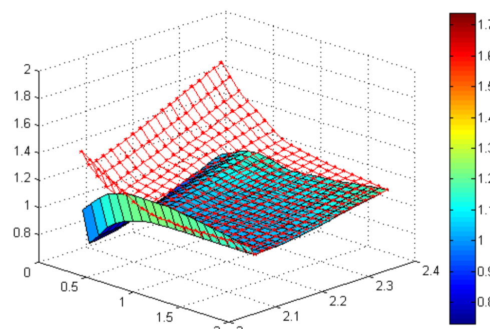

(i) Rice & Tracey (considering size effect)

Fig. 5.3. SFM of uncoupled fracture criteria (cont'd).

To evaluate the influence of size factor in fracture prediction, Figs. 5.4, 5.5 and 5.6, which show the deviation evaluation of each criterion, are constructed. In Fig. 5.4, it can be seen that the deviation of HFM is less than 11%, which is very promising compared with the conventional fracture models. The CFM shows a good result in macro scale, but the deviation increases when the geometry size of the specimen becomes smaller, which is a direct proof of the influence of size effect. In addition, Fig. 5.5 shows the deviation between the actual experimental result and the calculation ones based on Brozzo and C&L criteria. The size effect does not directly affect the calculation result, since the expected fracture strain with or without considering size effect is the same for these two criteria. When the specimen dimension is less than 0.5mm, the predicted result has an over 40% deviation compared with the experimental result. The deviation percentage of the rest three fracture criteria including Ayada, Oyane and Rice & Tracey criteria are shown in Fig. 5.6. These three criteria have one thing in common: the fracture prediction result by using the conventional constitutive model is much more accurate than the result by using hybrid constitutive model. The reason for this will be explained in the section 5.5.3.

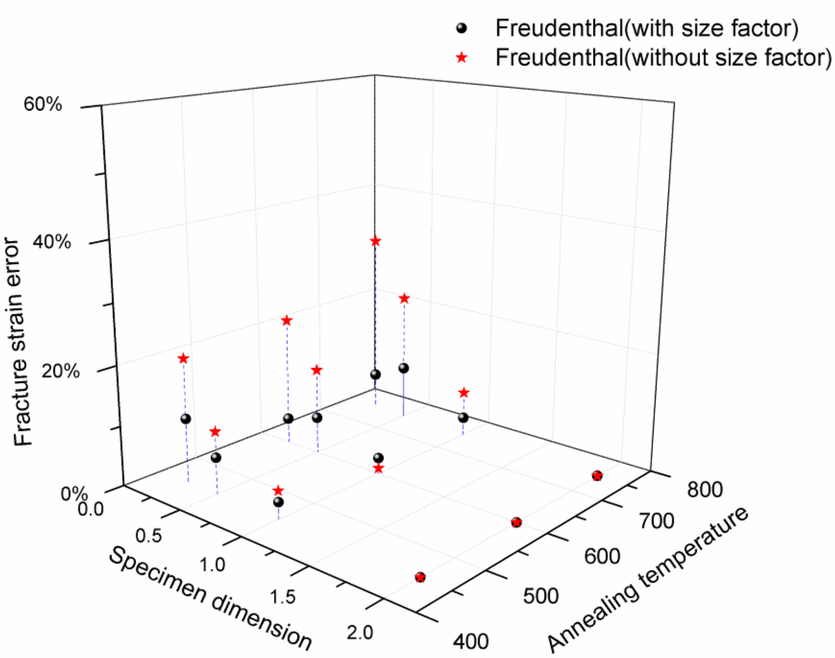

Fig. 5.4. Deviation evaluation using Freudenthal criterion.

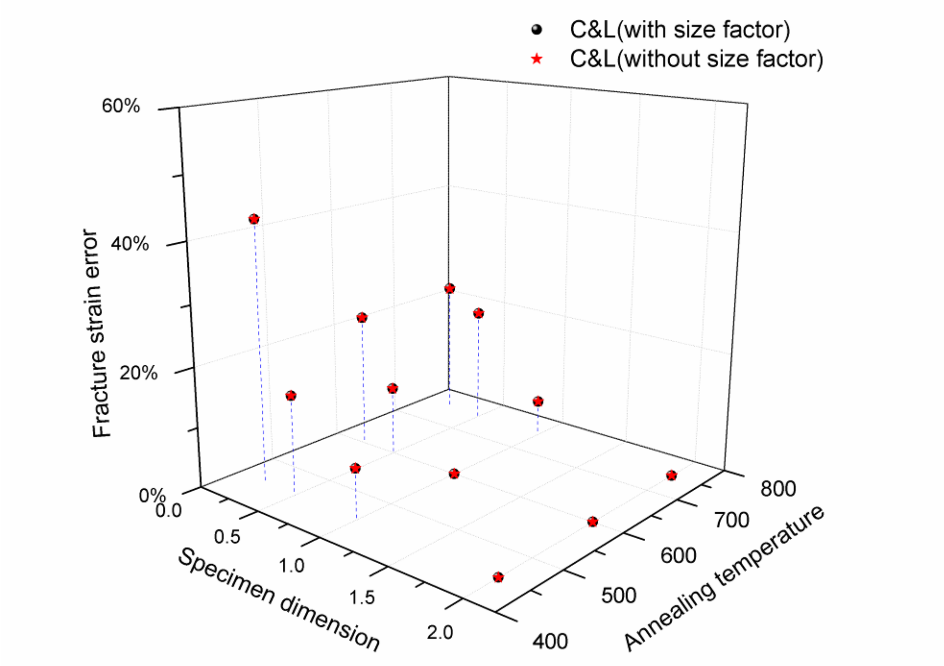

(a) Cockcroft & Latham

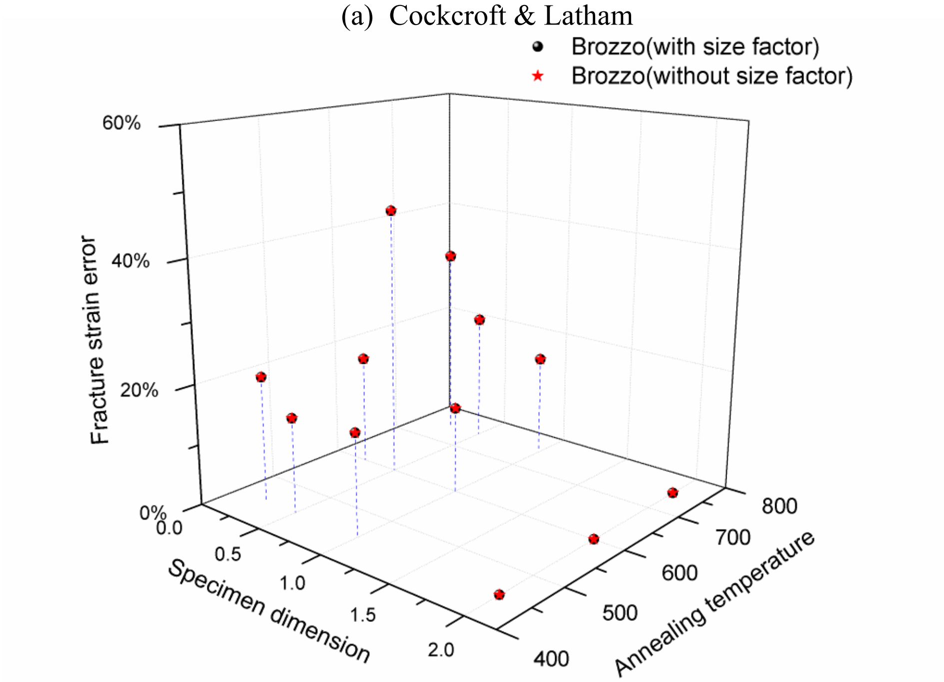

(b) Brozzo

Fig. 5.5. Deviation evaluation using Cockcroft & Latham and Brozzo criterion.

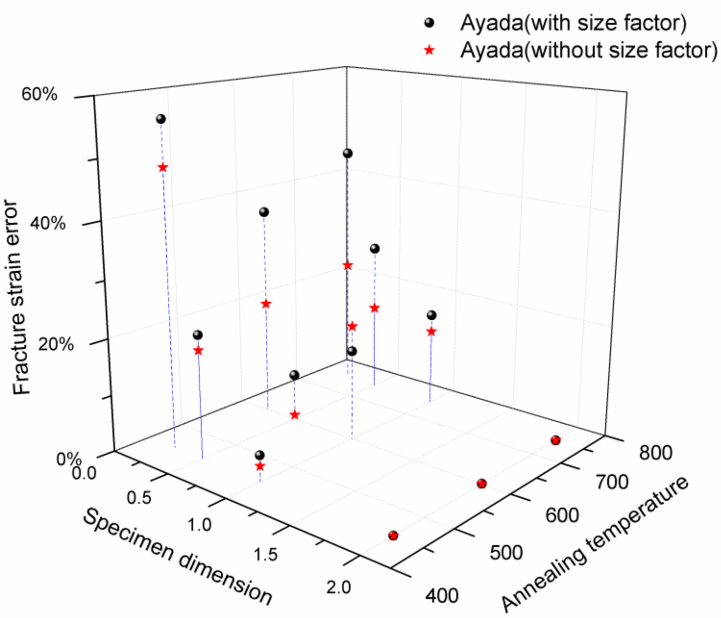

Ayada

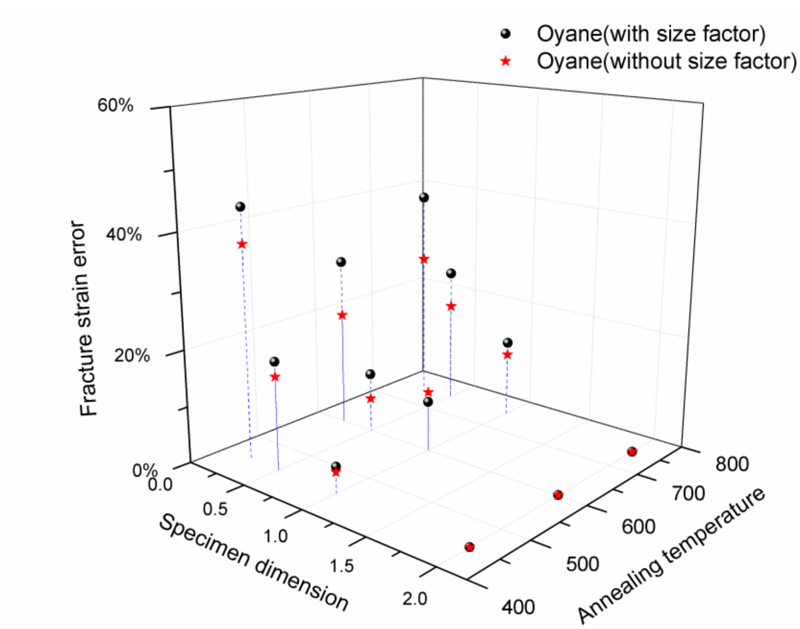

Oyane

Fig. 5.6. Deviation evaluation using Ayada, Oyane and Rice & Tracey criterion.

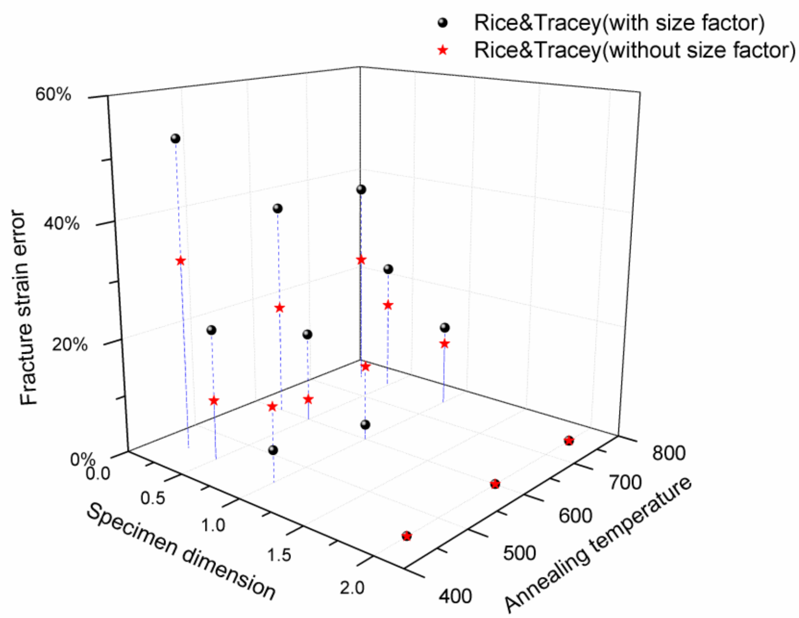

Rice & Tracey

Fig. 5.6 Deviation evaluation of Ayada, Oyane and Rice & Tracey criteria. (cont'd)

5.5.3 The generalized fracture model formulation

Among various DFCs, the coupled criteria assume that most ductile fracture are caused by void accumulation and growth, which further lead to macro-scaled fracture. The coupled criteria introduce the damage factor D to simulate the void growth in plastic deformation process. As most of these criteria use tensile test to determine the critical value, their application in prediction of tensile-dominative deformation is acceptable. However, the accuracy of coupled fracture criteria in compression-dominative deformation is beyond satisfactory.

Void-growth-based fracture criteria such as GTN and McClintock DFCs are not well applicable to compression-dominative deformation [56]. The main reason is that the fracture initiation and growth in tensile test is caused by both the void growth and shear stress concentration. In compression-dominative deformation, however, void can hardly exist inside the specimen. Unlike the tensile-dominative deformation, when the brittle phase or impurity in the multiphase metal is broken down under compression stress, the void will immediately be replaced by the rest part of specimen. Thus, the existence of ductile fracture in the compression-dominative deformation is mainly caused by shear stress concentration.

For the conventional DFCs listed in Table 5.1, the critical value is the key factor to evaluate the existence of ductile fracture. As mentioned in Eq. (1.1), the integral of the strain related function changes in deformation process and becomes the critical value C when the strain value reaches the fracture strain, as shown in Eq. (5.17).

$$F\left(\varepsilon_f\right)=C \tag{5.17}$$

In Eq. (5.17), $F\left(\varepsilon\right)$ is the damage value function, ε_f is the fracture strain and C is the critical value. For each fracture criterion, its simplified form can be written as a strain related exponent function.

In tensile-dominative deformation, stress triaxiality is critical to determine whether void growth or shear stress concentration has a major contribution in fracture initiation. In compression deformation, stress triaxiality and non-dimensional stress-concentration factor, which is presented in Cockcroft & Latham model, are considered as the two important factors which affect the damage value function $F(\varepsilon)$. Table 5.5 presents the generalized formulations of different DFCs. Most of the uncoupled DFCs can be represented by the integral of stress triaxiality, non-dimensional stress-concentration factor and mean stress. The damage value function is described by Eq. (5.18)

$$F = \int \mu(\varepsilon)^{n_1} \cdot \eta(\varepsilon)^{n_2} \cdot \sigma_m^{\ n_3} d\varepsilon \tag{5.18}$$

In Eq. (5.18), $\mu(\varepsilon)$ is the stress concentration factor which equals to $\frac{\sigma_1}{\overline{\sigma}}$, $\eta(\varepsilon)$ is the stress triaxiality and designated as $\frac{\sigma_m}{\overline{\sigma}}$. This equation reveals the physical meaning of the damage value function that the fracture initiation is caused by stress concentration and affected by the contribution of void growth and the magnitude of deformation force.

Table 5.5 Generalization of various uncoupled fracture criteria

Freudenthal	$F = \int \overline{\sigma} d\overline{\varepsilon} = \int \left(\frac{1}{\frac{\sigma_m}{\overline{\sigma}}} \cdot \sigma_m \right) d\overline{\varepsilon} = \int \frac{1}{\eta} \cdot \sigma_m d\overline{\varepsilon}$
Cockcroft & Latham	$F = \int \sigma_1 d\overline{\varepsilon} = \int \sigma_m \cdot \frac{\overline{\sigma}}{\sigma_m} \cdot \frac{\sigma_1}{\overline{\sigma}} d\overline{\varepsilon} = \int \frac{\mu}{\eta} \cdot \sigma_m d\overline{\varepsilon}$
Ayada	$F = \int \frac{\sigma_m}{\overline{\sigma}} d\overline{\varepsilon} = \int \eta d\overline{\varepsilon}$
Oyane	$F = \int \left(1 + A \frac{\sigma_m}{\overline{\sigma}} \right) d\overline{\varepsilon} = \int (1 + A \cdot \eta) d\overline{\varepsilon}$

Brozzo	$F=\int \frac{2\sigma_1}{3(\sigma_1-\sigma_m)}d\bar{\varepsilon}=\int \frac{2\frac{\sigma_1}{\bar{\sigma}}}{3\left(\frac{\sigma_1}{\bar{\sigma}}-\frac{\sigma_m}{\bar{\sigma}}\right)}d\bar{\varepsilon}=\int \frac{2}{3\left(1-\frac{\eta}{\mu}\right)}d\bar{\varepsilon}$
Rice & Tracey	$F=\int e^{1.5\frac{\sigma_m}{\bar{\sigma}}}d\bar{\varepsilon}=\int e^{1.5\eta}d\bar{\varepsilon}$

Regarding the deviation of different fracture criteria presented in Section 5.3, it can be explained by the general formulations presented in Table 5.5. In Table 5.5, the stress triaxiality of Freudenthal criteria is the only one which is inversely proportional to damage value function. According to the deformation of multiphase alloy, the decrease of stress triaxiality means that the main contribution to fracture initiation comes from shear stress concentration. In upsetting experiment, it is found that when the specimen size becomes smaller, the stress triaxiality of macro-scaled deformation is smaller than that of micro-scaled deformation, as shown in Fig. 5.7(a). The equation of Freudenthal criterion in Table 5.5 can thus be re-designated in the following:

$$F=\int \frac{1}{\eta_{\lambda-dep}}\cdot\sigma_m d\varepsilon_{\lambda-dep}=\int \frac{1}{\frac{\sigma_m}{587.52\varepsilon^{0.23}+0.681\varepsilon^{0.5}\cdot d^{-\frac{1}{2}}-\lambda\cdot\left(203.52\varepsilon^{0.23}+0.681\varepsilon^{0.5}\cdot d^{-\frac{1}{2}}\right)}}\cdot\sigma_m d\varepsilon_{\lambda-dep}$$

$$F=\int \frac{1}{\eta_{\lambda-ind}}\cdot\sigma_m d\varepsilon_{\lambda-ind}=\int \frac{1}{\frac{\sigma_m}{587.52\varepsilon^{0.23}+0.681\varepsilon^{0.5}\cdot d^{-\frac{1}{2}}}}\cdot\sigma_m d\varepsilon_{\lambda-ind} \tag{5.19}$$

The first equation of Eq. (5.19) is the damage value function considering size effect, while the second one does not consider this effect. In micro scale, it is obvious that the stress triaxiality considering size effect $\eta_{\lambda-dep}$ is larger than the one which does not consider size effect $\eta_{\lambda-ind}$. To obtain the same damage value F, the expected fracture strain $\varepsilon_{\lambda-dep}$ in consideration of size effect, needs to be larger than $\varepsilon_{\lambda-ind}$. The expected fracture strain is thus closer to the experimental results.

The stress triaxiality in Ayada, Oyane and Rice & Tracey criteria, on the other hand, are all proportional to the damage value function. The influence of size factor makes the calculation result even more deviated from the experimental result. Taking Ayada criterion as an instance, which can be re-designated in Eq. (5.20) as follows:

$$F = \int \eta_{\lambda-dep} d\varepsilon_{\lambda-dep} = \int \frac{\sigma_m}{587.52\varepsilon^{0.23} + 0.681\varepsilon^{0.5} \cdot d^{-\frac{1}{2}} - \lambda \cdot \left(203.52\varepsilon^{0.23} + 0.681\varepsilon^{0.5} \cdot d^{-\frac{1}{2}} \right)} d\varepsilon_{\lambda-dep}$$

$$F = \int \eta_{\lambda-ind} d\varepsilon_{\lambda-ind} = \int \frac{\sigma_m}{587.52\varepsilon^{0.23} + 0.681\varepsilon^{0.5} \cdot d^{-\frac{1}{2}}} d\varepsilon_{\lambda-ind} \tag{5.20}$$

As mentioned above, $\eta_{\lambda-dep}$ is larger than $\eta_{\lambda-ind}$, $\varepsilon_{\lambda-dep}$ needs to be smaller than $\varepsilon_{\lambda-ind}$ to obtain the same damage value and thus makes $\varepsilon_{\lambda-dep}$ more deviation from the actual experimental result. This conclusion reveals why the fracture prediction result by using the conventional constitutive model is better than the one using the hybrid constitutive model when Ayada, Oyane and Rice & Tracey DFCs are used.

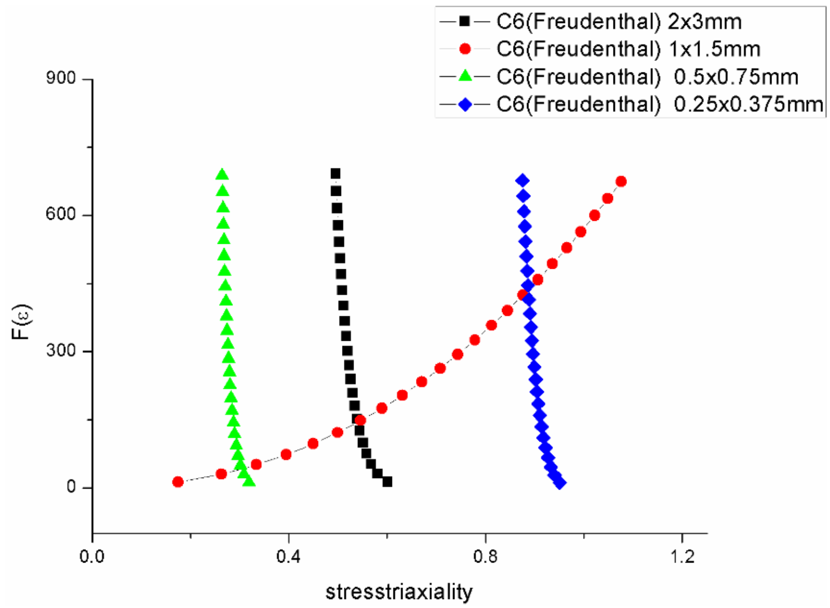

(a) As recevied

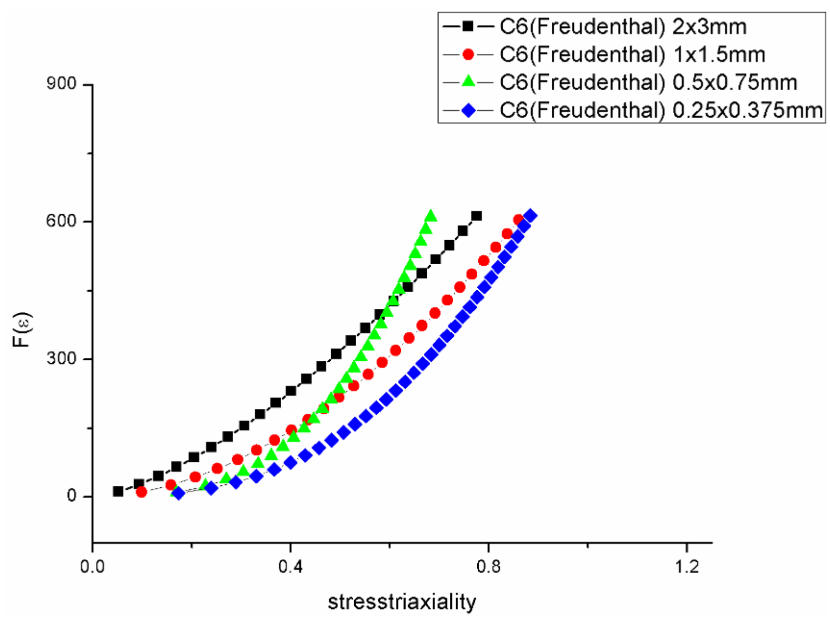

(b) 750 degree annealed

Fig. 5.7 Relationship between the damage value and stress triaxiality

Based on HFM and the data obtained in the previous section, the FE simulations for micro-scaled flanged upsetting are thus conducted in DEFORM 3D, and the result is demonstrated in Figs. 5.8 and 5.9. In Fig. 5.8, it is found that the Freudenthal fracture criterion is the only applicable DFC that can predict fracture in macro-scaled flanged upsetting. For other fracture criteria, as the damage value does not reach its own critical value, no fracture initiates in these scenarios, and their load stroke curves are almost the same. In Fig. 5.9, the simulation result of the micro-scaled flanged upsetting shows that no fracture exists by applying all the DFCs. As the load-stroke curve is pretty close to experimental result, Freudenthal criterion is thus considered to be the most suitable DFC in micro-scaled flanged upsetting process.

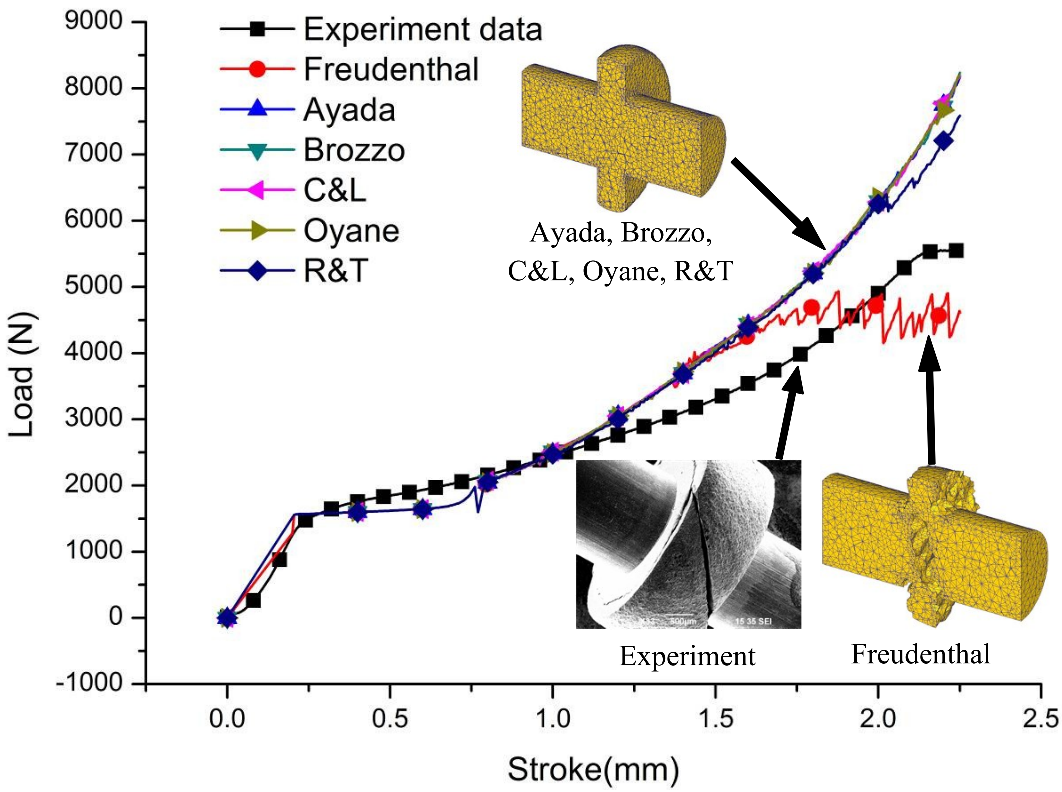

Fig. 5.8 Simulation and experimental verification for macro-scaled flanged upsetting.

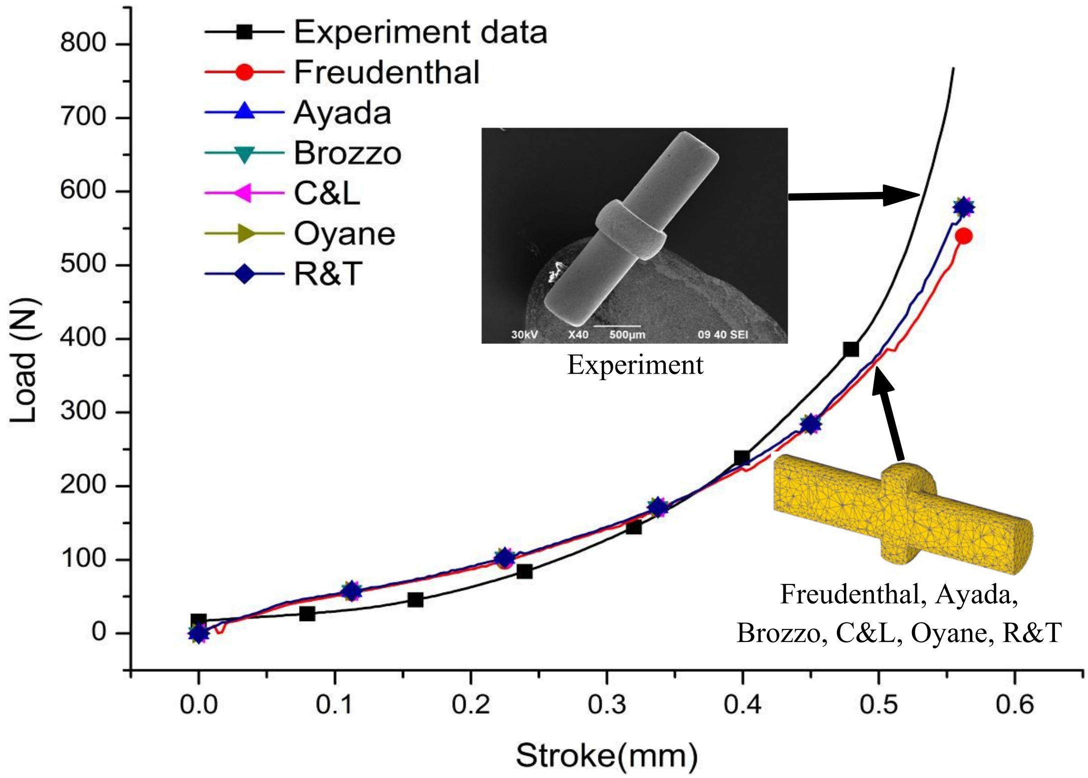

Fig. 5.9 Simulation and experimental verification for macro-scaled flanged upsetting.

5.6 Summary

The applicability of six most widely used fracture criteria in micro-scaled plastic deformation are examined and calibrated. Each DFC together with the hybrid constitutive model is implemented for fracture prediction in both the macro- and micro-scaled deformation scenarios. Through simulation and experiment, the following conclusions are made:

(1) Freudenthal criterion is the most suitable criterion for compression-dominative deformation processes in both macro and micro scales. The SFM based on Freudenthal criterion is close to the experiment.

(2) In compression-dominative deformation, the applicability of Cockcroft & Latham and Brozzo criteria is limited. The Ayada, Rice and Tracey, and Oyane criteria are able to predict the ductile fracture in both the macro and micro scales when the constitutive model without considering size effect is used. Introducing the size factor into these DFCs makes the prediction results have a greater deviation from the experimental results.

By using Freudenthal criterion, only flow stress curve is needed for fracture prediction. Other DFCs, however, need principal stress to calculate the fracture critical value *C*. Freudenthal DFC is thus the most convenient one for micro-scaled fracture prediction.

Chapter 6 Ductile Fracture in Micro-scaled Sheet Metal Forming

6.1 Introduction

This chapter deals with the size effect influence over ductile fracture in micro-scaled sheet metal forming. Micro-scaled sheet forming such as blanking, three-point bending and deep drawing, is widely used in many industries such as microelectronics and consumer electronics. Considering the product cost and efficiency of microforming against other micro-scaled manufacturing, many of the existing products are explored to be fabricated by microforming instead of the traditional manufacturing method [57-63]. In this chapter, micro-scaled sheet metal deep drawing part is the target deformation process to be studied.

6.2 Size factor of sheet metal

Similar to micro-scaled bulk forming presented in the previous chapters, the constitutive model based on the surface layer model is proposed to analyze the influence of size effect in micro-scaled sheet metal forming process. In this chapter, the grain size effect will be mainly discussed, as show in Fig. 6.1.

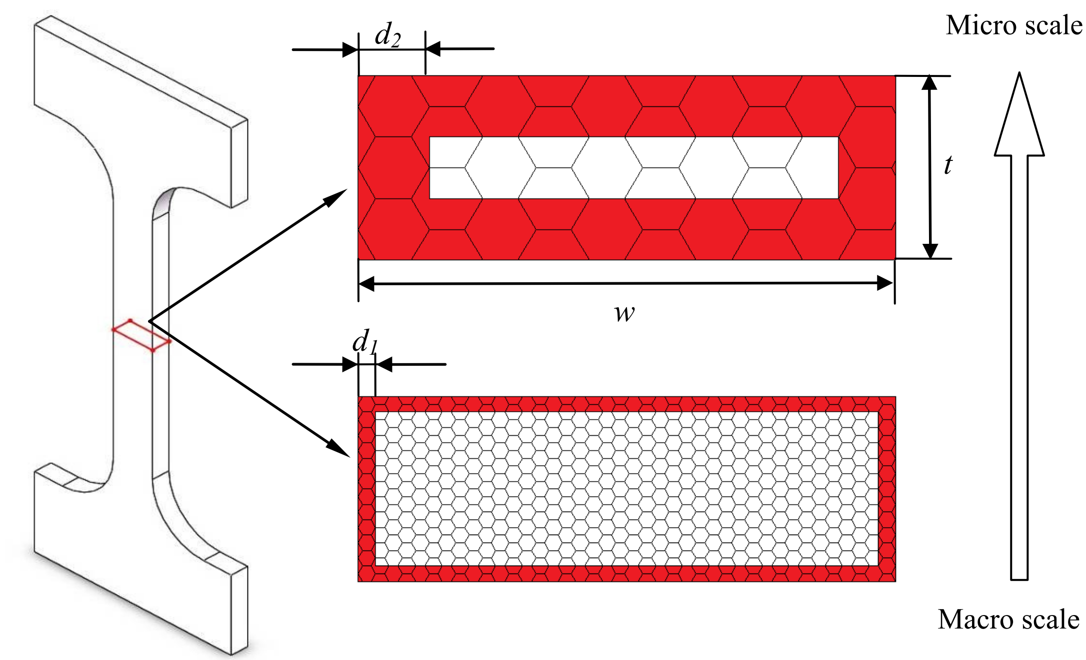

Fig. 6.1. Surface grain proportion of different scales.

Fig. 6.1 schematizes the surface grain proportion of different scales. The grains shaded with red color represent the surface layer grains and the rest part is the internal grains. t is the thickness of the sheet metal, w is the width of the sheet metal and d_1, d_2 is the grain size of as-received sample and the one annealed at $750^\circ C$. As this chapter mainly focuses on the grain size effect, w and t thus remain the same for these two scenarios as the feature dimension of the grain size effect is the same. The surface grain number can be represented as:

$$N_s = \frac{w \cdot t - \left(\left(w - 2d \right) \cdot \left(t - 2d \right) \right)}{\pi \cdot d^2 / 4}$$
$$N_s = 1 \left(w = t = d \right) \tag{6.1}$$

The size factor is thus determined as:

$$\lambda = \frac{N_s}{N} = \frac{\dfrac{w \cdot t - \left(\left(w - 2d \right) \cdot \left(t - 2d \right) \right)}{\pi \cdot d^2 / 4}}{\dfrac{w \cdot t}{\pi \cdot d^2 / 4}} = \frac{2dw + 2dt - 4d^2}{w \cdot t} \tag{6.2}$$

Unlike the size factor of feature size effect in Peng's research [29], the size factor of grain size effect cannot be simplified as $\lambda = \frac{d}{t}$ because the grain size becomes very close to the thickness and significantly affects the magnitude of size factor.

6.3 Research issue

In micro-scaled sheet metal forming, the feature dimension, especially for the thickness of sheet metal is the most important factor as there will be only several grains along the thickness direction after heat treatment. In this chapter, micro-scaled deep drawing will be discussed and the corresponding constitutive model is established. The coefficient of the model is calculated based on the experimental result of the tensile test of the as-received brass sheet with thickness of 0.2mm. The experimental results of the deep drawing test are thus compared with the simulation results. The general methodology is presented in Fig. 6.2. Similar to Chapter 3, the size factor is calculated after grain size is known from microstructure observation. The unknown coefficient of the constitutive model for sheet metal is then obtained via curve fitting using the size factor and flow stress curve of tensile test. Therefore, the fracture in micro-scaled deep drawing can be predicted via FE simulation and the predicted load-stroke curve is compared with the experimental results.

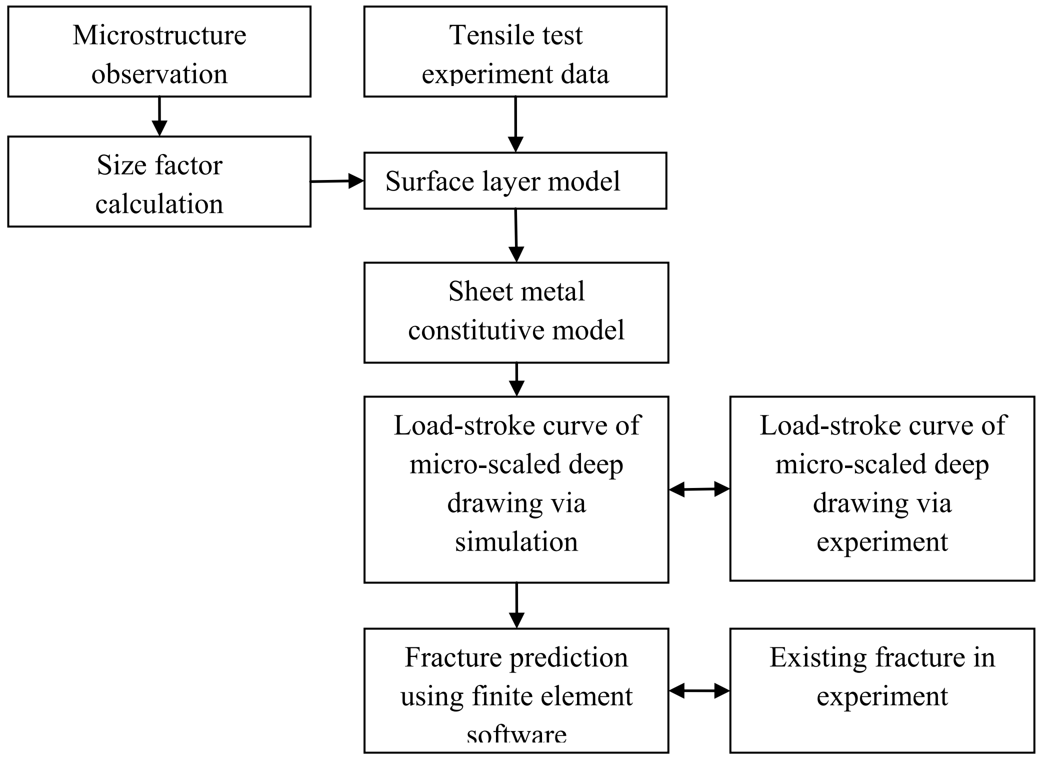

Fig. 6.2. General methodology of micro-scaled sheet metal forming.

6.4 Experiment

In this chapter, brass C2680R is used as the testing material. The thickness of the specimen for tensile test is $0.2mm$ and the width is $10mm$. The specimens are annealed in protective Argon atmosphere with different temperatures and holding times. The heat treatment conditions are listed in Table 6.1.

Table 6.1 Heat treatment conditions of sheet metal specimen

Scenario	Target temperature	Dwelling time	Grain size
1	As-received	As-received	$17\mu m$
2	$500^{\circ}C$	$2h$	$25\mu m$

3	$600^{\circ}C$	$2h$	$66\mu m$
4	$750^{\circ}C$	$3h$	$160\mu m$

After heat treatment, the specimens of the four scenarios shown in Table 6.1 are polished and etched for metallographic examination. The grain size for each scenario is shown in Fig. 6.3.

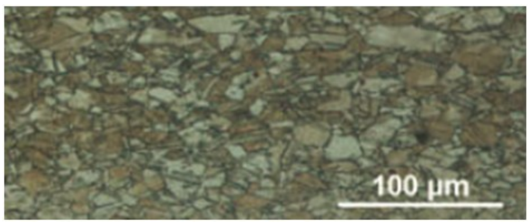

As-received specimen, $d = 17\mu m$

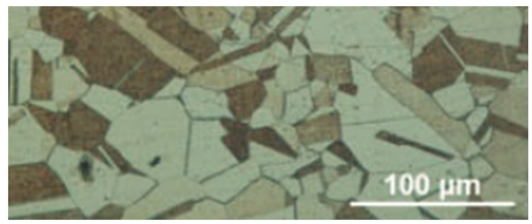

500℃ annealed specimen, $d = 25\mu m$

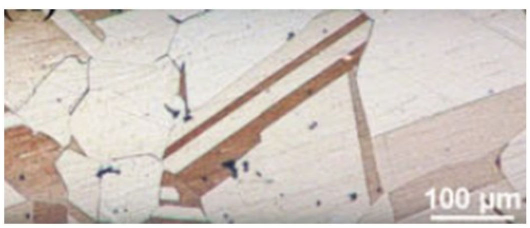

600℃ annealed specimen, $d = 66\mu m$

750℃ annealed specimen, $d = 160\mu m$

Fig. 6.3. Microstructure of different heat treatment scenarios [64].

The tensile test for scenario 1 to 4 is conducted on a MTS testing machine with an extensometer after the heat treatment is completed. The testing speed is 0.01*mm/s* to eliminate the influence of strain rate and each specimen undergoes plastic deformation until major cracks occur. The load-stroke curve of each scenario is thus extracted and transformed into true stress-strain curve, which is demonstrated in Fig. 6.4. They are then used for curve fitting and result comparison after the constitutive model is established.

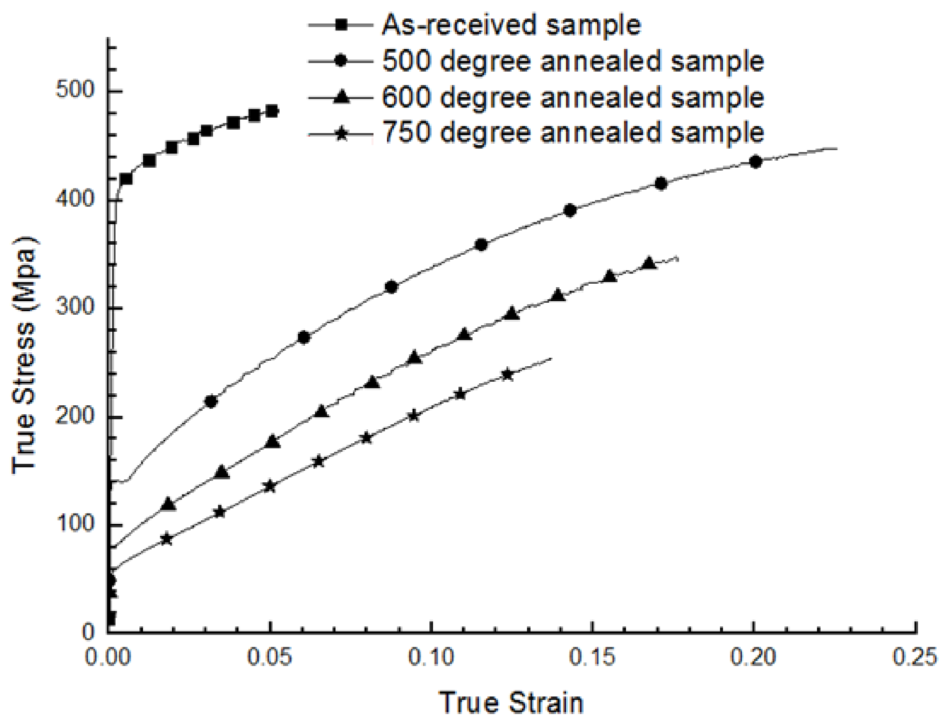

Fig. 6.4. Stress-strain curves of sheet metal specimens [64].

The micro-scaled deep drawing is thus conducted. The original sheet material is wire cut into a circle with the diameter of 3*mm*, and then placed between the die and holding pad. When the deep drawing deformation is finished, the formed part will be kept in die cavity, as the contact surface of the die is larger than the contact surface of the punch. In order to protect the formed part after deep drawing process, the die is split into two parts such that the formed part can be easily ejected out from the die. The die set is shown in Fig. 6.5.

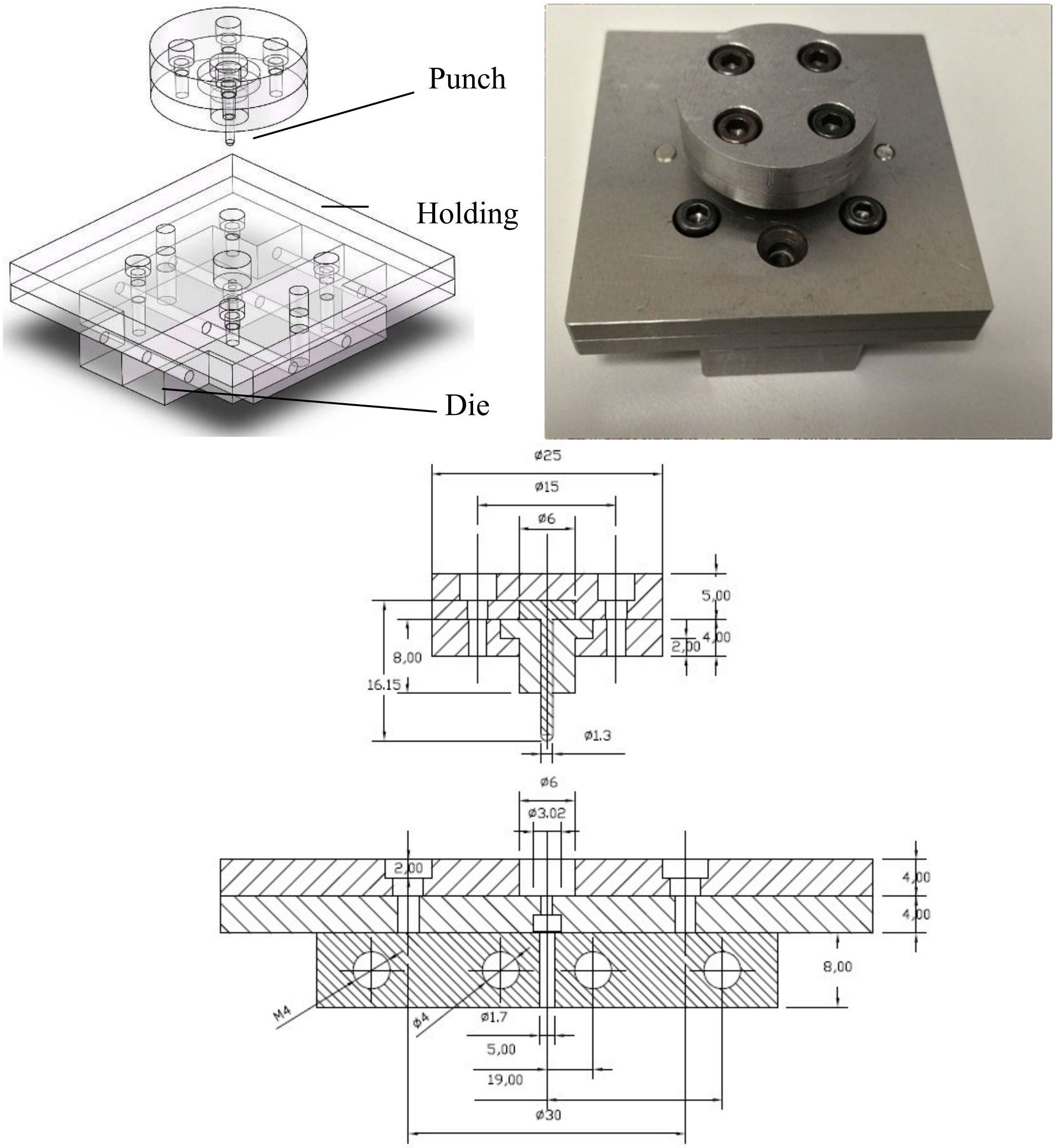

Fig. 6.5. Die set of micro-scaled deep drawing process.

6.5 Constitutive model of sheet metal forming

The constitutive model of sheet metal in this chapter is based on the surface layer model. The flow stress of the sheet metal in deformation process is represented in the following:

$$\begin{aligned}\sigma &= \frac{N_s\sigma_s + N_i\sigma_i}{N} \\ &= \frac{N_s \cdot m\tau_R\left(\varepsilon\right) + N_i \cdot \left(M\tau_R\left(\varepsilon\right) + \frac{k\left(\varepsilon\right)}{\sqrt{d}}\right)}{N} \\ &= M\tau_R\left(\varepsilon\right) + \frac{k\left(\varepsilon\right)}{\sqrt{d}} + \lambda \cdot \left(m\tau_R\left(\varepsilon\right) - M\tau_R\left(\varepsilon\right) - \frac{k\left(\varepsilon\right)}{\sqrt{d}}\right)\end{aligned} \tag{6.3}$$

Eq. (6.3) is similar to Eq. (3.3) in Chapter 3 except for the size factor λ. The calculation method of size factor λ is given in Section 6.2.

In Eq. (6.3), $M\tau_R\left(\varepsilon\right) + \frac{k\left(\varepsilon\right)}{\sqrt{d}}$ is used as the general stress form of polycrystalline grain. In Chapter 4, HCM, which is considered to be more accurate, is proposed for multiphase metal such as brass. In HCM, the $k\left(\varepsilon\right)$ in $M\tau_R\left(\varepsilon\right) + \frac{k\left(\varepsilon\right)}{\sqrt{d}}$ is calculated with dislocation theory and the coefficient of $k\left(\varepsilon\right)$ is obtained via a three-stage curve fitting. However, this model is not suitable as the primary objective of this research is to discuss the influence of grain size effect in micro-scaled sheet forming and the feature dimension remains the same for different scenarios. To obtain the final form of the constitutive model by using the experimental data of the as-received samples to conduct curve fitting, the number of unknown coefficient must be reduced to two in $M\tau_R\left(\varepsilon\right)+\frac{k\left(\varepsilon\right)}{\sqrt{d}}$ for curve fitting. The HCM in Chapter 4 has five unknown coefficients, and the flow stress data of the as-received samples with more than three scenarios of different dimensions is needed for the curve fitting to calculate these unknown coefficients. Therefore, the general stress form of the polycrystalline grain is designated as $M\tau_R\left(\varepsilon\right)+\frac{k\left(\varepsilon\right)}{\sqrt{d}}$ as this form has only two unknown coefficients.

According to Table 6.1 and Eq. (6.2), the size factor for each scale is calculated and listed in Table 6.2. In Scenario 4, the calculated size factor equals to 1.58 and the reason for this is the grain size of $160\mu m$, which is larger than half of the specimen thickness. This means in this scenario, most places along thickness direction will have only two grains or even one single grain. Therefore, the size factor of this scenario is 1 as all the grains have free surfaces.

Table 6.2 Size factor for each heat treatment scenarios.

Heat treatment condition	As-received	500	600	750
Size factor	17.28%	25.38%	66.44%	100%

Similar to Chapter 3, the form of $\tau_R\left(\varepsilon\right)$ and $k\left(\varepsilon\right)$ is simplified as $k\varepsilon^n$ for faster calculation. In Eq. (6.3), M is the Taylor factor with has the value of 3.06 and the grain orientation factor m is 2. Based on the true stress – strain curve of the as-received sample and the samples annealed at $500^{\circ}C$, the curve fitting is conducted and the coefficient of $\tau_R(\varepsilon)$ and $k(\varepsilon)$ is obtained as follows:

$$\begin{aligned} \tau_R(\varepsilon) &= 1730\varepsilon^{0.03} \\ k(\varepsilon) &= 366\varepsilon^{0.54} \end{aligned} \tag{6.4}$$

Therefore, the final form of Eq. (6.3) is:

$$\sigma = 5293.8\varepsilon^{0.03} + d^{-\frac{1}{2}} \cdot 365.6\varepsilon^{0.54} - \lambda \cdot \left(1833\varepsilon^{0.03} + d^{-\frac{1}{2}} \cdot 365.6\varepsilon^{0.54}\right) \tag{6.5}$$

6.6 Result analysis

By using Eq. (3.9) in Chapter 3 and Eq. (6.5), the critical value C, which represents the fracture energy of sheet metal, is calculated and listed in Table 6.3. The critical value C shows the same trend as the flow stress – strain curve in Fig. 6.4. The as-received sample has the lowest fracture energy and smallest fracture strain among all the heat treatment scenarios. For the samples with heat treatment, the fracture energy and fracture become small with the increase of grain size.

Table 6.3 The critical value and fracture strain in different heat treatment conditions

Heat treatment condition ($^{\circ}C$)	As-received	500	600	750
Critical value	432.73	896.401	638.543	446.72
Fracture strain	0.095	0.20	0.17	0.14

In Chapters 3, 4 and 5, if the Freudenthal fracture criterion is used, the critical value and the expected fracture strain increase with grain size. This has been proved with the hybrid constitutive model in compression-dominative deformation process. But in tensile test, this conclusion is not applicable for micro-scaled sheet metal forming process.

The main reason for this phenomenon is the material and the heat treatment condition. The testing material C2680R is a type of brass, which consist of 68 percent of copper and 31% of zinc. Dezincification of brass occurs when the brass sample is heated over the recrystallization temperature for over half an hour. The dezincification level increases with heat treatment time. With the zinc vaporizing out of the specimen, a tiny void will be left on the place where the zinc used to be. With the longer heating time and the higher temperature, there are voids in the testing material, as shown in Fig. 6.6.

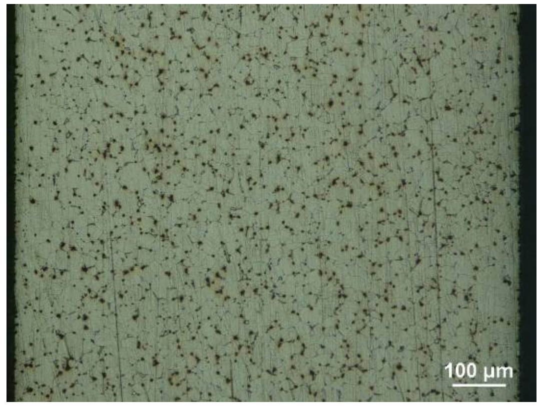

$650^{\circ}C, 2h$

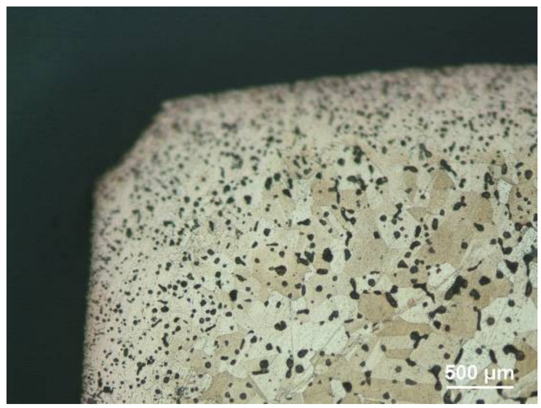

$900^{\circ}C, 3h$

Fig. 6.6. Voids initiated by dezincification of brass in bulk material

For bulk material mentioned in Chapters 3, 4 and 5, the dezincification does not affect stress-strain curve much as the proportion of surface layer grain is around 5% to 60%. Although some of the zinc in the surface layer of the specimen vaporizes after annealed at $750^{\circ}C$ for three hours, the zinc in the internal layer can hardly vaporize. On the other hand, the experiments in Chapter 3, 4 and 5 are all compression-dominative deformation process. Even there are voids occurring in the internal layer of the specimen, they will be eliminated in deformation since the rest material in the rest part of the specimen will fill up their original positions.

However, for sheet material in this chapter, the dezincification of brass has significant influence over fracture energy and fracture strain. As the sheet metal is very thin along thickness direction, zinc is considered to be much easier to vaporize, which will create more voids than bulk material. In addition, both the tensile test and deep drawing experiment is the tensile-dominative deformation, these voids will not only exist during the deformation process, but also have the chance to grow and form micro cracks with the voids nearby. This is illustrated in Figs. 6.7 and Fig. 6.8, which are the experimental and simulation results of the micro-scaled sheet metal forming of the as-received material and those annealed at $750^{\circ}C$.

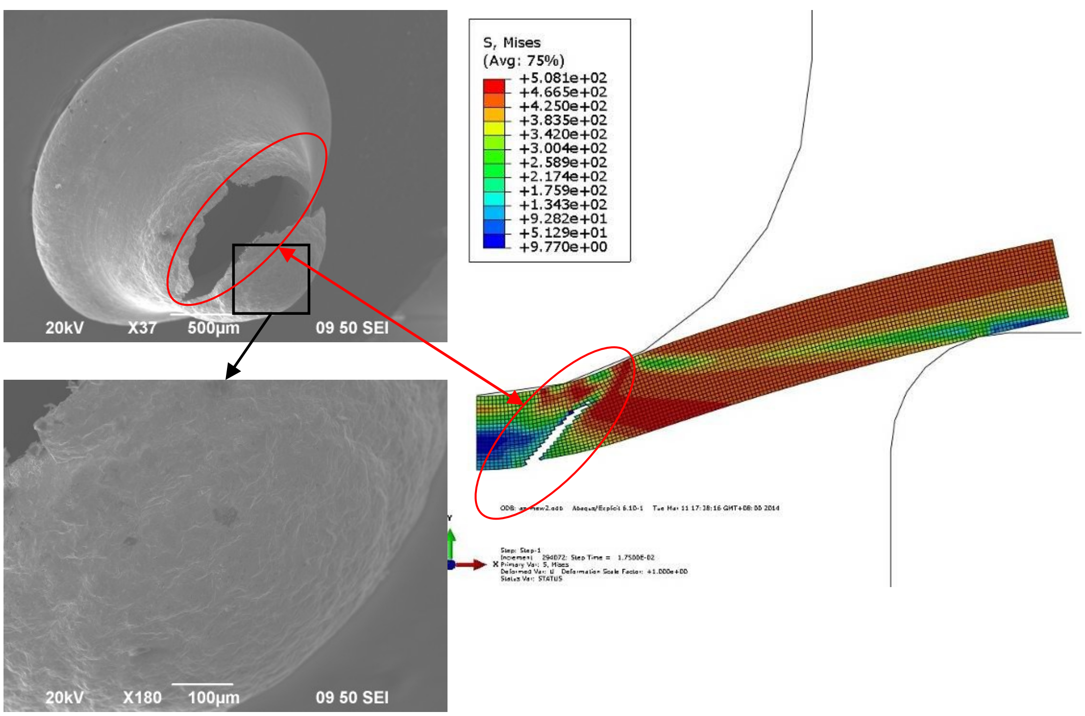

Fig. 6.7. Experimental and simulation results of deep drawing process (Low size factor).

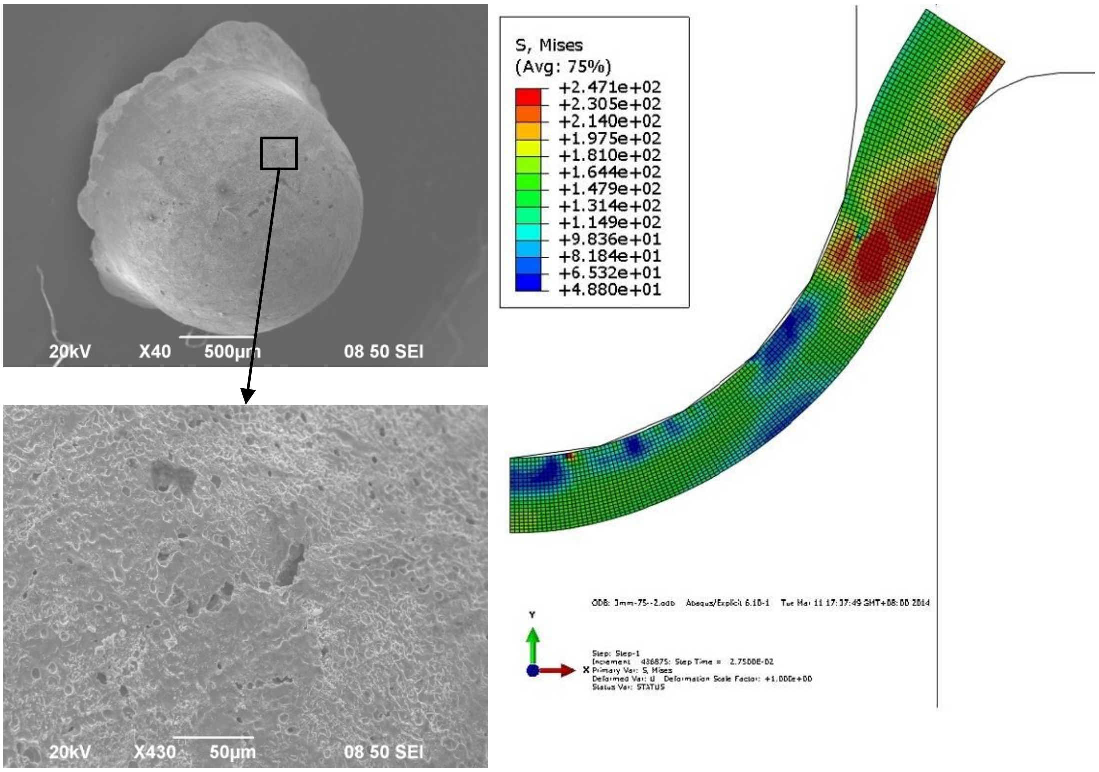

Fig. 6.8. Experimental and simulation results of deep drawing process (High size factor).

In Fig. 6.7, both the experimental and simulation results show that the major crack is induced by flow stress. The top surface of the as-received specimen is smooth without voids caused by the dezincification of brass. As the raw material is well lubricated before deformation, it is certain that the fracture of the as-received sample is not affected by friction stress or irregular metal flow, but only caused by the overwhelming stress during the deformation.

In Fig. 6.8, the SEM photo shows that the formed surface does not have the major crack. When higher magnification time is acquired, tiny voids are found on the top surface of the formed specimen. This is the direct proof of the size effect influence in micro-scaled sheet metal forming: Although the samples annealed at $750^{\circ}C$ has coarser grains and more tiny voids than the as-received sample, it is still able to complete deep drawing deformation without forming major cracks.

6.7 Summary

A fracture model for micro-scaled sheet metal forming is established based on the surface layer model and Freudenthal fracture criterion. Micro-scaled deep drawing process is thus used to verify the fracture model. In this chapter, the following conclusion can be made:

1. Surface layer model is suitable to describe the influence of micro-scaled sheet metal deformation. As there are only several grains along the thickness direction of sheet metal, the influence of size effect is much more obvious in micro-scaled sheet metal forming than micro-scaled bulk metal forming.
2. For the grain size effect in micro-scaled sheet metal forming, the specimen with coarser grain has better mechanical property than the as-received specimen, as there might be only 1~2 grains along the thickness direction.
3. When brass is used as the testing material in sheet metal forming, heat treatment is more likely to cause dezincification and affect the material property of the testing material.

Chapter 7 Conclusions and Suggestions for Future Research

7.1 Conclusions

In this research, the hybrid constitutive fracture model including a hybrid flow stress model is proposed and the evaluation of uncoupled ductile fracture criteria for their applicability in micro-scaled plastic deformation is carried out. Using micro flanged upsetting and micro-scaled deep drawing as the case study process, the FE simulation and the proposed model are verified and validated. The research provides an in-depth understanding of the influence of size effect in microforming and a basis for ductile fracture prediction and avoidance, and forming process design in terms of forming limit and product quality improvement.

First of all, a flow stress model, which can represent the stress contribution of each phase in multiphase alloys, is established. This hybrid flow stress model is proved to be accurate and suitable for fracture prediction of both bulk metal forming and sheet metal forming. Compared with the conventional constitutive model, the influence of size effect is considered. With the expected fracture strain calculated using this model, the SFM is established to distinguish the different influence of flow stress over feature size effect and grain size effect.

Secondly, the conventional fracture criteria for macro-scaled deformation process are evaluated in terms of their applicability in fracture prediction in micro-scaled forming processes. The generalized formation of the six uncoupled fracture criteria is proposed and the deviation of fracture prediction by using these criteria is presented. Meanwhile, Freudenthal fracture criterion is considered as a most suitable fracture criterion for both tensile-dominative and compression-dominative deformations.

By combining the research results of constitutive modeling and fracture criterion evaluation in micro-scaled plastic deformation, the hybrid constitutive fracture model can provide a satisfied fracture prediction for flanged upsetting, backward extrusion and deep drawing process. Using this model, the expected fracture strain of the testing material can be calculated, and SFM for the testing material can be set up. All the expected fracture strains with different microstructures and dimensions can be determined via stress-induced fracture map without conducting tensile or upsetting test for the same material with different microstructures and dimension. The thesis provides a systematical study on micro-scaled plastic deformation, and the in-depth understanding of micro-scaled ductile fracture.

7.2 Suggestions for future research

7.2.1 Fracture criterion evaluation in microforming

As pointed out in Chapter 5, six commonly used ductile fracture criteria are evaluated for their applicability in micro-scaled ductile fracture prediction. The generalized form for these six criteria is proposed to explain the deviation between the strain predicted by these fracture criteria and the experimental results. However, some of the uncoupled fracture criteria such as McClintock criteria cannot be analyzed with this generalized equation. On the other hand, the applicability of uncoupled fracture criteria in micro-scaled plastic deformation is determined for compression-dominative deformation. The fracture criterion evaluation for tensile-dominative deformation process, however, has not been discussed in this research. For coupled criteria, there is the same issue to be explored and addressed.

In tandem of this, further exploration is needed from these two aspects. The final generalized form of ductile fracture criteria need to be revised to cover more uncoupled fracture criteria such as McClintock, Norris and Johnson-Cook fracture criteria. Meanwhile, micro-scaled tensile test of bulk metal will be conducted and the applicability for ductile fracture in tensile-dominative deformation will be evaluated in our future research. Its critical value needs be calculated and compared with the one in compression-dominative deformation.

For coupled fracture criteria such as the Gurson-Tvergaard-Needleman porous plasticity model (GTN model), the influence of size effect will be considered. Compared with the uncoupled ductile fracture criteria, the prediction result of the GTN model with the consideration of size effect should be more accurate in tensile-dominative plastic deformation process.

7.2.2 Ductile fracture in micro-scaled sheet metal forming

In this thesis, the micro-scaled sheet metal forming is presented and considered as another important microforming process, in addition to micro-scaled bulk forming. The ductile fracture in this process is also a very critical issue. In Chapter 6, the constitutive model for micro-scaled deep drawing process is established and the ductile fracture in this process is successfully predicted. In modern industry, the progressive sheet metal forming process, which consists of several forming processes such as deep drawing and blanking, has a much higher manufacturing efficiency than separated deep drawing process [65]. In ductile fracture in this microforming process is of special importance in understanding of the process and deformation behaviors.

In this process, the die set for micro-scaled progressive forming consists of different die and punches in each forming operation. The original material of the progressive forming will be a piece of long sheet metal. The sheet metal will be firstly deep drawn into a cylinder, but still connected with the original sheet metal, which will be used as the perform for further deep drawing. After a few steps of drawing, the cylinder will be getting longer and thinner. Blanking is the last forming operation when the length and diameter of the cylinder reaches the expected value.

In future research, the above-mentioned micro-scaled deep drawing process will be conducted with the progressive forming tooling. The hybrid constitutive modeling of the micro-scaled tensile-dominative deformation will be conducted for fracture prediction. The stress-induced fracture inthe deformation process will thus be analyzed via FE simulation. The fracture based forming capability will be investigated in the process for design of the deformation in each operation and the total deformation in the whole process.

References

[1] Altan, T., G. Ngaile, and G. Shen, Cold and hot forging : fundamentals and applications. 2004, Materials Park, Ohio: ASM International.

[2] Wen J., Huang Y., Hwang K.C., Liu C., Li M., 2005. The modified Gurson model accounting for the void size effect. International Journal of Plasticity 21, 381-395.

[3] Ran J.Q., Fu M.W., Chan W.L., 2013. The influence of size effect on the ductile fracture in micro-scaled plastic deformation, International Journal of Plasticity 41, 65-81.

[4] Ran J.Q., Fu M.W., 2013. A hybrid model for analysis of ductile fracture in micro-scaled plastic deformation of multiphase alloys. International Journal of Plasticity, Accepted Manuscript, Available online.

[5] Pawelski O., 1992. Ways and Limits of the Theory of Similarity in Application to Problems of Physics and Metal Forming. Journal of Materials Processing Technology 34, 19–30.

[6] Picart P, Ghouati O, Gelin J.C., 1998. Optimization of metal forming process parameters with damage minimization. J. Mater. Process Technol.. 80–81, 597–601.

[7] Michel J.F., Picart P., 2002. Modeling the constitutive behavior of thin metal sheet using strain gradient theory. Journal of Materials Processing Technology. 125-126, 164-169.

[8] Chan W.L., Fu M.W., Lu J., 2011. The size effect on micro deformation behavior in micro-scale plastic deformation. Materials & Design 32, 198-206.

[9] Chan W.L., 2011, Experimental and numerical studies on the macro-and micro-scale metal-deformed product design and development, Ph.D dissertation.

[10] Vollertsen F., 2003. Size Effects in Manufacturing. BIAS-Verlag, Bremen 24. p. 1-9.

[11] Vollertsen F., 2008. Categories of size effects. Production Engineering-Research and Development 2, 377-383.

[12] Argon A.S., 2008. Strengthening Mechanisms in Crystal Plasticity. Oxford University Press.

[13] Ashby M.F., 1970, The deformation of plastically non-homogeneous materials. Philosophical Magazine 21, 399-424.

[14] Lai X.M., Peng L.F., Hu P., Lan S.H., Ni J., 2008. Material behavior modelling in micro/meso-scale forming process with considering size/scale effects. Computational Materials Science 43, 1003-1009.

[15] Gouveia B.P.P.A., Rodrigues J.M.C., Martins P.A.F., 1995. Fracture predicting in bulk metal forming. International Journal of Mechanical Sciences. 38, 360-372.

[16] Ogawa N., Shiomi M., Osakada K., 2002. Forming limit of magnesium alloy at elevated temperatures for precision forging. International Journal of Machine Tools & Manufacture. 42, 607–614.

[17] Sljapic V., Hartley P., Pillinger I., 2002. Observations on fracture in axi-symmetric and three-dimensional cold upsetting of brass. Journal of Materials Processing Technology. 125–126, 267–274.

[18] Murty S.V.S.N., Rao B.N., Kashyap B.P., 2004. Improved ductile fracture criterion for cold forming of spheroidised steel. Journal of Materials Technology 147, 94-101.

[19] Li H., Fu M.W., Lu J., Yang H., 2011. Ductile fracture: Experiments and computations. International Journal of Plasticity 27, 147-180.

[20] Li Y.N., Karr Dale G., 2009. Prediction of ductile fracture in tension by bifurcation, localization, and imperfection analyses. International Journal of Plasticity. 25, 1128–1153.

[21] Kadkhodapour J., Butz A., Ziaei-Rad S., Schmauder S., 2011. A micro mechanical study on failure initiation of dual phase steels under tension using single crystal plasticity model. International Journal of Plasticity. 27, 1103–1125.

[22] Bao Y.B., Wierzbicki T., 2004. On fracture locus in the equivalent strain and stress triaxiality space. International Journal of Mechanical Sciences 46, 81-98.

[23] Bai Y.L., Wierzbicki T., 2008. A new model of metal plasticity and fracture with pressure and Lode dependence. International Journal of Plasticity 24, 1071-1096.

[24] Brünig M., Chyra O., Albrecht D., Driemeier L., Alves M., 2008. A ductile damage criterion at various stress triaxialities. International Journal of Plasticity 24, 1731-1755.

[25] Brünig M., Albrecht D., Gerke S., 2011. Numerical Analyses of Stress-triaxiality-dependent Inelastic Deformation Behavior of Aluminum Alloys. International Journal of Damage Mechanics 20, 299-317.

[26] Brunig M., Gerke S., 2011. Simulation of damage evolution in ductile metals undergoing dynamic loading conditions. International Journal of Plasticity 27, 1598-1617.

[27] ABAQUS, 2011. Analysis User's Manual (Version 6.11).

[28] Hillerborg, A., Modeer, M. and Petersson P. E., 1976. Analysis of crack formation and crack growth bymeans of fracture mechanics and finite elements. Magazine of Concrete Research 6, 773-781.

[29] Peng L.F., Lai X.M., Lee H.J., Song J.H., Ni J., 2010. Friction behavior modeling and analysis in micro/meso scale metal forming process. Materials & Design 31, 1953-61.

[30] Armstrong R.W., 1962. The plastic deformation of polycrystalline aggregates. Philosophical Magazine. 7, 45-48.

[31] Armstrong R.W., 1982. The yield and flow stress dependence on polycrystal grain size. Yield, Flow and Fracture Polycrystals. 1-31.

[32] Clausen B., Lorentzen T., and Leffers T., 1988. Self-consistent modeling of the plastic deformation of F.C.C. polycrystals and its implications for diffraction measurements of internal stresses. Acta mater.. 46, 3087-3098.

[33] Keller C., Hug E., Habraken A.M., Duchene L., 2012. Finite element analysis of the free surface effects on the mechanical behavior of thin nickel polycrystals. International Journal of Plasticity. 29, 155–172.

[34] Saanouni K., Mariage J.F., Cherouat A., Lestriez P., 2004. Numerical prediction of discontinuous central bursting in axisymmetric forward extrusion by continuum damage mechanics. Comput. Struct. 82, 2309–2332.

[35] Atkins A.G., Mai Y.W., 1985. Elastic and plastic fracture: metals, polymers, ceramics, composites, biological materials.

[36] Cockroft M.G., Latham D.J., 1968. Ductile and workability of metals. J. Inst. Metall. 96, 33 – 39.

[37] Gospodinov G. and Kerelezova I., 2002. Boundary elements modeling of plain concrete notched beams by means of crack propagation formuala.

[38] Charlie R. Brooks, 1993. Ashok choudhury, Meallurgical: Failure analysis.

[39] Hansen N., 1985, Polycrystalline Strengthening. Metallurgical and Materials Transactions A.

[40] Bouquerel J., Verbeken K., De Cooman B.C., 2006, Microstructure-based model for the static mechanical behavior of multiphase steels. Acta materialia 54, 1443-1456.

[41] Petch N.J., 1953, The Journal of the Iron and Steel Institute 174, 25-28.

[42] Freudenthal, F.A., 1950. The Inelastic Behavior of Solids. Wiley, New York.

[43] Geiger M., Kleiner M., Eckstein R., Tiesler N., Engel U., 2001. Microforming. CIRP Annals -Manufacturing Technology, 50, 445-462.

[44] Fu M.W., Chan W.L., 2012. A review on the state-of-the-art microforming technologies. International Journal of Advanced Manufacturing Technology 67, 2411-2437.

[45] Chan W.L., Fu M.W., 2012. Experimental and simulation based study on micro-scaled sheet metal deformation behavior in microembossing process, Material Science and Engineering A 556, 60-67.

[46] Chan W.L., Fu M.W., 2013. Meso-scaled progressive forming of bulk cylindrical and flanged parts using sheet metal, Material & Design 43, 249-257.

[47] Hamblia R, Reszka M., 2002. Fracture criteria identification using an inverse techniquemethod and blanking experiment. International Journal of Mechanical Sciences, 44, 1349-1361.

[48] Khan A.S., Liu H., 2012. A new approach for ductile fracture prediction on Al 2024-T351 alloy. International Journal of Plasticity 35, 1-12.

[49] Khan A.S., Liu H., 2012. Strain rate and temperature dependent fracture criteria for isotropic and anisotropic metals. International Journal of Plasticity 37, 1-15.

[50] Wierzbicki T., Bao Y., Lee Y.W., Bai Y.L.,2005. Calibration and evaluation of seven fracture models. International Journal of Mechanical Sciences, 47, 719-743.

[51] Xue, L., Wierzbicki T., 2007. Ductile Fracture Modeling-Theory, Experimental Investigation and Numerical Verification. MASSACHUSETTS INSTITUTE OF TECHNOLOGY PHd dissertation.

[52] Oyane, M., 1972. Criteria of DF strain. Bull. JSME 15, 1507–1513.

[53] Ayada, M., Higashino, T., Mori, K., 1984. Central bursting in extrusion of inhomogeneous materials. In: Proceedings of the First ICTP. Adv. Technol. of Plast.,vol. 1, pp. 553–558.

[54] Brozzo, P. Deluca, B., Rendina, R., 1972. A new method for the prediction of formability limits of metal sheets. In: Sheet Metal Forming and Formability. Proceedings of the Seventh Biennial Congress of International Deep Drawing Research Group, Amsterdam, Netherlands.

[55] Rice, J.R., Tracey, D.M., 1969. On the ductile enlargement of voids in triaxial stress fields. J. Mech. Phys. Solids 17, 201 – 217.

[56] McClintock, F.A., 1968. A criterion for DF by the growing of holes. J. Appl. Mech. 90, 363 – 371.

[57] Luo M., Wierzbicki T., 2010. Numerical failure analysis of a stretch-bending test on dual-phase steel sheets using a phenomenological fracture model. International Journal of Solids and Structures 47, 3084-3102.

[58] Luo M., Dunand M., Mohr D., 2012. Experiments and modeling of anisotropic aluminum extrusions under multi-axial loading – Part II: Ductile fracture. International Journal of Plasticity. 32–33, 36–58.

[59] Malcher L., Pires F.M.A., Cesar de Sa J.M.A., 2012. An assessment of isotropic constitutive models for ductile fracture under high and low stress triaxiality. International Journal of Plasticity 30-31, 81-115.

[60] Qin Y., Balendra R., 2003. Optimisation of the lubrication for the extrusion of solid and tubular components by injection forging. Journal of Materials Processing Technology, 135, 219–227.

[61] Qin Y., Balendra R., 2004. An approach for the forming of large-thickness-flange components by injection forging. Journal of Materials Processing Technology, 145, 153–162.

[62] Rodriguez R., Gutierrez I., 2003. Correlation between nanoindentation and tensile properties influence of the indentation size effect, Materials Science and Engineering A, 361, 377–384.

[63] Uthaisangsuk V., Muenstermann S., Prahl U., Bleck W., Schmitz H.P., Pretorius T., 2011. A study of microcrack formation in multiphase steel using representative volume element and damage mechanics. Computational Materials Science, 50, 1225–1232.

[64] Wang J. L., Fu M. W., Ran J. Q., 2013. Analysis and avoidance of flow-induced defects in meso-forming process: simulation and experiment. International journal of advanced manufacturing technology, 68, 1551–1564.

[65] Fu M.W., Chan W.L., 2013. Micro-scaled progressive forming of bulk micropart via directly using sheet metals. Materials & Design, 49, 774-783.